WIP: Work in Progress Title

Ludwig-Maximilians-University Munich
Faculty of Physics

Dissertation

Eric Schanet

February 2021

WIP: Work in Progress Title

Ludwig-Maximilians-Universität München
Fakultät für Physik

Dissertation

Eric Schanet

February 2021

Supervisor: Prof. Dr. Dorothee Schaile

Abstract

My abstract

Zusammenfassung

Meine Zusammenfassung

Contents

Notes

Introduction

Here is my introduction

Natural units and Minkowski metric

Part I

Fundamental concepts

Chapter 1

Theory

This chapter starts with an outline of the basic principles and concepts of the Standard Model of Particle Physics (SM), the theoretical framework describing nature on the level of elementary particles. This is followed by an introduction to supersymmetry, a promising class of theories aiming to solve some of the shortcomings of the SM.

By no means intended to be a full description, this chapter merely tries to highlight the important relations and consequences of the SM and supersymmetry. The mathematical description of this chapter largely follows [1, 2] for the SM and [3] for supersymmetry.

1.1 The Standard Model of Particle Physics

By the end of the 1920s, quantum mechanics and general relativity had been relatively well established and the consensus among physicists was that matter was made of nuclear atoms consisting of electrons and protons. During the 1930s, a multitude of new experimental discoveries and theoretical puzzles excited physicists in three main fields of research: nuclear physics, cosmic rays and relativistic quantum mechanics. The following years and decades saw particle physics emerge as a result of these currents ultimately flowing together.

Since these early times of particle physics research, physicists have made extraordinary progress in describing nature at the subatomic scale. Today, a century later, the resulting theoretical framework, the Standard Model of Particle Physics, is the most fundamental theory of nature to date. It provides an extremely precise description of the interactions of elementary particles and—using the Large Electron Positron collider (LEP)—has been tested and verified to an unprecedented level of accuracy up to the electroweak (EWK) scale. Given the unprecedented success of SM, it is not surprising that its history is paved with numerous awards for both experimental and theoretical work. In 1964, the Nobel prize was awarded to Feynman, Schwinger and Tomonoga for their fundamental work in quantum electrodynamics (QED). This quantum field theory allows to precisely calculate fundamental processes as e.g. the anomalous magnetic moment of the electron to a relative experimental uncertainty of 2.3×10^{-10} [4]. In 1979, Glashow, Weinberg and Salam were awarded with the Nobel prize for their work towards electroweak unification. The most prominent recent progress is undoubtedly the discovery of the Higgs boson, not only resulting in the Nobel prize being awarded to Englert and Higgs,

Table 1.1: Names, electric charges and masses (rounded to three significant digits if known to that precision) of all observed fermions in the SM [5].

	generation	particle	electric charge [e]	mass
leptons	1	electron (e)	-1	511 keV
		electron neutrino (ν_e)	0	$<$ 2 eV
	2	muon (μ)	-1	106 MeV
		muon neutrino (ν_μ)	0	$<$ 0.19 MeV
	3	tau (τ)	-1	1.78 GeV
		tau neutrino (ν_τ)	0	$<$ 18.2 MeV
quarks	1	up (u)	$\frac{2}{3}$	2.3 MeV
		down (d)	$-\frac{1}{3}$	4.8 MeV
	2	charm (c)	$\frac{2}{3}$	1.28 GeV
		strange (s)	$-\frac{1}{3}$	95 MeV
	3	top (t)	$\frac{2}{3}$	173 GeV
		bottom (b)	$-\frac{1}{3}$	4.18 GeV

but also completing the SM, roughly 50 years after the existence of the Higgs boson had been theorised.

Couplings and masses are measured from experiment

1.1.1 Particle content of the SM

Neutrino masses not in SM!

The SM successfully describes ordinary matter as well as their interactions, namely the electromagnetic, weak and strong interactions. Gravity is the only fundamental force not described within the SM. The particles in the SM are classified into two main categories, depending on their spin. Particles with half-integer spin follow Fermi-Dirac statistics and are called fermions. As they are subject to the Pauli exclusion principle, they make up ordinary matter. Particles with integer spin follow Bose-Einstein statistics and mediate the fundamental interactions between fermions.

need ref

Fermions are further divided into leptons and quarks, which each come in three generations with increasing masses[†]. The three electrically charged leptons are each associated with a corresponding neutral neutrino (more on this *association* in chapter). While the SM assumes massless neutrinos, the observation of neutrino oscillations [6] implies the existence of at least two massive neutrinos. By extending the SM to allow non-vanishing neutrino masses, neutrino oscillations can be introduced through lepton generation mixing, described by the Pontecorvo-Maki-Nakagawa-Sakata (PMNS) matrix [7]. Apart from an electric charge, the six quarks also carry a colour charge. There are three types of colour charge: *red*, *green* and *blue* as well as their respective anti-colours. The mixing in the quark sector through the weak interaction can be described by the Cabibbo-Kobayashi-Maskawa (CKM) matrix [8, 9]. Finally, each fermion comes with its own anti-particle with same mass and spin, but inverted charge-like quantum numbers[§]. All fermions in the SM are listed in table 1.1.

† Neutrinos might not exist in a normal mass hierarchy but could also have an inverted mass hierarchy.

§ The exact nature of anti-neutrinos is still an open question and ties into whether or not the neutrino mass matrix contains non-vanishing Majorana mass terms.

Table 1.2: Names, electric charges and masses (rounded to three significant digits if known to that precision) of all observed bosons in the SM [5].

particle	spin	electric charge $[e]$	mass
photon (γ)	1	0	0
gluon (g)	1	0	0
$W^{\pm}$	1	± 1	80.4 GeV
Z^0	1	0	91.2 GeV
Higgs boson (H)	0	0	125 GeV

The fundamental forces described by the SM are propagated by bosons with spin $1\hbar$. The photon γ couples to electrically charged particles and mediates the electromagnetic interaction. As the photon is massless, the electromagnetic force has infinite range. The strong force is mediated by gluons carrying one unit of colour and one unit of anti-colour. Due to colour-confinement, colour charged particles like quarks and gluons cannot exist as free particles and instead will always form colour-neutral bound states. Although nine gluon states would theoretically be possible, only eight of them are realised in nature: the colour-singlet state $\frac{1}{\sqrt{3}}(|r\bar{r}\rangle + |g\bar{g}\rangle + |b\bar{b}\rangle)$ would be colour-neutral result in long-range strong interactions, which have not been observed. Finally, the weak force is mediated by a total of three bosons, two charged W-bosons W^+ and W^-, and a neutral Z-boson. The mediators of the weak force are massive, resulting in a finitely ranged interaction. The $W^{\pm}$ and Z bosons gain their masses through the Higgs mechanism (discussed in chapter), resulting in a massive spin-0 boson, called the Higgs boson. All bosons known to the SM are listed in table 1.2.

Might want to explain this later once I introduced the gauge groups?

need ref

1.1.2 The SM as a gauge theory

Formally, the SM is a collection of a special type of quantum field theories, called gauge theories. Quantum field theory (QFT) is the application of quantum mechanics to dynamical systems of fields, just as quantum mechanics is the quantisation of dynamical systems of particles. QFT provides a uniform description of quantum mechanical particles and classical fields, while including special relativity.

In classical mechanics, the fundamental quantity is the action S, which is the time integral of the Lagrangian L, a functional characterising the state of a system of particles in terms of generalised coordinates $q_1, \ldots, q_n$. In field theory, the Lagrangian can be written as spatial integral of a Lagrangian density $\mathcal{L}(\phi_i, \partial_\mu \phi_i)$, that is a function of one or more fields ϕ_i and their spacetime derivates $\partial_\mu \phi_i$. For the action, this yields

$$S = \int L \,\mathrm{d}t = \int \mathcal{L}\left(\phi_i, \partial_\mu \phi_i\right) \mathrm{d}^4 x. \tag{1.1}$$

In the following, the Lagrangian density $\mathcal{L}$ will simply be referred to as the *Lagrangian*.

Using the principle of least action $\delta S = 0$, the equation of motions for each field are given by the Euler-Lagrange-equation,

$$\partial_\mu \left(\frac{\partial \mathcal{L}}{\partial \left(\partial_\mu \phi_i \right)} \right) - \frac{\partial \mathcal{L}}{\partial \phi_i} = 0. \tag{1.2}$$

As opposed to the Hamiltonian formalism, the Lagrange formulation of field theory is especially well suited in this context, as it exhibits explicit Lorentz-invariance. This is a direct consequence of the principle of least action, since boosted extrema in the action will still be extrema for Lorentz-invariant Lagrangians.

Explicitly derive the Euler-Lagrange equations? Cf. Peskins Ch.2.2.

Symmetries are of central importance in the SM. As Emmy Noether has famously shown in 1918 [10] for classical mechanics, every continuous symmetry of the action has a corresponding conservation law. In the context of classical field theory, each generator of a continuous internal or spacetime symmetry transformation leads to a conserved current, and thus to a conserved charge. In QFTs, quantum versions of Noether's theorem, called Ward–Takahashi identities [11, 12] for Abelian theories and Slavnov–Taylor identities [13–15] for non-Abelian theories relate the conservation of quantum currents and charge-like quantum numbers to continuous global symmetries of the Lagrangian.

Check correctness of formulation

From a theoretical point of view, the SM can be described by a non-Abelian Yang-Mills type gauge theory based on the symmetry group

cite YM

$$SU(3)_C \otimes SU(2)_L \otimes U(1)_Y,$$

where $U(n)$ ($SU(n)$) describes (special) unitary groups, i.e. the Lie groups of $n \times n$ unitary matrices (with determinant 1, if special). $SU(3)_C$ generates quantum chromodynamics (QCD), i.e. the interaction of particles with colour charge through exchange of gluons, and $SU(2)_L \otimes U(1)_Y$ generates the electroweak interaction. Here, the subscript Y represents the weak hypercharge, while the L indicates that $SU(2)_L$ only couples to left-handed particles (right-handed antiparticles).

Feyman diagrams

Transitioning from classic field theory to quantum field theory is typically done either through canonical quantisation or through the usage of path integral formalism. Only the the simplest field theories can be solved analytically, namely those containing only free fields, without any interactions. Perturbation theory has to be used for calculating scattering cross sections and decay rates for any QFT containing interactions. Any transition matrix can then be written as a series expansion in the coupling constant, with each term represented by a Feynman diagram.

Using appropriate Feynman rules dictating the possible vertices (representing interactions between fields) and propagators (representing the propagation of fields), an infinite number of Feynman diagrams can be written down. Given the incoming and outgoing particles, all possible combinations of propagators and vertices that can be placed in between (i.e. all possible Feynman diagrams) represent the full perturbation series. Only the lowest order in the series is considered at leading order (LO), the next-lowest at next-to-leading order (NLO), and so on.

is this paragraph correct?

Gauge principle

The gauge principle is fundamental to the SM and dictates that the existence of gauge fields is directly related to symmetries under local gauge transformations. QED, being the simplest gauge theory, can be taken to illustrate this important principle. The free Dirac Lagrangian for a single, non-interacting fermion with mass m is given by

$$\mathcal{L}_{\text{Dirac}} = \bar{\psi}\left(i\gamma^{\mu}\partial_{\mu} - m\right)\psi, \tag{1.3}$$

where ψ is a four-component complex spinor field, $\bar{\psi} = \psi^{\dagger}\gamma^{0}$, and γ^{μ} with $\mu = 0, 1, 2, 3$ are the Dirac matrices with the usual anticommutation relations generating a matrix representation of the Dirac algebra

$$\{\gamma^{\mu}, \gamma^{\nu}\} \equiv \gamma^{\mu}\gamma^{\nu} + \gamma^{\nu}\gamma^{\mu} = 2\eta^{\mu\nu}\mathbb{1}_4. \tag{1.4}$$

It is worth noting that the free Dirac Lagrangian is invariant under a global $U(1)$ transformation

$$\psi \to e^{i\theta}\psi, \tag{1.5}$$

where the phase θ is spacetime independent and real. In order to produce the physics of electromagnetism, the free Dirac Lagrangian however has to be invariant under *local* $U(1)$ phase transformations, which is not the case, as the transformed Lagrangian picks up an additional term from the spacetime derivative of the phase $\partial_{\mu}\theta(x)$.

In order for the Dirac Lagrangian to become invariant under a local gauge transformation, a new vector field $A_{\mu}(x)$ has to be introduced and the partial derivative has to be replaced with the covariant derivative†

$$\partial_{\mu} \to D_{\mu} \equiv \partial_{\mu} + ieA_{\mu}, \tag{1.6}$$

where e is the coupling of the fermion field to the gauge field A_{μ} and can be identified with the elementary charge. This leads to a Lagrangian that is invariant under the transformations

$$\psi \to e^{i\theta(x)}\psi, \qquad A_{\mu} \to A_{\mu} - \frac{1}{e}\partial_{\mu}\theta(x). \tag{1.7}$$

The modified Lagrangian now includes a term for interactions between the gauge field and the fermion field

$$\begin{aligned} \mathcal{L} &= \mathcal{L}_{\text{Dirac}} + \mathcal{L}_{\text{int}} \\ &= \bar{\psi}\left(i\gamma^{\mu}\partial_{\mu} - m\right)\psi - \left(e\bar{\psi}\gamma^{\mu}\psi\right)A_{\mu}, \end{aligned} \tag{1.8}$$

and is indeed invariant under a local phase transformation. Yet, it still cannot be complete as it is missing a term describing the kinematics of the free gauge field A_{μ}. For a vector field, the kinetic term is described by the Proca Lagrangian

$$\mathcal{L}_{\text{Proca}} = -\frac{1}{4}F_{\mu\nu}F^{\mu\nu} + \frac{1}{2}m_A^2 A^{\nu}A_{\nu}, \tag{1.9}$$

where $F^{\mu\nu} \equiv (\partial^{\mu}A^{\nu} - \partial^{\nu}A^{\mu})$ is the field strength tensor that is invariant under the transformation in eq. (1.7). Since $A^{\nu}A_{\nu}$ is not invariant under the same transformation, the only way to

† The prescription of achieving local gauge invariance by replacing ∂_{μ} with D_{μ} is called *minimal coupling*.

keep the full Lagrangian invariant under a local phase transformation is by requiring $m_A = 0$, i.e. the introduced gauge field A_μ has to be massless, giving the Maxwell Lagrangian (ultimately generating the Maxwell equations)

$$\mathcal{L}_{\text{Maxwell}} = -\frac{1}{4} F_{\mu\nu} F^{\mu\nu}. \tag{1.10}$$

This finally yields the full Lagrangian

$$\begin{aligned}\mathcal{L}_{\text{QED}} &= \mathcal{L}_{\text{Dirac}} + \mathcal{L}_{\text{Maxwell}} + \mathcal{L}_{\text{int}} \\ &= \bar{\psi}\left(i\gamma^\mu \partial_\mu\right)\psi - m\bar{\psi}\psi - \frac{1}{4} F^{\mu\nu} F_{\mu\nu} - \left(e\bar{\psi}\gamma^\mu \psi\right) A_\mu\end{aligned} \tag{1.11}$$

which can be identified to be the full Lagrangian of QED. The introduced gauge field A_μ is therefore nothing else but the electromagnetic potential with its associated massless particle, the photon. Thus, by applying the gauge principle on the free Dirac Lagrangian, i.e. forcing a global phase invariance to hold locally, a new massless gauge field including interaction terms with the existing fields in the Lagrangian has to be introduced. In the case of the free Dirac Lagrangian, local gauge invariance produces all of quantum electrodynamics.

As Yang and Mills have shown in 1954 [16], requiring a global phase invariance to hold locally is perfectly possible in the case of any continuous symmetry group. Considering a general non-Abelian symmetry group G, represented by a set of $n \times n$ unitary matrices $U(\alpha^1, \dots, \alpha^N)$, parametrised by N real parameters $\alpha^1, \dots, \alpha^N$, then a gauge-invariant Lagrangian can be constructed with a similar prescription [1] as previously in the case of $U(1)$.

A total of n fermion fields with mass m are needed, arranged in an n-dimensional multiplet $\Psi = (\psi_1, \dots, \psi_n)^T$. The free Lagrangian

$$\mathcal{L}_{\text{free}} = \bar{\Psi}\left(i\gamma^\mu \partial_\mu - m\right)\Psi, \tag{1.12}$$

is invariant under a global phase transformation

$$\Psi(x) \to U(\alpha^1, \dots, \alpha^N)\Psi(x), \tag{1.13}$$

Each element in the set of transformations U can be written in terms of the group generators T^a

$$U(\alpha^1, \dots, \alpha^N) = e^{i\alpha^a T^a}, \tag{1.14}$$

where the group indices $a = 1, \dots, N$ are to be summed over. The group generators T^a satisfy the commutation relations

$$[T^a, T^b] = if^{abc} T^c, \tag{1.15}$$

with f^{abc} the so-called structure constants quantifying the lack of commutativity between the generators. By convention, the basis for the generators T^a is typically chosen such that f^{abc} is completely anti-symmetric.

In order to make the Lagrangian invariant under local phase transformations, i.e. under transformations with a set of spacetime-dependent real parameters $\alpha^a(x)$ a vector field $\boldsymbol{W}_\mu$

together with a coupling constant g have to be introduced through the covariant derivative

$$\partial_\mu \to D_\mu = \partial_\mu - ig\boldsymbol{W}_\mu. \tag{1.16}$$

As D_μ acts on the n-dimensional multiplet Ψ, the introduced gauge field $\boldsymbol{W}_\mu$ has to be an $n \times n$ matrix and can thus be expanded in terms of the generators

$$\boldsymbol{W}_\mu(x) = T^a W_\mu^a(x), \tag{1.17}$$

explicitly illustrating, that a total of N gauge fields W_μ^a are introduced through the covariant derivative. Similar to QED above, the covariant derivative also introduces an interaction term of the form

$$\mathcal{L}_{\text{int}} = g\bar{\Psi}\gamma^\mu \boldsymbol{W}_\mu \Psi, \tag{1.18}$$

in the Lagrangian in eq. (1.12), coupling the gauge fields W_μ^a to the fermion fields. For infinitesimal $\alpha^a(x)$, the gauge fields gauge transform according to

$$W_\mu^a \to W_\mu^a + \frac{1}{g}\partial_\mu \alpha^a + f^{abc} W_\mu^b \alpha^c, \tag{1.19}$$

where the term with α^a looks familiar from the $U(1)$ example and corresponds to the Abelian case, while the term with f^{abc} introduces the non-Abelian structure into the theory. The non-Abelian structure is again clearly visible when introducing a kinetic term for the gauge fields into the Lagrangian

$$\mathcal{L}_{\text{W}} = -\frac{1}{4} F_{\mu\nu}^a F^{\mu\nu,a}, \tag{1.20}$$

with the field-strength tensor now $F_{\mu\nu}^a = \partial_\mu W_\nu^a - \partial_\nu W_\mu^a + g f^{abc} W_\mu^b W_\nu^c$. As was already the case for QED, the above Lagrangian contains Abelian terms quadratic in W, describing the propagation of the free gauge fields. This time, the Lagrangian however also contains non-Abelian terms cubic and quartic in W, leading to self-interaction of the gauge fields.

Quantum chromodynamics

Quantum chromodynamics (QCD), the gauge theory describing the strong interaction between quarks and gluons in the SM, is an example for a non-Abelian Yang-Mills theory. QCD is based on the gauge group $SU(3)_C$, with the subscript C indicating that the quantum number associated with the symmetry group is the *colour*. Each quark is described by a triplet of fermion fields $q = (q_r, q_g, q_b)^T$, where the subscripts refer to the three different colours. The symmetry group $SU(3)$ has a total of $n^2 - 1 = 8$ generators, usually expressed in terms of the Gell-Mann matrices λ^a. The covariant derivative introducing the gauge fields G_μ^a acting on the quark triplets is then

$$D_\mu = \partial_\mu - ig_s \frac{\lambda^a}{2} G_\mu^a, \tag{1.21}$$

with g_s the coupling constant of the strong interaction, that is typically written as $\alpha_s = g_s^2/(4\pi)$ in analogy to the fine-structure constant in QED. Gauge invariance thus introduces a total of $N = 8$ gauge fields that can be identified with the eight gluons, leading to the full Lagrangian

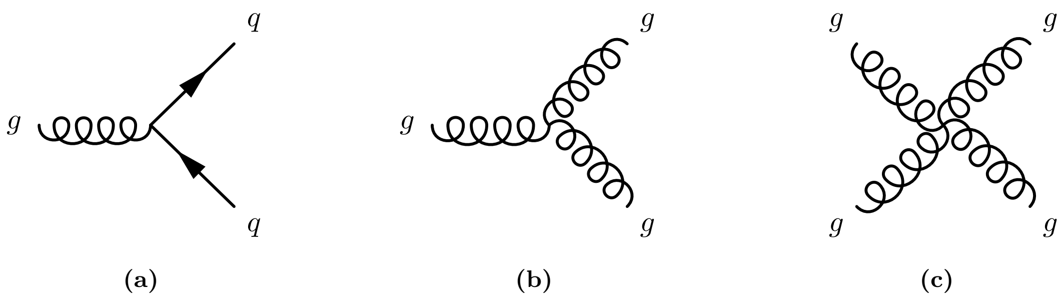

Figure 1.1: Possible vertices in QCD.

of QCD

$$\mathcal{L}_{\mathrm{QCD}} = \sum_q \bar{q}(i\gamma^\mu \partial_\mu - m_q)q - \sum_q -g_s \bar{q}\gamma^\mu \frac{\lambda^a}{2} q G^a_\mu - \frac{1}{4} G^a_{\mu\nu} G^{\mu\nu,a}, \tag{1.22}$$

where $q = u, d, s, c, b, t$ and $G^a_{\mu\nu}$ are the gluon field strengths given by

$$G^a_{\mu\nu} = \partial_\mu G^a_\nu - \partial_\nu G^a_\mu + g_s f^{abc} G^b_\mu G^c_\nu. \tag{1.23}$$

As expected from the previous section, $\mathcal{L}_{\mathrm{QCD}}$ contains terms that are cubic and quartic in the gluon fields, resulting in gluon self-interaction in the theory. All possible QCD interaction vertices involving gluons and quarks are shown in fig. 1.1.The gluon self-interactions lead to a number of phenomena unknown to Abelian theories, rendering the kinematics of QCD highly non-trivial.

In QCD, a similar effect to the electric charge screening in QED happens through quark-antiquark pairs, resulting in a screening of the colour charge. However, the existence of gluon loops in the gluon propagator due to gluon self-interaction creates an opposing *antiscreening* effect of colour charges. At short distances or large momentum scales, colour-charged particles essentially become free particles, a phenomenon that is called *asymptotic freedom*. In this regime, where α_s is sufficiently small, QCD processes can be calculated using perturbation theory. At large distances or small moment scales however, α_s becomes large and gluons interact very strongly with colour-charged particles, meaning that no free gluons or quarks can exist. This phenomenon is called *confinement* and implies that free quarks and gluons will be subject to *hadronisation*, i.e. form colourless bound states by combining with other quarks or gluons (that can be created from the vacuum). In a particle detector, hadronisation manifests itself as collimated showers of particles, called *jets*.

At momentum scales where the strong coupling α_s becomes large ($\alpha_s \approx \mathcal{O}(1)$), QCD processes can no longer be calculated using perturbation theory and instead lattice QCD [17, 18] is used.

Electroweak interaction

During the 1960s, Glashow, Weinberg and Salam [19–21] developed a unified theory of the electromagnetic and weak interactions, based on the $SU(2)_{\mathrm{L}} \otimes U(1)_Y$ symmetry group. Known already experimentally from the Wu experiment'[22] in 1956, weak interaction violates parity, i.e. the symmetry transformations have to act differently on the left-handed and right-handed fermion fields. The left- and right-handed components of a fermion field can be projected out using

$$\psi_{\mathrm{L}} = \frac{1-\gamma^5}{2}\psi, \qquad \psi_{\mathrm{R}} = \frac{1+\gamma^5}{2}\psi, \tag{1.24}$$

with $\gamma^5 = i\gamma^0\gamma^1\gamma^2\gamma^3$. As the weak interaction only acts on left-handed fermions, they can be ordered as $SU(2)$ doublets

$$\begin{pmatrix}\nu_e \\ e\end{pmatrix}_{\mathrm{L}}, \quad \begin{pmatrix}u \\ d\end{pmatrix}_{\mathrm{L}}, \qquad \begin{pmatrix}\nu_\mu \\ \mu\end{pmatrix}_{\mathrm{L}}, \quad \begin{pmatrix}c \\ s\end{pmatrix}_{\mathrm{L}}, \qquad \begin{pmatrix}\nu_\tau \\ \tau\end{pmatrix}_{\mathrm{L}}, \quad \begin{pmatrix}t \\ b\end{pmatrix}_{\mathrm{L}}. \tag{1.25}$$

The quantum number associated with $SU(2)$ symmetry transformations is called weak isospin I with third component I_3. Fermion doublets have $I = 1/2$, with the upper component having $I_3 = 1/2$ and the lower component $I_3 = -1/2$. Right-handed fermion fields have $I = 0$, i.e. are singlet states in weak isospin space

$$e_{\mathrm{R}}, u_{\mathrm{R}}, d_{\mathrm{R}}, \qquad \mu_{\mathrm{R}}, c_{\mathrm{R}}, s_{\mathrm{R}}, \qquad \tau_{\mathrm{R}}, t_{\mathrm{R}}, b_{\mathrm{R}}, \tag{1.26}$$

and thus do not couple to the weak interaction. In the electroweak theory, neutrinos are assumed to be strictly massless, therefore no right-handed neutrino singlets exist.

The fermion doublets can be written in a free Lagrangian similar to eqs. (1.3) and (1.12)

$$\mathcal{L} = \bar{\psi}_{\mathrm{L}} i\gamma^\mu \partial_\mu \psi_{\mathrm{L}}, \tag{1.27}$$

with one crucial difference—the omission of the fermion masses. As $\bar{\psi}\psi = \bar{\psi}_{\mathrm{L}}\psi_{\mathrm{R}} + \bar{\psi}_{\mathrm{R}}\psi_{\mathrm{L}}$, mass terms would mix left- and right-handed terms and break gauge invariance. Section 1.1.2 will illustrate how fermion masses will instead be generated in the electroweak theory. For left-handed fermion fields, local $SU(2)_{\mathrm{L}}$ transformations can be written as

$$\psi_{\mathrm{L}} \to \exp\left(ig_2\alpha^a\frac{\sigma^a}{2}\right)\psi_{\mathrm{L}}, \tag{1.28}$$

where g_2 is the coupling constant, α^a with $a = 1, 2, 3$ are real parameters and the Pauli matrices σ^a are the generators of $SU(2)_{\mathrm{L}}$. By introducing the covariant derivative $D_\mu = \partial_\mu + ig_2\frac{\sigma^a}{2}W_\mu^a$ and including the usual kinetic term for the gauge fields, the Lagrangian becomes invariant under $SU(2)_{\mathrm{L}}$ transformations and reads

$$\mathcal{L} = \bar{\psi}_{\mathrm{L}} i\gamma^\mu D_\mu \psi_{\mathrm{L}} - \frac{1}{4}W_{\mu\nu}^a W^{\mu\nu,a}, \tag{1.29}$$

with the gauge field strength tensors $W_{\mu\nu}^a = \partial_\mu W_\nu^a - \partial_\nu W_\mu^a + g_2\epsilon^{abc}W_\mu^b W_\nu^c$ where ϵ^{abc} are the structure constants. As previously in the case of QCD, the non-Abelian structure of the symmetry group causes self-interactions of the gauge fields.

In order to include electromagnetic interactions, the weak isospin group is extended with the $U(1)_Y$, corresponding to the multiplication of a phase factor $e^{i\alpha\frac{Y}{2}}$ to each of the preceding doublets and singlets. Here, Y is the weak hypercharge as given by the Gell-Mann–Nishijima relation [23–25]

$$Q = I_3 + \frac{Y}{2}, \tag{1.30}$$

with Q the electric charge. The electromagnetic group $U(1)_{\mathrm{em}}$ as a subgroup of the combined electroweak gauge group.

By modifying the covariant derivative to include a $U(1)_Y$ gauge field and ensuring that $U(1)_Y$ acts the same on left- and on right-handed fermions it becomes $D_\mu = \partial_\mu + ig_2 \frac{\sigma^a}{2} W_\mu^a + ig_1 \frac{Y}{2} B_\mu$ for left-handed fermions and $D_\mu = \partial_\mu + ig_1 \frac{Y}{2} B_\mu$ for right-handed fermions. Then the full electroweak Lagrangian reads

$$\begin{aligned}\mathcal{L}_{\text{electroweak}} =& \sum_j^6 \bar{\psi}_{\mathrm{L}}^j i\gamma^\mu \left(\partial_\mu - ig_2 \frac{\sigma^a}{2} W_\mu^a + ig_1 \frac{Y}{2} B_\mu\right) \psi_{\mathrm{L}}^j \\ &+ \sum_j^9 \bar{\psi}_{\mathrm{R}}^j i\gamma^\mu \left(\partial_\mu + ig_1 \frac{Y}{2} B_\mu\right) \psi_{\mathrm{R}}^j\end{aligned} \tag{1.31}$$

where $B_{\mu\nu} = \partial_\mu B_\nu - \partial_\nu B_\mu$.

Spontaneous symmetry breaking

In the electroweak theory a total of three vector fields W_μ^a and one vector field B_μ are associated with the gauge groups $SU(2)_{\mathrm{L}}$ and $U(1)_Y$, respectively. As has been shown explicitly through the example of QED in section 1.1.2, the gauge fields need to be massless for the resulting Lagrangian to be gauge invariant under the respective symmetry group. In addition, the electroweak symmetry group does not allow for fermion masses. Both gauge bosons of the weak interaction and the fermion are however manifestly massive, hence the electroweak symmetry has to be broken in the SM.

This spontaneous symmetry breaking is achieved through the Brout-Englert-Higgs mechanism [26–28]. In the SM, an isospin doublet of complex scalar fields, called Higgs doublet, is introduced

$$\Phi(x) = \begin{pmatrix} \phi^+(x) \\ \phi^0(x) \end{pmatrix}. \tag{1.32}$$

The Higgs doublet has hypercharge $Y = 1$, hence according to eq. (1.30), ϕ^+ has electric charge $+1$ while ϕ^0 is electrically neutral. With the covariant derivative introduced in section 1.1.2, the Higgs doublet gets an associated part in the SM Lagrangian reading

$$\mathcal{L}_{\mathrm{H}} = (D_\mu \Phi)^\dagger (D^\mu \Phi) - V(\Phi), \tag{1.33}$$

where $V(\Phi)$ is a gauge invariant potential

$$V(\Phi) = -\mu^2 \Phi^\dagger \Phi + \frac{\lambda}{4} (\Phi^\dagger \Phi)^2. \tag{1.34}$$

For positive and real parameters μ^2 and λ, this potential has the form of a *Mexican hat* and an infinite number of minima for field configurations with $\Phi^\dagger \Phi = 2\mu^2/\lambda$. In the vacuum, i.e. in the ground state of the theory with minimal potential energy of the field, one of these minima is chosen such that the Higgs receives a vacuum expectation value (VEV)

$$\langle\Phi\rangle = \frac{1}{\sqrt{2}}\begin{pmatrix}0\\ v\end{pmatrix} \qquad \text{with} \quad v = \frac{2\mu}{\sqrt{\lambda}} \approx 246\,\text{GeV}. \tag{1.35}$$

This is neither invariant under a $SU(2)_\mathrm{L}$ transformation of the form $U = \exp(i\alpha^a \frac{\sigma^a}{2})$, nor under a $U(1)_Y$ transformation of the form $\exp(i\alpha\frac{Y}{2})$, therefore the electroweak gauge symmetry is spontaneously broken; the Lagrangian has a symmetry that the vacuum does not have. It is worth noting that the $U(1)_\mathrm{em}$ gauge symmetry is not broken as the VEV of ϕ^+ vanishes and ϕ^0 is invariant under $U(1)_\mathrm{em}$.

The Higgs doublet can be expressed as excitations around the ground state

$$\Phi(x) = \frac{1}{\sqrt{2}}\begin{pmatrix}\phi_1(x) + i\phi_2(x)\\ v + H(x) + i\chi(x)\end{pmatrix}, \tag{1.36}$$

where H, χ, ϕ_1 and ϕ_2 are real scalar fields with vanishing VEV. The Higgs potential can then be written as

$$V = \mu^2 H^2 + \frac{\mu^2}{v}H(H^2 + \chi^2 + \phi_1^2 + \phi_2^2) + \frac{\mu^2}{4v^2}(H^2 + \chi^2 + \phi_1^2 + \phi_2^2), \tag{1.37}$$

where only H gets a mass term, thus describing an electrically neutral scalar particle with mass $m_H = \sqrt{2}\mu$. The remaining scalar fields remain massless, in accordance with the Nambu-Goldstone theorem [29, 30], stating that every spontaneously broken continuous symmetry generates a massless Goldstone boson. These bosons are unphysical and can be gauged away through a $SU(2)_\mathrm{L}$ transformation, such that the expansion around the vacuum from eq. (1.36) involves only the physical scalar $H(x)$

$$\Phi(x) = \frac{1}{\sqrt{2}}\begin{pmatrix}0\\ v + H(x)\end{pmatrix}. \tag{1.38}$$

The gauge transformation bringing eq. (1.36) into the above form is called the *unitary gauge*. In this gauge, the Higgs potential from eq. (1.34) has the form

$$V = \frac{m_H^2}{2}H^2 + \frac{m_H^2}{2v}H^3 + \frac{m_H^2}{8v^2}H^4, \tag{1.39}$$

containing cubic and quartic self-interactions of the Higgs field proportional to m_H^2. Inserting the excitation around the vacuum state in the kinetic term of the $\mathcal{L}_\mathrm{H}$ yields mass terms for the vector bosons

$$\mathcal{L}_\mathrm{H} \propto \frac{v^2}{8}g_2^2\left(W_\mu^1 W^{1,\mu} + W_\mu^2 W^{2,\mu}\right) + \frac{v^2}{8}\begin{pmatrix}W_\mu^3 & B_\mu\end{pmatrix}\begin{pmatrix}g_2^2 & g_1 g_2\\ g_1 g_2 & g_1^2\end{pmatrix}\begin{pmatrix}W^{3,\mu}\\ B^\mu\end{pmatrix}, \tag{1.40}$$

Instead of expressing the Lagrangian in terms of the fields W_μ^a and B_μ that make the original gauge invariance manifest, it can also be written in terms of the *physical* fields that correspond

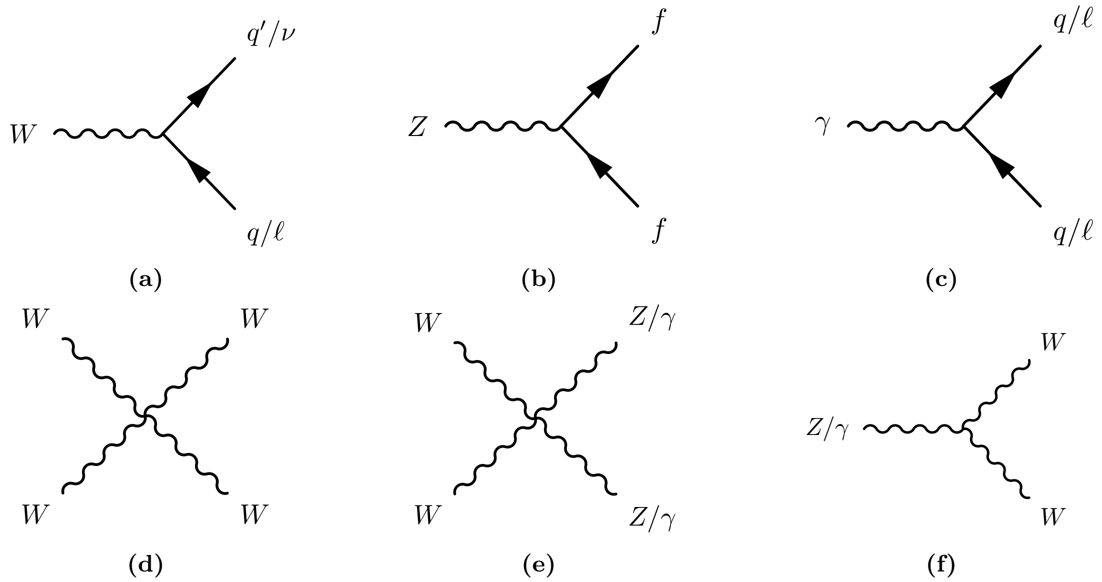

Figure 1.2: Possible vertices in the electroweak interaction.

to the physical $W^{\pm}$, Z and γ bosons in the electroweak theory

$$\begin{aligned} W^{\pm}_{\mu} &= \frac{1}{\sqrt{2}}(W^1_{\mu} \mp iW^2_{\mu}) && \text{with} \quad m_W = \frac{g_2}{2}v, \\ Z_{\mu} &= \frac{1}{\sqrt{g_1^2+g_2^2}}(g_2 W^3_{\mu} - g_1 B_{\mu}) && \text{with} \quad m_Z = \frac{\sqrt{g_1^2+g_2^2}}{2}v, \\ A_{\mu} &= \frac{1}{\sqrt{g_1^2+g_2^2}}(g_1 W^3_{\mu} + g_2 B_{\mu}) && \text{with} \quad m_A = 0. \end{aligned}$$

It is worth noting, that the massless photon field A_{μ} associated with the electromagnetic $U(1)_{\text{em}}$ gauge symmetry is automatically recovered. All possible vertices between fermions and the physical electroweak gauge bosons are shown in fig. 1.2 The change of basis from (W^3_{μ}, B_{μ}) to (Z_{μ}, A_{μ}) [2] can also be written as a basis rotation with the weak mixing angle θ_W

Write somewhere SU2xU1 to U1 breakdown

$$\begin{pmatrix} Z_{\mu} \\ A_{\mu} \end{pmatrix} = \begin{pmatrix} \cos\theta_W & \sin\theta_W \\ -\sin\theta_W & \cos\theta_W \end{pmatrix} \begin{pmatrix} W^3_{\mu} \\ B_{\mu} \end{pmatrix} \quad \text{with } \cos\theta_W = \frac{g_2}{\sqrt{g_1^2+g_2^2}} = \frac{m_W}{m_Z}. \tag{1.41}$$

In the SM, not only the $W^{\pm}$ and Z bosons but also fermions gain their masses through spontaneous breaking of the electroweak gauge symmetry. Fermion fields gain masses through gauge-invariant Yukawa interactions with the Higgs field. For one fermion generation, the respective Yukawa terms in the Lagrangian are

$$\mathcal{L}_{\text{Yukawa,gen}} = -\lambda_{\ell}\bar{L}_{\text{L}}\Phi\ell_{\text{R}} - \lambda_d\bar{Q}_{\text{L}}\Phi d_{\text{R}} - \lambda_u\bar{Q}_{\text{L}}\Phi^{\dagger}u_{\text{R}} + \text{h.c.}, \tag{1.42}$$

where λ_f with $f = \ell, d, u$ are the dimensionless Yukawa couplings and $L_{\text{L}} = (\nu_{\text{L}}, \ell_{\text{L}})^T$ and $Q_{\text{L}} = (u_{\text{L}}, d_{\text{L}})^T$ are the left-handed lepton and quark doublets, respectively. The VEV of the

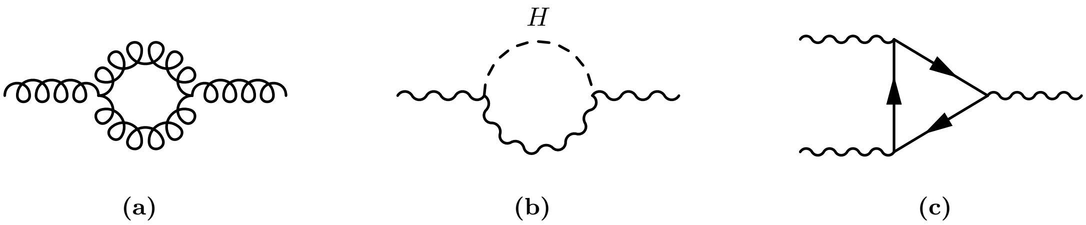

Figure 1.3: Examples of loops corrections to (a) the gluon propagator, (b) the W or Z propagator and (c) the cubic gauge boson vertex.

Higgs field then gives rise to fermion mass terms in the Lagrangian, which, in the unitary gauge, reads for a single fermion generation

$$\mathcal{L}_{\text{Yukawa,gen}} = -\sum_{f=\ell,d,u} \left(m_f \bar{\psi}_f \psi_f + \frac{m_f}{v} H \bar{\psi}_f \psi_f \right) \qquad \text{with} \quad m_f = \frac{1}{\sqrt{2}} \lambda_f v. \tag{1.43}$$

When introducing all three fermion generations, additional Yukawa terms mixing fermions of different generations appear in the Lagrangian. The terms involving quark fields can be parametrised using the Cabibbo–Kobayashi–Maskaw (CKM) matrix V_{CKM} [8, 9], quantifying the transition probability between quark generations. Since no right-handed neutrinos exist in the SM, no generation mixing in the lepton sector occurs and hence no neutrino mass terms are allowed in the SM. Neutrino oscillations have however been observed experimentally, thus at least one massive neutrino generation needs to exist. Their mixing can then be described with the Pontecorvo-Maki-Nakagawa-Sakata (PMNS) matrix [7], allowing neutrinos to acquire mass e.g. through the see-saw mechanism [31].

1.1.3 Renormalisation and divergencies

At lowest order in the perturbative expansion, the momenta of the internal lines in the Feynman diagrams are fixed by the external particles. For higher orders where the diagrams involve loops, the momenta of the internal lines need to be integrated over as they are not fixed by energy-momentum conservation. Some examples of loop corrections to propagators and vertices are shown in fig. 1.3. As each vertex in the Feynman diagrams is associated with a coupling constant that is usually smaller than 1 (apart from the non-perturbative regime of QCD), higher orders in the perturbative expansion contribute less and less to the total amplitude of the full expansion.

The momentum integrals in loop corrections however lead to *ultraviolet divergencies* for large momenta. In order to eliminate the divergencies, the integrals have to be *regularised*, e.g. by applying a cut-off scale Λ or calculating the integrals in a number $D = 4-\epsilon$ of dimensions where they converge. The potential divergencies are then absorbed in parameters of the Lagrangian, such as coupling constants and masses, after which the regulator is removed (e.g. $\epsilon \to 0$) again and a *renormalisation* procedure is applied, replacing the bare parameter values with the physical, measured values. Renormalisation effectively absorbs the effects of quantum fluctuations acting on much smaller scales than the scale of the given problem in the parameters of the theory. As Veltmann and t'Hooft [32, 13] have shown in the early 1970s, all Yang-Mills

Mass dimension needs to be < 4

theories with massive gauge fields are renormalizable, making the SM as a whole a renormalizable theory.

1.2 Supersymmetry

Among the properties a quantum field theory might possess to make it more mathematically tractable, one specific higher symmetry reveals particularly far-reaching implications; a symmetry relating fermions and bosons, known as *supersymmetry* (SUSY). The following section introduces the basic concepts, a promising class of theories that turns out solving some of the shortcomings of the SM.

First, a motivation for the need of SUSY is given by highlighting some of the open questions of the SM, followed by an introduction to the mathematical description and phenomenological consequences of supersymmetric theories. This section is intended to highlight the most important concepts and relations, a complete and detailed introduction to SUSY can e.g. be found in [3].

1.2.1 Shortcomings of the SM

Although the SM is a wildly successful theory able to predict and describe the interactions between elementary particles with unprecedented precision, there are still phenomena in nature that cannot be suitable understood with the SM. Those limitations and open questions are the reason for numerous searches looking for new physics beyond the Standard Model (BSM). Some of these open questions are described in the following.

Dark Matter

The existence of Dark Matter (DM), i.e. non-luminous and non-absorbing matter is nowadays well established [5]. Some of the earliest hints for the existence of DM came from the observation that the rotation curves of luminous objects were not consistent with the expected velocities based on the gravitational attraction of the visible objects around them. Zwicky already postulated in 1933 the existence of DM [33] based on rotation curves of galaxies in the Coma cluster. In 1970, Rubin measured rotation curves of spiral galaxies [34], revealing again a significant disagreement with the theoretically expected curves given the visible matter in the galaxies. Based on Newtonian dynamics, the circular velocity of stars outside the bulge of galaxies is expected to fall off with increasing radius as $v(r) \propto 1/\sqrt{r}$ [35]. Rubin's observations showed however that the velocities of stars outside the bulge stay approximately constant, strongly suggesting the existence of a non-luminous (or *dark*) halo around the galaxies. Surveys of galaxy clusters and obervations of gravitational lensing effects observed in e.g. the bullet cluster [36] or the Abell 1689 cluster [37] have since then further consolidated the existence of large accumulations of non-luminous mass in the universe.

The anisotropies in cosmic microwave background (CMB), studied by the COBE [38, 39], WMAP [40, 41] and Planck missions [42] are very well described by the Lambda Cold Dark Matter model (ΛCDM) [43], which includes a density for cold dark matter. Planck's latest

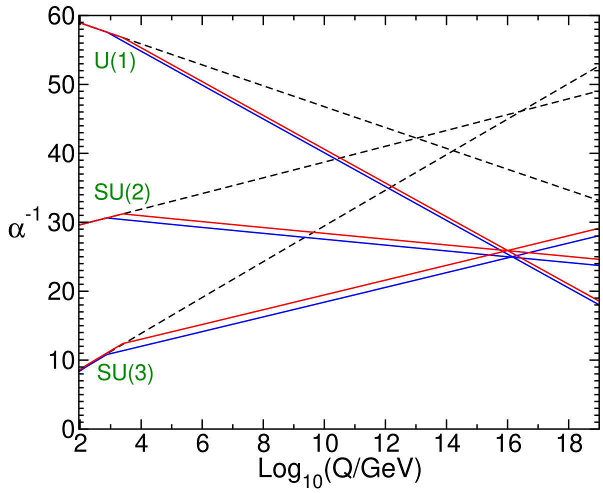

Figure 1.4: Evolution of the inverse coupling constants in the SM (dashed lines) and the MSSM (solid lines) in function of the energy scale Q. In the MSSM, the masses of the supersymmetric particles are treated as common threshold varied between 750 GeV and 2.5 TeV. Figure taken from [3].

results [44] suggest that the matter density of the universe is $\Omega_m = 0.3111 \pm 0.0056^{\dagger}$ and that ordinary baryonic matter only takes up $\sim 4.9\%$ of the universe, while DM accounts to $\sim 26.1\%$. DM relic density

Candidates for non-baryonic DM need to satisfy certain conditions: they have to be stable on cosmological timescales (otherwise they would have decayed by now), they have to couple only very weakly to the electromagnet interaction (otherwise they would be luminous matter) and they have to have the right relic density. Analyses of structure formations in the Universe have furthermore shown that most DM should have been *cold*, i.e. non-relativistic at the beginning of galaxy formation [35]. Candidates for DM particles are e.g. sterile neutrinos, axions, primordial black holes, or weakly interacting massive particles (WIMPs).

In the SM, the only DM candidate particle is the neutrino. Given the upper limits on the neutrino masses, an upper bound on their relic density can be computed, revealing that neutrinos are simply not abundant enough to be a dominant component of DM [35]. Many BSM theories naturally predict new WIMPs with masses in the GeV to TeV range. In many SUSY models with exact R-parity conservation (see section 1.2.5), the lightest supersymmetric particle is neutral and stable and might indeed be an ideal candidate for DM.

Unification of forces

Apart from the non-perturbative low-energy behaviour of QCD, the SM as a $SU(3)_C \otimes SU(2)_\mathrm{L} \otimes U(1)_Y$ gauge theory apparently gives a complete picture of nature up to the energy scale probed with today's accelerators. However, some peculiar aspects of the SM hint to a more fundamental theory. A prominent example is the question why the electric charges of the electrons and the charges of the quarks of the protons and neutrons in the nuclei exactly cancel, making for electrically neutral atoms [1]. Or in other words: why are the charges of all observed particles simple multiples of the fundamental charge?

An explanation to many of these peculiarities comes naturally when describing the SM as a unified theory with a single non-Abelian gauge group, usually taken to be $SU(5)$ [45]. The larger symmetry group with a single coupling constant is then thought to be spontaneously

† The remaining $\sim 69\%$ are taken up by *dark energy*, whose nature is still an open question.

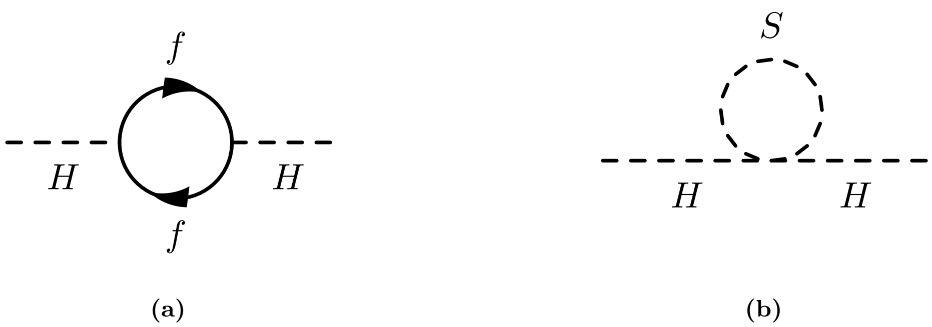

Figure 1.5: A massive fermion (a) and a hypothetical massive scalar particle (b) coupling to the Higgs boson.

broken at very high energy, such that the known SM interactions are recovered at lower energies. In such a grand unified theory (GUT), the particles in the SM are arranged in anomaly-free irreducible representations of the gauge group, thereby e.g. naturally ensuring the fractional charges of quarks [2].

explain anomaly cancellations

In the SM, the coupling constants run towards each other with increasing energy scale, but never exactly meet. In the Minimal Supersymmetric Standard Model (MSSM) with supersymmetric particles at the TeV scale the running couplings meet within their current uncertainties. Figure 1.4 shows the running of the coupling constants in both the SM and the MSSM.

The Hierarchy Problem

As the SM is a renormalizable gauge theory, finite results are obtained for all higher-order loop corrections, making the SM a theory that is well-defined up to infinite energies. In renormalisation terms, this means that the cut-off scale Λ is theoretically allowed to go to infinity. It is however clear, that the SM cannot be a complete theory of nature and that at some unknown high-energy scale Λ, *new physics* has to appear. At the very least, a new theoretical framework becomes necessary at the Planck scale $M_P \approx 10^{18}\,\mathrm{GeV}$ [3], where quantum gravitational effects can no longer be ignored.

The mass parameters of fermions and massive vector bosons are protected from large quantum corrections by chiral symmetry and gauge symmetry, respectively [46]. The mass parameter of the scalar Higgs field, on the other hand, gets loop corrections proportional at least to the scale at which new physics sets in. The coupling of the Higgs field to a fermion f with mass m_f, depicted in fig. 1.5(a), yields a one-loop correction term to the Higgs square mass [3] given by

$$\Delta m_H^2 = -\frac{|\lambda_f|^2}{8\pi^2}\Lambda^2 + \dots\,. \tag{1.44}$$

Thus, in order to obtain the relatively low value of the Higgs mass in the order of $10^2\,\mathrm{GeV}$, the quantum corrections to the bare Higgs parameter have to be tuned in such a way that they almost cancel. Hence, if there is *any* scale of new physics even only several orders of magnitude higher than the electroweak scale, the large quantum corrections to the Higgs mass immediately lead to a *fine-tuning* problem that is considered to be unnatural.

In SUSY, the Higgs mass is automatically protected from the large quantum corrections by the introduction of two complex scalar partners to each SM fermion. The quantum corrections from the a hypothetical heavy complex scalar particle S with mass m_S as in fig. 1.5(b) yields a one-loop correction [3] given by

$$\Delta m_H^2 = \frac{\lambda_S}{16\pi^2}\left[\Lambda^2 + 2m_S^2 \log\left(\Lambda/m_S\right) + \dots\right]. \tag{1.45}$$

Interestingly, the corrections in eq. (1.44) and eq. (1.45) enter with opposite signs. Thus, if $\lambda_S = |\lambda_f|^2$, then the large quantum corrections neatly cancel and no excessive fine-tuning is needed. The requirement $\lambda_S = |\lambda_f|^2$ means that the fermions and their supersymmetric bosonic partners would have same masses. Such particles would have been discovered long ago in particle physics experiments, meaning that SUSY must be a broken symmetry (see section 1.2.5) such that the supersymmetric particles acquire masses well above their SM partners.

Anomalous magnetic moment of the muon

One of the longest standing disagreements between experiment and theory in the SM is the anomalous magnetic moment of the muon. The magnetic moment of the muon $\vec{\mu}_\mu$ is related to its intrinsic spin $\vec{S}$ through the gyromagnetic ratio g_μ by

$$\vec{\mu}_\mu = g_\mu \frac{q}{2m}\vec{S}. \tag{1.46}$$

For a structureless spin-1/2 particle with mass m and charge $q = \pm e$, the gyromagnetic ratio is $g_\mu = 2$ [47]. Loop corrections coupling the muon spin to virtual fields cause small deviations, parameterised by the anomalous magnetic moment

$$a_\mu = \frac{1}{2}(g_\mu - 2). \tag{1.47}$$

The anomalous magnetic moment can be precisely measured as well as predicted within the SM, a comparison between experimental data and theoretical prediction thus directly tests the SM at quantum loop level and may hint to effects from new physics in case of discrepancies [48]. In the SM, the most dominant contribution to a_μ comes from QED corrections involving photon and fermion loops. An exemplary diagram is shown in fig. 1.6(a). Weak contributions involving the heavy $W^\pm$, Z and Higgs particles are relatively suppressed due to their mass [5]. Although the contributions from QCD are relatively small, they give rise to the main theoretical uncertainties as they are not calculable from first principles [5].

The E821 experiment at Brookhaven National Lab (BNL) [47] has measured the anomalous magnetic moment of the muon and found a deviation from the SM expectation of

$$\Delta a_\mu = a_\mu^{\text{exp}} - a_\mu^{\text{SM}} = 261(63)(48) \times 10^{-11}, \tag{1.48}$$

where the numbers in parentheses are the uncertainties from experiment and theory, respectively. This represents a deviation of 3.3σ [5] from the SM expectation.

In SUSY, additional Feynman diagrams exist involving the supersymmetric partners of the muon, the muon neutrino and the electroweak gauge bosons, and thus the measured deviation

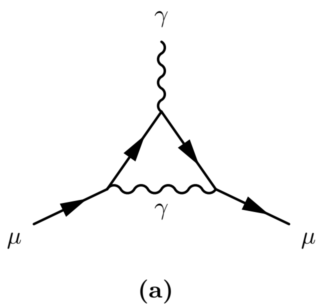

Figure 1.6: Electromagnetic (a) and supersymmetric (b), (c) contributions to a_μ. Adapted from [48].

in a_μ can easily be accommodated in many supersymmetric models [49, 50]. Two exemplary lowest-order diagrams involving supersymmetric particles is shown in figs. 1.6(b) and 1.6(c).

1.2.2 Supersymmetric Algebra

A generator of supersymmetric transformations is an anti-commuting spinor Q that turns fermionic states $|f\rangle$ into bosonic states $|b\rangle$ and vice-versa.

$$Q\,|f\rangle = |b\rangle\,, \qquad\qquad Q\,|b\rangle = |f\rangle\,. \tag{1.49}$$

As spinors are complex objects, $Q^\dagger$ is also a symmetry operator. Both Q and $Q^\dagger$ are necessarily fermionic and thus must carry half-integer spin, in the simplest case spin-1/2, meaning that SUSY must be a spacetime symmetry, i.e. a Poincaré symmetry. The Coleman-Mandula theorem [51] dictates that the symmetry group generating a consistent spacetime quantum field theory must be the direct product of the internal symmetry group with the Poincaré group, which in principle rules out the possibility for SUSY. The Haag-Lopuszanski-Sohnius extension [52] however states that the only possible way of non-trivially combining internal and spacetime symmetry groups is to use a Lie superalgebra and fermionic spin-1/2 generators. Thus, in order to obey the Haag-Lopuszanski-Sohnius theorem and simultaneously allow for parity-violating interactions, the SUSY generators have to satisfy the following algebra of commutation and anti-commutation relations [53].

$$\begin{aligned}
\{Q, Q^\dagger\} &= 2\sigma_\mu P^\mu, \\
\{Q, Q\} &= \{Q^\dagger, Q^\dagger\} = 0, \\
[P^\mu, Q] &= \left[P^\mu, Q^\dagger\right] = 0, \\
\{M^{\mu\nu}, Q\} &= \sigma^{\mu\nu} Q, \\
\{M^{\mu\nu}, Q^\dagger\} &= \bar{\sigma}^{\mu\nu} Q^\dagger,
\end{aligned} \tag{1.50}$$

where P^μ is the four-momentum generator of spacetime translations, $\sigma_\mu = (\mathbb{1}_2, \sigma_i)$, $\bar{\sigma}_\mu = (\mathbb{1}_2, -\sigma_i)$ with $i = 1, 2, 3$ and the Pauli matrices σ_i, and $\sigma^{\mu\nu} = \frac{i}{4}(\sigma^\mu\bar{\sigma}^\nu - \sigma^\nu\bar{\sigma}^\mu)$ as well as $\bar{\sigma}^{\mu\nu} = \frac{i}{4}(\bar{\sigma}^\mu\sigma^\nu - \bar{\sigma}^\nu\sigma^\mu)$. This is the simplest version of SUSY, called $N = 1$ symmetry, as it introduces only one pair of generators. Supersymmetric theories with $N \geq 2$ pairs of generators also exist and generally have some theoretical advantages as e.g. fewer divergencies in the case of $N = 2$ or even no divergencies at all in the case of $N = 4$ [53]. SUSY models with

$N \geq 2$ however do not allow for parity violation and thus fail to describe the physics of the SM, disqualifying them from an experimental point of view [53].

As both SUSY generators commute with spacetime translations (see eq. (1.50)), they also both commute with the squared mass operator $-P^2$. Consequently, particles related by the generators, called *superpartners*, must have equal eigenvalues under $-P^2$, i.e. equal masses. Furthermore, the SUSY generators also commute with the gauge transformation generators, hence superpartners must have same electric charge, weak isospin and degrees of freedom in colour space [3].

Mention link to gravity

1.2.3 Supermultiplets

The SM and SUSY particles are arranged in irreducible representations of the SUSY algebra, called *supermultiplets*, that each contain both fermionic and bosonic states, that are superpartners of each other. It can be shown that each supermultiplet has an equal number of fermion and boson degrees of freedom, $n_f = n_b$ [3].

The simplest supermultiplet Ψ that can be constructed contains a single Weyl fermion *psi* and two real scalars, described by a single complex field *phi*, called the *sfermion*. The Weyl fermion has two spin helicity states, hence $n_f = 2$, and the complex scalar field has two components with $n_b = 1$ each. An additional complex scalar field F, called *auxiliary field* and not corresponding to a physical particle, has to be introduced in order to allow the SUSY algebra to close off-shell [3]. The supermultiplet Ψ thus reads

$$\Psi = (\phi, \psi, F). \tag{1.51}$$

Being a pure bookkeeping device, the auxiliary field does not propagate and can be eliminated on-shell with the equations of motion $F = F^* = 0$. This supermultiplet is called a *chiral* or *scalar* supermultiplet.

The next-simplest supermultiplet for which $n_f = n_b$ holds, is the *vector* or *gauge* supermultiplet Φ containing a spin-1 gauge boson A_a^μ, where a is the index of the gauge group. In order for the theory to be renormalizable, this gauge boson must be massless before spontaneous breaking of the symmetry. As a massless spin-1 boson has two helicity states, $n_b = 2$, the superpartner, called *gaugino*, must be a massless spin-1/2 Weyl fermion λ_a with two helicity states, $n_f = 2$ [3]. An auxiliary real bosonic field D_a is needed in order to balance the degrees of freedom off-shell [53], completing the supermultiplet to be

$$\Phi = (\lambda_a, A_a^\mu, D_a). \tag{1.52}$$

Like the chiral auxiliary field, the gauge auxiliary field does not correspond to a physical particle and can be eliminated on-shell through its equations of motion [3].

1.2.4 Supersymmetric Lagrangian

The simplest supersymmetric model that can be shown to realise the superalgebra is the massless, non-interacting Wess-Zumino model [54, 3], given by

$$\begin{aligned}\mathcal{L}_{\text{free}} &= \mathcal{L}_{\text{scalar}} + \mathcal{L}_{\text{fermion}} \\ &= \partial^\mu \phi^* \partial_\mu \phi + i\psi^\dagger \bar{\sigma}^\mu \partial_\mu \psi,\end{aligned} \tag{1.53}$$

with a massless complex scalar ϕ and a spin-1/2 fermion ψ, corresponding to a single chiral supermultiplet. As discussed in section 1.2.3, in order for this Lagrangian to satisfy the supersymmetry off-shell where the equations of motion cannot be used, an auxiliary complex scalar field F has to be added. For a collection of i chiral supermultiplets, the free Lagrangian reads

$$\begin{aligned}\mathcal{L}_{\text{free}} &= \mathcal{L}_{\text{scalar}} + \mathcal{L}_{\text{fermion}} + \mathcal{L}_{\text{aux}} \\ &= \partial^\mu \phi^{*i} \partial_\mu \phi_i + i\psi^{\dagger i} \bar{\sigma}^\mu \partial_\mu \psi_i + F^* i F_i,\end{aligned} \tag{1.54}$$

where the repreated indices i are summed over. The auxiliary Lagrangian term $\mathcal{L}_{\text{aux}}$ implies the trivial equations of motion $F = F^* = 0$ which are needed to remove the auxiliary field in the on-shell case. The next step involves adding terms for non-gauge interactions for the chiral supermultiplets It can be shown that the most general non-gauge interactions for chiral supermultiplets are determined by a holomorphic[†] function of the complex scalar fields, called the *superpotential* W [3, 53], which reads

$$W = \frac{1}{2} m^{ij} \phi_i \phi_j + \frac{1}{6} y^{ijk} \phi_i \phi_j \phi_k, \tag{1.55}$$

with y^{ij} the Yukawa couplings between the scalars and fermions. The superpotential can at most be cubic in order for the final Lagrangian to be renormalizable [53]. The requirement that the interaction part of the Lagrangian be invariant under supersymmetry transformations further defines the potential V. The equations of motions of the auxiliary fields F can be written as

$$F_i = \frac{\partial W(\phi)}{\partial \phi^i} = -W_i^*, \qquad F^{*i} = -\frac{\partial W(\phi)}{\partial \phi_i} = -W^i, \tag{1.56}$$

which thus yields for the potential $V = W_i^* W^i = F_i F^{*i}$. The full Lagrangian of the Wess-Zumino model with general chiral interactions for i chiral supermultiplets is then given [3] by

$$\mathcal{L} = \partial^\mu \phi^{*i} \partial_\mu \phi_i + i\psi^{\dagger i} \bar{\sigma}^\mu \partial_\mu \psi_i + \frac{1}{2} m^{ij} \psi_i \psi_j + \frac{1}{2} m^*_{ij} \psi^{\dagger i} \psi^{\dagger j} + \frac{1}{2} y^{ijk} \phi_i \psi_j \psi_k + \frac{1}{2} y^*_{ijk} \phi^{*i} \psi^{\dagger j} \psi^{\dagger k} + V. \tag{1.57}$$

The Lagrangian in eq. (1.57) immediately reveals that, as expected by supersymmetry, the masses of the fermions and bosons in the same supermultiplet are identical. In order to incorporate gauge supermultiplets and consider the interactions between fermions and gauge bosons observed in the SM, the usual minimal coupling rule has to be applied, replacing ∂_μ

[†] A holomorphic function is a complex-valued function in one or more complex variables that is complex differentiable in a neighbourhood for every point of its domain.

with D_μ. This leads to equation of motions for the auxiliary fields D^a

$$D^a = -g(\phi^* T^a \phi), \tag{1.58}$$

where T^a are the generators of the gauge group and g is the coupling constant [3]. The potential then becomes

$$V = F^{*i} F_i + \frac{1}{2} \sum_a D^a D^a = W_i^* W^i + \frac{1}{2} \sum_a g_a^2 (\phi^* T^a \phi)^2, \tag{1.59}$$

where a runs over the gauge groups that in general have different gauge couplings [3, 53].

1.2.5 The Minimal Supersymmetric Standard Model

The Minimal Supersymmetric Standard Model (MSSM) is the simplest supersymmetrisation of the SM in the sense that it introduces a minimal set of additional particles.

Particle content and interactions

The MSSM arranges all SM particles in one chiral (all the fermions and quarks) and one gauge (all spin-1 bosons) supermultiplet. As supersymmetric partners (*spartners*) have the same quantum numbers apart from spin, none of the SM particles can be spartners of each other. Thus, all spartners have to be new, unseen particles. Table 1.3 summaries the names, notations and spins of all spartners introduced in the MSSM. The naming convention is to prepend the names of the spartners of fermions with an 's' (e.g. *selectron*, *stop*, ...) and append '-ino' to the names of the spartners of the bosons (e.g. *Wino*, *Higgsino*, ...). Supersymmetric particles (*sparticles*) are generally denoted by adding a tilde to the symbol of SM particles (e.g. $\tilde{e}$, $\tilde{u}$, $\tilde{g}$, ...).

An important detail to note is that right-handed and left-handed fermions get their own chiral supermultiplets and thus have distinct spartners, as otherwise the preference of the weak interaction for left-handed particles would be violated. For example, left-handed and right-handed quarks (q_L, q_R) get two different spartners ($\tilde{q}_\mathrm{L}$, $\tilde{q}_\mathrm{R}$), denoted with an index L and R, which refers to the handedness of the SM particle as scalar particles have only one helicity state. Additionally, the spartners of the left-handed and right-handed will mix to form physical mass eigenstates.

It is also worth asking why the spartners of SM particles are of lower spin in the first place, as e.g. spin-1 spartners of the SM fermions could also have been considered. The MSSM being minimal, this would not be possible as the introduction of spin-1 bosons would entail the introduction of new gauge interactions. Furthermore, introducing spartners with spin greater than 1 would make the resulting theory non-renormalizable [53].

In the MSSM, two Higgs doublets are needed in order to give masses to the up-type and down-type quarks via Yukawa couplings. A single Higgs field h cannot be used for this as it would require Yukawa terms including the complex conjugate h^* of the Higgs field, which is forbidden as the superpotential, being a holomorphic function of the fields, cannot depend on the complex conjugates of the same fields [53]. Additionally, the use of a single Higgs doublet would lead to gauge anomaly in the electroweak gauge symmetry [55]. Instead two complex

Table 1.3: Particle content of the MSSM. The spin refers to the spin of the spartner. Adapted from [53].

Particle	Spartner 0	Spin
quarks q	squarks $\tilde{q}$	0
$\rightarrow$ top t	stop $\tilde{t}$	
$\rightarrow$ bottom t	sbottom $\tilde{b}$	
...		
leptons ℓ	sleptons $\tilde{\ell}$	0
$\rightarrow$ electron e	selectron $\tilde{e}$	
$\rightarrow$ muon μ	smuon $\tilde{\mu}$	
$\rightarrow$ tau τ	stau $\tilde{\tau}$	
$\rightarrow$ neutrinos ν_ℓ	stop $\tilde{\nu}_\ell$	
gauge bosons	gauginos	1/2
$\rightarrow$ photon γ	photino $\tilde{\gamma}$	
$\rightarrow$ boson Z	Zino $\tilde{Z}$	
$\rightarrow$ boson B	Bino $\tilde{B}$	
$\rightarrow$ boson W	Wino $\tilde{W}$	
$\rightarrow$ gluon g	gluino $\tilde{g}$	
Higgs bosons $H_i^{\pm,0}$	higgsinos $\tilde{H}_i^{\pm,0}$	1/2

Higgs doublets with hypercharge $Y = +1/2$ and $Y = -1/2$ are used in the MSSM. The two Higgs doublets can be written as

$$H_u = \begin{pmatrix} H_u^0 \\ H_u^- \end{pmatrix}, \qquad H_d = \begin{pmatrix} H_d^+ \\ H_d^0 \end{pmatrix}, \tag{1.60}$$

As illustrated in section 1.2.4 using the Wess-Zumino model, interactions are introduced using the superpotential. In the MSSM, the superpotential reads

$$W_{\mathrm{MSSM}} = \bar{u}\boldsymbol{y_u}QH_u - \bar{d}\boldsymbol{y_d}QH_d - \bar{e}\boldsymbol{y_e}LH_d + \mu H_u H_d, \tag{1.61}$$

where Q and L correspond to the supermultiplets containing the left-handed quarks and leptons as well as their spartners, respectively, and $\bar{u}$, $\bar{d}$, $\bar{e}$ correspond to the supermultiplets containing the right-handed up-type quarks, down-type quarks and leptons as well as their spartners, respectively. The parameters $\boldsymbol{y_u}$, $\boldsymbol{y_d}$ and $\boldsymbol{y_e}$ are the 3×3 Yukawa coupling matrices. Except for the third generation, the Yukawa couplings are already known to be relatively small [3] and are thus not of direct interest for the phenomenology of the theory. Phenomenologically more interesting are the supersymmetric gauge interactions that dominate the production and decay process of spartners in the MSSM [3]. The superpotential in eq. (1.61) illustrates again why two Higgs doublets are needed in the MSSM, since terms like $\bar{u}QH_d^*$ or $\bar{e}LH_u^*$ are not allowed due to the holomorphism of the superpotential. The term $\mu H_u H_d$ contains the *higgsino mass parameter* μ and is the supersymmetric version of the Higgs mass term in the SM Lagrangian.

Soft supersymmetry breaking

As stated in section 1.2.2, all superpartners must have same quantum numbers apart from their spin. They especially also should have same masses, however such particles would have been discovered a long time ago and thus SUSY must be broken. Formally, SUSY should thus be an exact symmetry that is spontaneously broken because the Lagrangian has a symmetry under which the vacuum state is not invariant. However, if broken SUSY is still to provide a solution to the Hierarchy problem, i.e. cancel the quadratic divergencies in the loop corrections for the Higgs mass parameter, then the relations between the dimensionless couplings of the SM particles and their superpartners have to be maintained [3]. Hence, only symmetry breaking terms with positive mass dimension are allowed in the Lagrangian, especially also forbidding the presence of dimensionless SUSY-breaking couplings [3]. Such a breaking of SUSY is called *soft* breaking and can be written as

$$\mathcal{L} = \mathcal{L}_{\text{SUSY}} + \mathcal{L}_{\text{soft}}. \tag{1.62}$$

where, $\mathcal{L}_{\text{soft}}$ contains all the symmetry breaking terms while $\mathcal{L}_{\text{SUSY}}$ is the SUSY invariant Lagrangian with all the gauge and Yukawa interactions. In a softly broken SUSY, the loop corrections to the Higgs mass parameter depend quadratically on the largest mass scale associated with the soft terms (m_{soft}). As the fine-tuning problem reappears if m_{soft} becomes too large, superpartners with masses not far above the TeV scale are generally assumed.

A total of 105 new parameters with no counterpart in the SM are introduced through $\mathcal{L}_{\text{soft}}$ [3, 56]:

- gaugino mass parameters M_1, M_2 and M_3,
- trilinear scalar couplings, parametrized by 3×3 matrices in generation space $\boldsymbol{a_u}$, $\boldsymbol{a_d}$, $\boldsymbol{a_e}$, representing Higgs-squark-squark and Higgs-slepton-slepton interactions,
- Hermitian 3×3 matrices in generation space $\boldsymbol{m^2_Q}$, $\boldsymbol{m^2_{\bar{u}}}$, $\boldsymbol{m^2_{\bar{d}}}$, $\boldsymbol{m^2_L}$, $\boldsymbol{m^2_{\bar{e}}}$ that represent the sfermion masses,
- SUSY breaking parameters $m^2_{H_u}$, $m^2_{H_d}$ and b.

The sfermion mass matrices and the trilinear scalar couplings may introduce additional flavour mixing and CP violation, both of which are heavily constrained by experimental results. Flavour mixing in the lepton sector is for example constrained by an upper limit on $\text{BR}(\mu \to e\gamma) < 4.2 \times 10^{-12}$ [57]. Bounds on additional CP violation as well as squark mixing terms come from measurements of the electron and neutron electric moments and neutral meson systems[†]. citation? Formally, in order to avoid these terms, SUSY breaking can be assumed to be *flavour-blind*, meaning that the mass matrices are approximately diagonal. The large Yukawa couplings for the third generation squarks and sfermions can then be achieved by assuming that the trilinear scalar couplings are proportional to the corresponding Yukawa coupling matrix.

As most of the parameters in the MSSM are related to soft SUSY breaking, it is not surprising that the phenomenology of the MSSM strongly depends on the exact breaking mechanism. The breaking is usually introduced to happen in a *hidden sector* and the effects of the breaking

[†] It is of course still possible to fine-tune the numerous phases in the MSSM, creating cancelling contributions

are then typically mediated by messenger particles from a messenger field to the *visible sector* containing all the particles of the MSSM. Since the hidden sector is assumed to be only coupled weakly or indirectly to the visible sector, the phenomenology mostly depends on the mechanism mediating the breaking. The two most popular mechanisms are *gravity-mediated* and *gauge-mediated* SUSY breaking.

Mediating SUSY breaking through gravity is an attractive approach, since all particles share gravitational interactions. This makes it easy to imagine gravitational effects to be the only connection between the hidden and the visible sectors. In such models SUSY breaking is mediated through effects of gravitational strength, suppressed by inverse powers of the Plack mass [5]. The gravitino mass is typically of electroweak scale [58, 59]. Due to its couplings of gravitational strengths, it typically does not play a role in collider physics [5].

In gauge-mediated SUSY breaking (GMSB), additional messenger fields sharing gauge interactions with the MSSM fields are transmitting the breaking from the hidden to the visible sector. In such models, the gravitino is typically the LSP, as its mass ranges from a few eV to a few GeV, making it a candidate for DM [60].

Mass spectrum

In the MSSM, electroweak symmetry breaking is generalised to the two Higgs doublets introduced in eq. (1.60). In total, the two doublets have eight degrees of freedom, three of which are used up to give masses to the $W^\pm$ and Z bosons during the breaking of $SU(2)_\mathrm{L} \otimes U(1)_Y$ to $U(1)_\mathrm{em}$ (see section 1.1.2). Thus, five physical Higgs bosons appear in the MSSM; two neutral Higgs bosons even under CP transformation called h^0, one neutral Higgs boson odd under CP transformation called A^0 and finally two charged Higgs bosons called $H^\pm$. The two Higgs doublets H_u and H_d each get a VEV (v_u and v_d, respectively) that are connected to the VEV v of the SM Higgs field by

$$v_u^2 + v_d^2 = v^2. \tag{1.63}$$

Phenomenologically, the ratio of the two VEVs is usually considered, conventionally called $\tan\beta$,

$$\tan\beta = \frac{v_u}{v_d}. \tag{1.64}$$

Due to electroweak symmetry breaking, the gauginos and higgsinos are not mass eigenstates but mix to form states with definite mass, called *electroweakinos*:

- the two charged higgsinos mix with the two charged winos to form two charged mass eigenstates $\tilde{\chi}_1^\pm$, $\tilde{\chi}_2^\pm$, called *charginos*,
- the remaining neutral higgsinos mix with the photino, zino and bino to form four neutral mass eigenstates $\tilde{\chi}_1^0$, $\tilde{\chi}_2^0$, $\tilde{\chi}_3^0$, $\tilde{\chi}_4^0$, called *neutralinos*.

Both charginos and neutralinos are by convention labeled in ascending mass order. In the gauge-eigenstate basis $\psi^0 = (\tilde{B}, \tilde{W}^0, \tilde{H}_d^0, \tilde{H}_u^0)$, the neutralino mixing matrix reads [3]

$$\boldsymbol{M}_{\tilde{\chi}}^0 = \begin{pmatrix} M_1 & 0 & -g_1 v_d/\sqrt{2} & g_1 v_u/\sqrt{2} \\ 0 & M_2 & g_2 v_d/\sqrt{2} & -g_2 v_u/\sqrt{2} \\ -g_1 v_d/\sqrt{2} & g_2 v_d/\sqrt{2} & 0 & -\mu \\ g_1 v_u/\sqrt{2} & -g_2 v_u/\sqrt{2} & -\mu & 0 \end{pmatrix}, \tag{1.65}$$

where M_1 and M_2 stem directly from the soft SUSY breaking terms while the $-\mu$ terms are the higgsino mass terms. Entries with g_1 and g_2 come from Higgs-higgsino-gaugino couplings. The neutralino mixing matrix can be diagonalized to obtain the neutralino masses, which can be expressed in terms of the parameters M_1, M_2, μ and $\tan\beta$ [3]. As the exact forms of the mass expressions are relatively complicated, they are typically evaluated in limits where one of the mass parameters is significantly smaller than the other two. This is possible because M_1 and M_2 can be chosen to be real and positive through an appropriate phase redefinition of $\tilde{B}$ and $\tilde{W}$[†]. If neutralinos are dominated the wino, bino or higgsino component, they are called wino-, bino- or higgsino-like in the following.

The chargino mixing matrix can be written in a similar fashion. In the gauge-eigenstate $\psi^\pm = (\tilde{W}^\pm, \tilde{H}_u^+, \tilde{W}^-, \tilde{H}_d^-)$, it can be written as

$$\boldsymbol{M}_{\tilde{\chi}^\pm} = \begin{pmatrix} \mathbb{0}_2 & \boldsymbol{X}^T \\ \boldsymbol{X} & \mathbb{0}_2 \end{pmatrix} \qquad \text{with} \quad \boldsymbol{X} = \begin{pmatrix} M_2 & g_2 v_u \\ g_2 v_d & \mu \end{pmatrix}. \tag{1.66}$$

The masses of the charginos are then the eigenvalues of the doubly degenerate 4×4 matrix $\boldsymbol{M}_{\tilde{\chi}^\pm}^\dagger \boldsymbol{M}_{\tilde{\chi}^\pm}$ and can be expressed in terms of M_2, μ and $\sin 2\beta$ [3].

Squarks and sleptons also mix with each other. As in principle any scalars with same electric charge, colour charge and R-parity can mix with each other, the mass eigenstates of the sleptons and squarks should a priori be obtained through diagonalization of three 6×6 mixing matrices (one for up-type squarks, one for down-type squarks and one for charged sleptons) and one 3×3 matrix (for sneutrinos). The assumption of flavour-blind soft SUSY breaking terms leads to most of the mixing angles being very small. As opposed to the first and second generation, the third generation sfermions have relatively large Yukawa couplings, therefore the superpartners of the left- and right-handed fermions mix to mass eigenstates $(\tilde{t}_1, \tilde{t}_2)$, $(\tilde{b}_1, \tilde{b}_2)$, $(\tilde{\tau}_1, \tilde{\tau}_2)$, again labeled in ascending mass order. The first and second generation sfermions, on the other hand, having very small Yukawa couplings, end up in nearly mass-degenerate, unmixed pairs.

The gluino, being the single color octet fermion of the unbroken $SU(3)_C$ gauge group, cannot mix with another fermion and thus is a mass eigenstate with mass $m_{\tilde{g}} = |M_3|$ at tree level [3, 48].

R-parity

The superpotential of the MSSM in principle allows additional gauge-invariant terms that are holomorphic in the chiral superfields but violate either lepton number (L) or baryon number (B). However, L- or B-violating have never been observed. Even worse, the L- and B-violating

[†] This makes the phase of μ in that convention a physical parameter that can no longer be rotated away through basis rotation.

terms would cause a finite lifetime of the proton by allowing for it to decay e.g. via $p \to e^+\pi^0$, a process that is heavily constrained to have a lifetime longer than 1.6×10^{34} years [61] as found by the Super-Kamiokande experiment.

In order to avoid these terms, a new symmetry called *R-parity* is introduced. R-parity is a multiplicatively conserved quantum number defined to be

$$P_R = (-1)^{3(B-L)+2s}, \tag{1.67}$$

where s is the spin of the particle. Given this definition, all SM particles and the Higgs bosons have even R-parity ($P_R = +1$) while all spartners have odd R-parity ($P_R = -1$). Assuming R-parity to be exactly conserved at each vertex in the MSSM leads to a number of interesting phenomenological consequences:

- Sparticles are always produced in pairs.
- Heavier sparticles decay into lighter ones.
- The number of sparticles at each vertex must be even.
- The lightest supersymmetric particle (LSP) must be stable as it cannot decay any further without violating R-parity.

The nature of the LSP can be further constrained by cosmological observations [62]. If it were electrically charged or coupled to the strong interaction, it would have dissipated its energy and mixed with ordinary matter in the galactic disks where it would have formed anomalous heavy isotopes. Upper limits on such supersymmetric relics [63] thus heavily favour an electrically neutral and weakly interacting LSP. This excludes in particular the gluino as an LSP. Another possible LSP, the sneutrino, is ruled out by LEP and direct searches. A gravitino LSP is especially attractive in gauge mediated theories.

Another option is a neutralino LSP. In large portions of the MSSM parameter space, a neutralino LSP produces a DM relic density that is compatible with the DM relic density measured by Planck [63, 44]. In the following, only R-parity conserving SUSY models with neutralino LSPs are considered.

1.2.6 The phenomenological MSSM

In addition to the 19 parameters of the SM, the MSSM adds a total of 105 additional parameters, too much to allow for a realistic exploration of the MSSM in a model-independent way. However, as already discussed in section 1.2.5, not all values of the 105 additional parameters lead to phenomenologically viable models. By requiring a set of phenomenological constraints, the 105 free parameters can be reduced to only 19 free parameters, spanning a model space called the phenomenological MSSM (pMSSM) [64, 65]. The free parameters in the pMSSM are listed in table 1.4.

The reduction of free parameters is obtained by applying the following constraints on the MSSM:

Table 1.4: Parameters of the pMSSM.

Parameter	Meaning
$\tan\beta$	ratio of the Higgs doublet VEVs
M_A	mass of the CP-odd Higgs boson
μ	Higgs-higgsino mass parameters
M_1, M_2, M_3	wino, bino and gluino mass parameters
$m_{\tilde{q}}$, $m_{\tilde{u}_R}$, $m_{\tilde{d}_R}$, $m_{\tilde{\ell}}$, $m_{\tilde{e}_R}$	first and second generation sfermion masses
$m_{\tilde{Q}}$, $m_{\tilde{t}_R}$, $m_{\tilde{b}_R}$, $m_{\tilde{L}}$, $m_{\tilde{\tau}_R}$	third generation sfermion masses
A_t, A_b, A_τ	third generation trilinear couplings

- No new source of CP violation, as discussed already in section 1.2.5, achieved by assuming all soft breaking parameters to be real.
- Minimal flavour violation, meaning that FCNC, heavily constrained by experiment, are not allowed and the flavour physics is governed by the CKM matrix.
- First and second sfermion generations are mass-degenerate[†].
- The trilinear couplings and Yukawa couplings are negligible for the first and second sfermion generations.

The pMSSM does not make any assumptions on the physics above the TeV scale, and therefore does not assume a specific SUSY breaking mechanism. With its 19 free parameters, and the typical complexity of a search for SUSY, the pMSSM is still computationally extremely challenging to probe. Using appropriate approximations, the computational complexity can be simplified enough for exhaustive scans and comparisons to experimental data to become possible.

1.2.7 Simplified models

In searches for BSM physics at the Large Hadron Collider, it is common to use simplified models [66–68] as a way of reducing the space of free parameters to a manageable level. Simplified models do not aim to represent complete supersymmetric models but are mostly defined by the empirical objects and kinematic variables use in the searches, typically allowing only a small number of sparticles to be involved in the decay chain (usually only two or three). Other sparticles are decoupled by setting their masses to be kinematically inaccessible at current collider experiments. The decay chains of the participating sparticles are determined by fixed branching ratios, often set to be 100%. Experimental bounds from non-observation of a given model are then usually presented in function of the physical masses of the sparticles involved in the decay chain. The model space spanned by the free parameters of the simplified model is typically called a *signal grid*, as each set of distinct mass parameter values, called *signal point*, occupies a single point in this space.

[†] This is motivated by e.g. Kaon mixing measurements and holds unless first and second generation squarks are significantly heavier than $\mathcal{O}(1\,\text{TeV})$.

Simplified models have the inherent advantage that they circumvent the issue of having to search for SUSY in a vast parameters space where many of the parameters only have small effects on observables. Their interpretation in terms of limits on individual SUSY production and decay topologies in function of sparticle masses is straightforward and very convenient. The hope is, that simplified models are a reasonable approximation of sizeable regions of parameter space of the more complete model they are embedded in [5]. The obvious downside is however, that the limits obtained in simplified models are not automatically a good approximation of the true underlying constraint on the respective model parameter when interpreted in more complete SUSY models. Often times, for example, the constraints set on sparticle masses in simplified models, significantly overestimate the true constraints obtained in more complex SUSY spectra, especially when the usual 100% branching fractions are assumed in the simplified models (see e.g. [69, 70]).

One way of circumventing these issues while sticking to the simplified model approach is to ensure that the limits obtained in different simplified models involving different production and decay mechanisms are combined into limits representing more complex SUSY spectra. In such an approach, the simplified model limits can be seen as building blocks for more complete and realistic SUSY models. Another possibility is to perform reinterpretations of SUSY searches—optimised for one ore more simplified models—in more complete SUSY model spaces, like e.g. the pMSSM. This can not only demonstrate the sensitivity of existing SUSY searches beyond simplified models, but also potentially identify blind spots and uncovered model regions. In addition, direct connections to DM searches as well as Higgs and flavour measurements can be explored this way. Some recent efforts going in this direction are provided in [69, 71, 72].

1.3 Search for electroweakinos

While both the ATLAS experiment [73] and CMS experiment [74] at the Large Hadron Collider at CERN set strong limits on the presence of gluinos and squarks at the TeV scale, the limits on electroweakinos are mostly still well below 1 TeV and thus offer ample space for SUSY to hide in. The reason why the limits on electroweakinos are still low is mostly due to the low cross-sections of electroweakino production, compared to those of squark and gluino production.

Apart from the electroweakino mass limits set by the current collider experiments, some additional limits from the LEP experiments are still relevant. Combining the results from all four LEP experiments leads to a general lower chargino mass limits of 103.5 GeV, except for corners of the phase space with low sneutrino mass [75]. For small mass splittings between the $\tilde{\chi}_1^{\pm}$ and the $\tilde{\chi}_1^0$, the lower limit is a little weaker with dedicated searches excluding charginos with $m(\tilde{\chi}_1^{\pm}) < 91.9\,\text{GeV}$ [75]. For the neutralino, a general lower limit on the lightest neutralino mass comes from limits on the invisible width of the Z boson, excluding $m(\tilde{\chi}_2^0) < 45.5\,\text{GeV}^{\dagger}$ [5].

1.3.1 Production of electroweakinos at the Large Hadron Collider

If gluinos and squarks are too heavy to be within reach of the Large Hadron Collider, the direct production of electroweakinos might be the dominant production mode of SUSY. At hadron

† Depending on the coupling between the Z boson and the lightest neutralino.

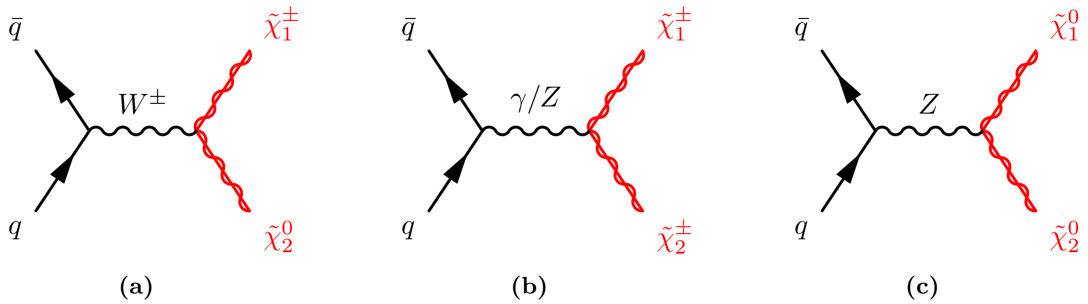

Figure 1.7: Dominant Feynman diagrams for direct production of electroweakino pairs at the Large Hadron Collider.

colliders, electroweakinos can be pair-produced directly via electroweak processes. The direct production of electroweakino pairs dominantly happens through electroweak gauge bosons from s-channel $q\bar{q}$ annihilation, as shown in fig. 1.7. Contributions from t-channels via squark exchange are typically of less importance [3].

1.3.2 Models used within this work

The main model considered in the SUSY search presented in this work and pictured in fig. 1.8 is a simplified model for direct production of a $\tilde{\chi}_1^{\pm}\tilde{\chi}_2^0$ pair where the lightest chargino decays via $\tilde{\chi}_1^{\pm} \to W\tilde{\chi}_1^0$ and the next-to-lightest neutralino decays via $\tilde{\chi}_2^0 \to W\tilde{\chi}_1^0$, each with 100% branching ratio. In this model, in the following called the *Wh model*, the lightest chargino $\tilde{\chi}_1^{\pm}$ and the next-to-lightest neutralino $\tilde{\chi}_2^0$ are considered to be mass-degenerate and wino-like, while the lightest neutralino $\tilde{\chi}_1^0$ is a bino-like LSP, hence $|M_1| < |M_2| \ll |\mu|$. The masses of $\tilde{\chi}_1^{\pm}/\tilde{\chi}_2^0$ and $\tilde{\chi}_1^0$ are free parameters and are systematically varied, creating a two-dimensional signal grid to be scanned and compared to data. The Higgs boson mass is set to 125 GeV in accordance with the measured value [76, 77] and its branching ratios are the ones from the SM. The search further targets a W boson which decays into an electron or muon (and a corresponding neutrino) and a Higgs boson decaying into a pair of b-quarks. The branching ratio of $h \to b\bar{b}$ is taken to be 58.3% as expected for the SM Higgs boson. The final state of this simplified model thus includes exactly one light lepton (electron or muon) from the $W^{\pm}$ decay, two b-jets from the Higgs boson decay, as well as missing transverse momentum from the LSPs and neutrino escaping the detector. introduced in section

In addition to the simplified model targeted by the SUSY search presented in this work, an additional class of models is considered in the second part of this work. These models are sampled directly from the pMSSM and are used to reinterpret the SUSY search in the pMSSM. In accordance with the simplified model in fig. 1.8, the pMSSM models are sampled with a focus on electroweakinos, i.e. all electroweak parameters are set to be lighter than 2 TeV while first and second generation squarks are decoupled and set to have mass parameters of 10 TeV. Sleptons are also set to be decoupled with mass parameters fixed at 10 TeV. In order to yield a better rate of surviving models during the sampling without affecting the decays of the electroweakinos too much, third generation squark and gluino mass parameters are varied between 2–5 TeV and 1–5 TeV, respectively. No assumptions are made on the bino, wino or Reference, why?

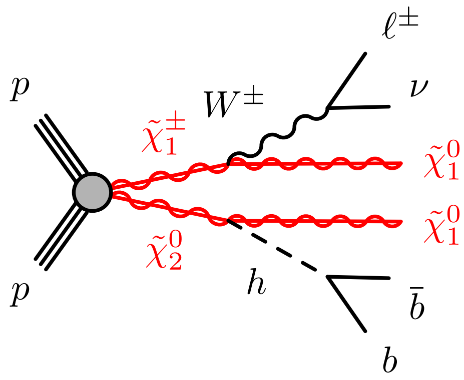

Figure 1.8: Diagram for the simplified model used in this work.

higgsino nature of either charginos or neutralinos. More details on the sampling of the pMSSM models are given in.

reference to sampling

Chapter 2

Experiment

One of Europe's first joint ventures in science [78], CERN (Conseil Européen pour la Recherche Nucléaire) is the largest physics research facility in the world, bringing together more than 12,200 people from of 110 nationalities to work together and push the frontiers of science and technology. Located at the Franco-Swiss border near Geneva, CERN was founded in 1954 and nowadays counts 23 member states [78]. CERN's main research area is particle physics, hence why the organization operates a full complex of particle accelerators and detectors.

This chapter introduces the Large Hadron Collider (LHC), CERN's main particle accelerator, as well as the ATLAS experiment, in which the Supersymmetry (SUSY) search presented in this work is embedded in.

2.1 The Large Hadron Collider

The LHC [79] is the largest particle accelerator situated at CERN. It is installed in a tunnel with 26.7 km circumference, that was originally constructed from 1984 to 1989 for the Large Electron Positron (LEP) accelerator. The tunnel is situated on the Franco-Swiss border and wedged between the Jura mountains and lake Léman. It lies between 45 m (in the limestone of the Juar) and 170 m (in molasse rock) below the surface, resulting in a tilt of 1.4% towards the lake. While proton-proton (pp) collisions are the main operating mode of the LHC, its design also allows it to accelerate and collide heavy ions like lead and xenon. Since data from pp collisions is used in this work, the following sections will mainly focus on this operating mode. As a particle-particle collider, the LHC obviously consists of two rings with counter-rotating beams, as opposed to particle-antiparticle colliders that only need a single ring. With an inner diameter of only 3.7 m, the tunnel however simply too narrow to fit two separate proton rings. Instead the LHC is built in a twin bore design†, housing two sets of coils and beam channels in a single magnetic and mechanical structure and cryostat [79]. While saving costs, this design has the disadvantage of both beams being magnetically coupled, thereby reducing flexibility of the machine.

Before being injected into the LHC, protons are pre-accelerated by an injection chain built from multiple existing machines in CERN's accelerator complex, pictured in fig. 2.1. The injection

† Originally proposed by John Blewett at BNL for cost-saving measures of the Colliding Beam Accelerator [79].

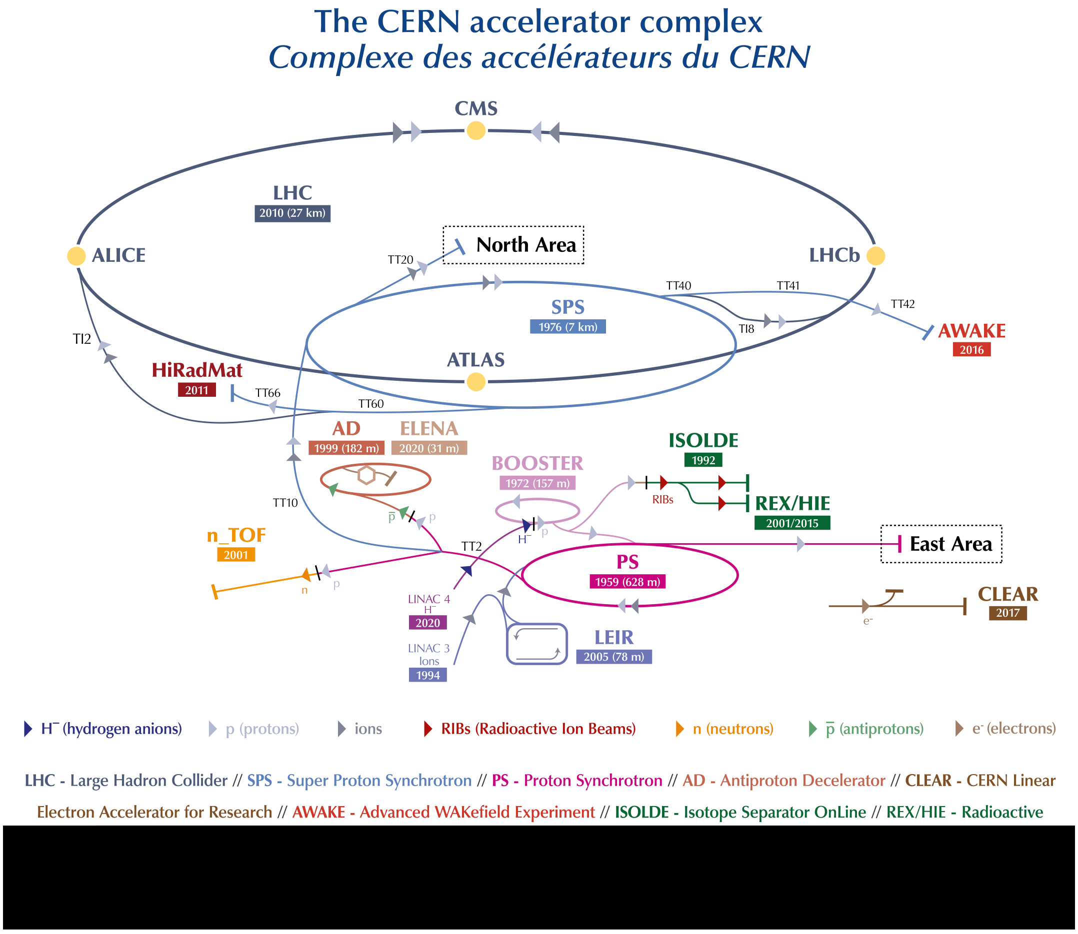

Figure 2.1: CERN accelerator complex as of 2018 [81].

chain consists of predecessor accelerators that have been upgraded in order to be able to handle the high luminosity and high energy requirements of the LHC. The protons for the LHC stem from a duoplasmatron source [80], stripping electrons from hydrogen atoms through electric discharges between a hot anode and cathode. The 90 keV protons are then accelerated by a Radio frequency (RF) quadrupole to 750 keV before being injected into Linac2[†], a linear accelerator producing a beam of 50 MeV protons through the use of RF cavities. The protons then enter a set of circular accelerators, the Proton Synchrotron Booster (PSB), the Proton Synchrotron (PS) and the Super Proton Synchrotron (SPS), creating a stepwise acceleration up to an energy of 450 GeV, which is the injection energy of the LHC. The LHC finally accelerates the protons up to nominal beam energy before colliding them.

The LHC is composed of eight straight sections and eight arcs. The eight straight sections each serve as interaction points (*Point*), either for particle detectors, or for machine hardware of the collider itself. The Points are labelled clockwise, with IP 1 being closest to the CERN Meyrin site. Four of the eight Points house the main particle physics experiments at the LHC, called

[†] Originally built to replace Linac 1 in order to produce higher energetic proton beams, Linac 2 has been replaced by Linac 4 in 2020.

ATLAS, CMS, ALICE and LHCb, covering a wide range of fundamental research. The two general purpose particle detectors ATLAS [82] and CMS [83] are installed at Point 1 and Point 5, respectively. Both ATLAS and CMS are designed to perform high precision SM measurements including Higgs measurements as well as searches for BSM physics. Being very similar in terms of targeted phase space, ATLAS and CMS can be used to cross-check results of each other. ALICE [84] is situated at Point 2 and specializes on heavy ion physics, studying the physics of quark-gluon plasma at high energy densities. Built in Point 8, LHCb [85] targets B-physics and performs measurements of CP-violation. Apart from the four main experiments, three smaller experiments exist at the LHC: TOTEM, MoEDAL and LHCf. While TOTEM [86] and LHCf [87] study forwards physics close to CMS and ATLAS, respectively, MoEDAL [88] searches for magnetic monopoles.

The remaining four Points house accelerator equipment needed for operation of the LHC. Most of the collimation system is placed at Point 3 and Point 7, performing beam cleaning and machine protection through a series of beam intercepting devices, ensuring that no stray particles from experimental debris or beam halo can reach and damage other machine components. The acceleration of the beam itself is performed at Point 4 with two RF systems, one for each LHC beam. The RF cavities operate at 400 MHz and provide 8 MV during injection and 16 MV during coast [79]. Due to the RF acceleration, the accelerated protons are grouped in packages called *bunches*, each containing roughly 10^{11} protons, with a bunch spacing of 25 ns [79]. Each beam contains a total of 2808 [79] bunches as design value. The remaining Point 6 houses the beam dumping system, allowing to horizontally deflect and fan out both beams into dump absorbers using fast-paced *kicker* magnets. The two nitrogen-cooled dump absorbers each consist of a graphite core contained in a steel cylinder, surrounded by 750 t of concrete and iron shielding [89]. Insertion of the beams from the SPS into the LHC happens at Points 2 and 8, close to the ALICE and LHCb experiments.

The eight arcs of the LHC are filled with dipole magnets built from superconducting NbTi Rutherford cables. The electromagnets are responsible for keeping the accelerated particles on their circular trajectory and are the limiting factor of the maximal centre-of-mass energy $\sqrt{s}$ of the LHC. In order to achieve the design energy of $\sqrt{s} = 14\,\text{TeV}$ [89], the magnets have to create a field strength of 8.3 T [79]. In order to sustain the electric currents needed for such high field strengths, the magnets need to be cooled down to 1.9 K [79] using superfluid helium and operated in superconducting state. In addition to the dipole magnets, the arcs contain quadrupole magnets used to shape and focus the beams, as well as multipole magnets correcting and optimizing the beam trajectory. Quadrupole magnets are also used to reduce the beam size before and after the interaction points.

2.1.1 Pile-up

Due to the high number of protons in each bunch, several pp collisions occur at each bunch crossing. This leads to a phenomenon called *pile-up*, where the recorded events not only contain information from the hard-scattering process of interest, but also remnants from additional, often low-energy, pp collisions. During the Run 2 data-taking period, the mean number of inelastic pp collisions per bunch crossing, μ, has varied from roughly 10 to 70, with the majority of bunch crossings having a value of μ around 30. Figure 2.2(a) shows the mean number of interactions per bunch crossing during the Run 2 data-taking period, weighted by luminosity.

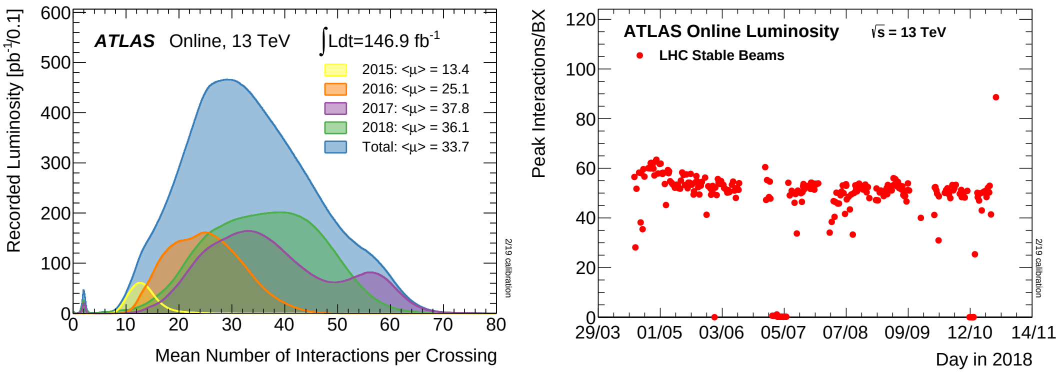

(a) Luminosity-weighted mean number of interactions per bunch crossing during Run 2 data-taking.

(b) Peak mean number of interactions per bunch crossing for each fill during 2018.

Figure 2.2: Number of interactions per bunch crossing recorded by the ATLAS detector [90]

The peak number of interactions per bunch crossing μ_{peak} per fill has been consistently around 50 during the 2018 data-taking (cf. fig. 2.2(b)).

Experimentally, pile-up can be divided into five major components [91]:

- *In-time* pile-up: multiple interactions during a single bunch crossing, of which not all will be interesting, as often with relatively low energy. If they can be resolved, the main hard-scattering event can still be isolated and studied.
- *Out-of-time* pile-up: additional collisions occurring in bunch crossings before or after the main event of interest. This happens either due to read-out electronic integrating over longer time frames than the 25 ns bunch spacing, or detector components being sensitive to several bunch crossings.
- *Cavern background*: gas of thermal neutrons and photons that typically fill the experimental caverns during a run of the LHC and tend to cause random hits in detector components.
- *Beam halo events*: protons scraping an up-stream collimator, typically resulting in muons travelling parallel to the beam pip
- *Beam gas events*: collision events that originate from interactions between proton bunches and residual gas inside the beam pipe.

While the effects of cavern background can be mitigated through special pieces of shielding, beam halo and beam gas events leave signatures that can be recognized and removed. Signals from in-time and out-of-time pile-up create irreducible overlap with the events of interest, significantly impacting analyses, and thus need to be simulated [91].

2.1.2 Luminosity and data-taking

Apart from the beam energy, the most important quantity for a collider is the instantaneous luminosity L. For a synchrotron with Gaussian beam distribution, the instantaneous luminosity

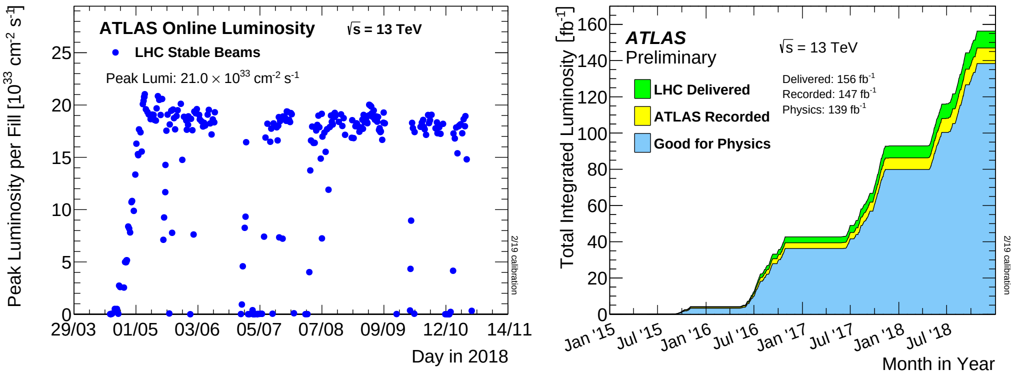

(a) (b)

Figure 2.3: Instantaneous and cumulative luminosities in Run 2. Figure (a) shows the peak instantaneous luminosity delivered to ATLAS during *pp* collision data taking in 2018 as a function of time. Figure (b) shows the cumulative luminosity delivered to ATLAS (green), recorded by ATLAS (yellow) and deemed good for physics analysis (blue) during the entirety of Run 2 [90].

can be written as

$$L = \frac{N_b^2 n_b f_{\text{rev}}}{4\pi\sigma_x\sigma_y} F, \tag{2.1}$$

where n_b is the number of bunches, N_b the number of protons per bunch, f_{rev} the revolution frequency and σ_x and σ_y the transverse beam sizes. The parameters F is a geometrical correction factor accounting for the reduction in instantaneous luminosity due to the beams crossing at a certain crossing angle. While the design instantaneous luminosity of the LHC at the high-luminosity experiments ATLAS and CMS is $L = 10^{34}\,\text{cm}^{-2}\,\text{s}^{-1}$ [79], the 2017 and 2018 data-taking periods saw a peak luminosity twice as high [92].

The instantaneous luminosity is related to the total number of events N through the cross section σ of the events in question

$$N = \sigma L_{\text{int}} = \sigma \int L\,\text{d}t, \tag{2.2}$$

with L_{int} the total integrated luminosity, a measure for the total amount of collision data produced.

A precise knowledge of the integrated luminosity corresponding to a given dataset is crucial for both SM measurements as well as searches for Beyond the Standard Model (BSM) physics. Searches for SUSY like the one presented in this work rely on precise measurements of the integrated luminosity in order to be able to estimate the contribution from SM background processes. The luminosity measurement for the Run 2 dataset used within this work is described in detail in [93, 94] and relies on a measurement of the bunch luminosity, i.e. the luminosity produced by a single pair of colliding bunches

$$L_b = \frac{\mu f_{\text{rev}}}{\sigma_{\text{inel}}} = \frac{\mu_{\text{vis}} f_{\text{rev}}}{\sigma_{\text{vis}}}, \tag{2.3}$$

with μ the pile-up parameter, σ_{inel} the cross section of inelastic pp collisions, $\mu_{\text{vis}} = \epsilon\mu$ is the fraction ϵ of the pile-up parameter μ visible to the detector and $\sigma_{\text{vis}} = \epsilon\sigma_{\text{inel}}$ the visible inelastic cross section. If σ_{vis} is known, the currently recorded luminosity can be determined by measuring μ_{vis}. At the ATLAS experiment, the observed number of inelastic interactions per bunch crossing μvis is measured using dedicated detectors, as for example LUCID-2 [95], a forward Cherenkov-detector using the quartz windows from photomultipliers as Cherenkov medium. In order to use μ_{vis} as luminosity monitor, the respective detectors need to be calibrated through a measurement of the visible inelastic cross section σ_{vis}. This can be done using van der Meer (vdM) scans [96, 97], in which the transverse distribution of protons in the bunches is inferred by measuring the relative interaction rates as a function of the transverse beam separation†. The algorithms used to determine the σ_{vis} calibration are described in [93, 94] and the luminosity during the vdM runs can be determined using eq. (2.1). At the LHC, vdM scans are typically performed in special low-μ runs with well-known machine parameters in order to minimise uncertainties [93]. During high-μ physics runs, the luminosity measurement is then an extrapolation from the vdM runs.

The LHC entered operation in 2008, with first beams in September and first collisions by the end of November that same year [98]. Its operation is in general structured into so-called *Runs*, that are spanned by multiple years of data-taking. Run 1 spanned from 2009 to 2013 and delivered roughly 28.5 fb^{-1} of pp collision data to ATLAS, taken at centre-of-mass energies of 7 TeV and 8 TeV [99, 100, 94]. Run 2 lasted from 2015 to 2018 and saw a centre-of-mass energy increase to 13 TeV, delivering approximately 156 fb^{-1} of pp collision data to ATLAS [93]. Run 3 of pp collision data taking with two times design peak luminosity is currently planned to start its physics program in 2022 and last until end of 2024 [101]. Current plans foresee Run 3 to deliver about 150 fb^{-1} of pp collision data with centre-of-mass energies of 13 TeV and 14 TeV. After Run 3, the LHC will be upgraded to the High Luminosity LHC, significantly increasing the peak instantaneous luminosity and delivering up to 3000 fb^{-1} of pp collision data from 2027 until 2040 [101, 102].

This work uses pp collision data taken by ATLAS during Run 2 of the LHC. Of the 156 fb^{-1} delivered to ATLAS, 147 fb^{-1} were recorded, and 139 fb^{-1} were deemed to be good for physics analysis. Figure 2.3 shows the cumulative luminosity delivered to ATLAS during Run 2. Uncertainties on the measurement total recorded luminosity stem from the measurements of μ_{vis} and σ_{vis}, but are dominated by the uncertainties on σ_{vis} as vdM scans can only be done during special runs, while the general conditions during high-μ conditions change continuously. For the full Run 2 dataset, the uncertainties accumulate to $\pm 1.7\%$ [93].

2.2 ATLAS Experiment

The ATLAS experiment is one of two general-purpose detectors at the LHC. Located at Point 1 in a cavern 100 m below the surface, it is approximately 44 m long and 25 m high [82]. The design of the ATLAS experiment is driven by the aim to allow for a diverse research program, including SM precision measurements, Higgs physics and searches for BSM physics, whilst at the same time taking into account the unique and challenging conditions set by the LHC. The various detector technologies used are designed to withstand the high-radiation environment

† Often called *beam sweeping*.

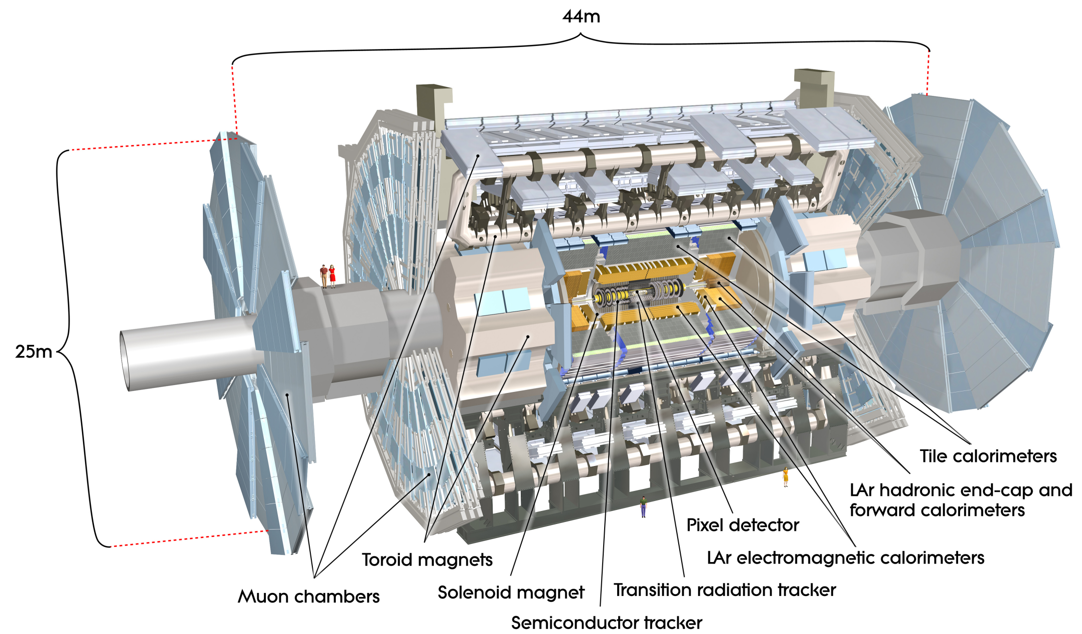

Figure 2.4: Computer generated picture of the ATLAS detector, giving an overview on the various subsystems [103].

of the LHC, while allowing particle measurements with high spatial and temporal granularity. The general structure of ATLAS is depicted in fig. 2.4, and consists of a central part, called *barrel*, that has a cylindrical shape around the beam pipe, and two discs, called *end-caps*, that close off the barrel on each side. This makes the ATLAS detector forward-backward symmetric and covering nearly the full solid angle of 4π, which is needed in order to measure momentum imbalances caused by particles that only interact weakly with the detector material.

The interface between the ATLAS experiment and the LHC is the beam pipe. In order to be maximally transparent to the particles created in the collisions, but also be able to withstand the forces from the vacuum, the beam pipe is made out of Beryllium close to the Interaction Point (IP), and stainless-steel further away from the IP [1].

The following sections introduce the working principles of the different detector components used in ATLAS, starting with the innermost component closest to the IP, the inner detector, followed by the calorimeters in the middle and finally the muon spectrometers on the outside. If not otherwise stated, details on the detector components are extracted from [82].

2.2.1 Coordinate system

In order to properly describe collision events in the ATLAS detector, a suitable detector system is needed. The right-handed coordinate system [104] used in ATLAS has its origin at the nominal IP in the centre of the detector. The positive x-axis points towards the centre of the LHC ring, the positive y-axis points upwards to the surface, and the beam pipe is used to define the z-axis. In the x–y plane, called the transverse plane, the azimuthal angle ϕ is the angle around the beam axis, and the polar angle θ is measured from the beam axis. The rapidity [5] is defined as

$$y = \frac{1}{2}\ln\left(\frac{E+p_z}{E-p_z}\right) = \tanh\frac{p_z}{E}^{-1}, \tag{2.4}$$

with E the energy of an object and p_z its momentum in z-direction. As opposed to the polar angle θ, differences in the rapidity are invariant under Lorentz boosts in z-direction.

The pseudorapidity [5] is the high-energy limit ($p \gg m$) of the rapidity, and defined as

$$\eta = -\ln\tan\frac{\theta}{2}, \tag{2.5}$$

with $\cos\theta = p_z/p$. Pseudorapidity and rapidity are approximately equal in the limit where $p \gg m$ and $\theta \gg \frac{1}{\gamma}$. Compared to the rapidity, the pseudorapidity has the advantage of not depending on the energy and momentum calibration of the detected objects. Additionally, it gives a direct correspondence to the polar angle θ through the relation $\tanh\eta = \cos\theta$. Objects travelling along the beam axis have a pseudorapidity of $\eta = \inf$ and objects travelling upwards along the y-axis have $\eta = 0$.

The distance between two objects in the ATLAS detector is given by

$$\Delta R = \sqrt{(\Delta\eta)^2 + (\Delta\phi)^2}. \tag{2.6}$$

The longitudinal momentum of the partons composing the colliding hadrons is only known by means of the Parton Distribution Functions (PDFs), giving the probabilities of the partons to have a certain energy in the direction of the beam. Thus, the total longitudinal energy in each collision is not exactly known, impeding the use of physics quantities in the z-direction. In the x–y plane, however, momentum conservation can be applied, which is why mainly transverse physics quantities are used, indicated by a subscript 'T', e.g. E_T or p_T.

2.2.2 Magnet system

In order to perform precise momentum measurements of particles, ATLAS uses a system of magnets, whose magnetic fields force charged particles on curved tracks due to the Lorentz force. Using precise measurements of the tracks taken in the inner detector and the muon spectrometers, the curvature of the tracks can be determined, allowing an inference of the charge-to-momentum ratio q/p of charged particles. ATLAS employs a set of four superconducting magnets, one central solenoid, and three toroids, all operating at a nominal temperature of 4.5 K, achieved through a cryogenic system using liquid helium [82].

The solenoid is aligned on the beam axis and provides a 2 T magnetic field for the inner detector [82]. As it is located in front of the calorimeters (as seen from the IP), it is specially designed to have minimal material thickness in order to avoid influencing the subsequent energy measurements. The solenoid consists of single-layer coils made out of a Nb/Ti conductor and additional aluminum for stability. It operates at a nominal current of 7.73 kA and uses the hadronic calorimeter as return yoke [82].

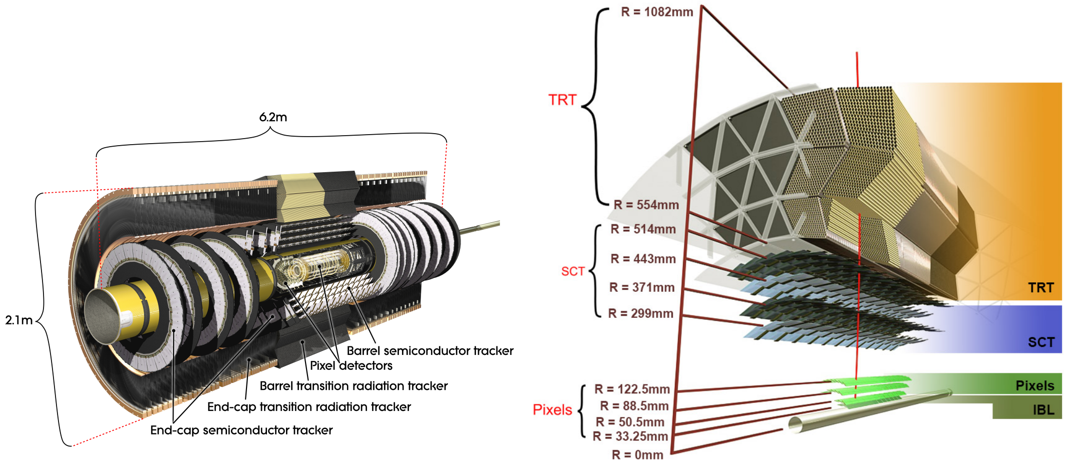

Figure 2.5: Schematic drawing of the ID and its subdetectors. Images adapted from [105, 106].

The toroid magnets consist of a barrel toroid and two end-cap toroids, producing a magnetic field of 0.5 T and 1 T for the muon spectrometers in the barrel and end-caps, respectively[†] [82]. Both barrel and end-cap toroids are made out off Nb/Ti/Cu conductor with aluminum stabilisation, wound into double pancake-shaped coils. The barrel toroid coils are enclosed in eight stainless-steel vacuum vessels in a racetrack-shaped configuration and arranged around the barrel calorimeters with an azimuthal symmetry. In order to withstand the Lorentz forces, the end-cap toroid coils are assembled in eight square units, and bolted and glued together with eight wedges, forming rigid structures. Both end-cap and barrel toroids operate at a nominal current of 20.5 kA [82].

2.2.3 Inner detector

Embedded in the magnetic field of the solenoid, the Inner Detector (ID) measures tracks of charged particles, allowing a determination of their momentum, while also providing crucial information for vertex reconstruction. As the ID is the detector closest to the beam pipe, its components need to be able to withstand the extreme high-radiation environment close to the IP. The ID consists of three subdetectors and uses two different working principles: semiconductor and gaseous detectors. In semiconductor-based tracking detectors, charged particles passing through the detector create a trail of electron-hole pairs that subsequently drift through the semiconductor material and cause electric signals. In gaseous detectors, traversing particles create electron-ion pairs also drift towards metal electrodes and induce electric signals.

Closest to the ID lies the pixel detector, followed by the Silicon Microstip Tracker (SCT), both of which are made of semiconductors. The SCT is surrounded by the Transition Radiation Tracker (TRT), a gaseous detector. In total, the ID provides tracking and momentum information within $|\eta| < 2.5$ and down to transverse momenta of nominally 0.5 GeV. A schematic illustration of the ID and its subdetectors is shown in fig. 2.5.

[†] The magnetic field in of the toroid magnets is designed to be higher in the end-caps in order to ensure enough bending power necessary for precise momentum measurements.

Pixel detector

In the high-rate environment directly adjacent to the beam pipe, the only detector technology able to operate and deliver high-precision tracking information are semiconductor detectors segmented into pixels. As opposed to strip detectors, the reduced size of silicon pixel detectors and thus significantly reduced hit rate per readout channel allows pixel detectors to still be operational in the harsh environment close to the IP. In ATLAS, pixels are hybrids of sensors and readout electronics, and were originally arranged in three layers in the barrel and the end-caps with a typical pixel of $50\,\mu\mathrm{m} \times 400\,\mu\mathrm{m}$, covering pseudorapidities up to $|\eta| < 2.5$. In order to increase robustness and performance in the high-luminosity environment, a new innermost layer, called the Insertable B-Layer (IBL), was installed together with a new, smaller radius beam pipe between Run 1 and Run 2 [107, 108]. The IBL uses smaller pixels with a size of $50\,\mu\mathrm{m} \times 250\,\mu\mathrm{m}$ and improves the tracking precision as well as vertex identification performance [108]. It also improves the performance of identifying jets originating from b-quarks (called b-tagging). The pixel detector [109]. The tracking precision obtained by the pixel detector is $10\,\mu\mathrm{m}$ in $(R - \phi)$ and $115\,\mu\mathrm{m}$ in (z) for the barrel and (R) for the end-caps.

Silicon microstrip detector

The pixel detector is surrounded by the SCT, consisting of four layers in the barrel and nine disks in the end-caps. In order to provide two-dimensional tracking information, strips are arranged in double-layers with a small crossing angle of 40 mrad and a mean pitch of $80\,\mu\mathrm{m}$ [82]. A charged particle traversing the SCT through the barrel thus creates four space point measurements. In the barrel, one set of strips in each of the four double-layers is oriented in beam direction, thereby measuring $R - \phi$, and in the end-caps, one set of strips in each layer is oriented in radial direction. The SCT has roughly 6.3 million readout channels and provides tracking information up to $|\eta| < 2.5$ [82]. It achieves a precision of $17\,\mu\mathrm{m}$ in $(R - \phi)$ and $580\,\mu\mathrm{m}$ in (z) for the barrel and (R) for the end-caps [82].

Transition radiation tracker

The last and also largest of the three subdetectors of the ID is the TRT, a gaseous detector made of multiple layers of 4 mm diameter drift tubes, surrounding the pixel detector and the SCT. The drift tubes consist of an aluminum cathode coated on a polyimide layer reinforced by carbon fibers and use a gold-plated tungsten wire as anode. The tubes are filled with a Xe-based gas mixture, providing an electric permittivity different from the surrounding material, causing transition radiation when traversed by ultrarelativistic particles. While the 144 cm long tubes in the barrel region are aligned parallel to the beam pipe, the 37 cm long tubes in the end-caps are aligned in radial direction, providing coverage up to $|\eta| < 2.0$ and an intrinsic accuracy of $130\,\mu\mathrm{m}$ in $R - \phi$ [82]. The low accuracy compared to the pixel detector and the SCT is compensated by the large amount of hits (typically 36 per track) and the longer measured track length. As the amount of transition radiation given off by a particle, is proportional to its Lorentz factor γ [5], the TRT is also used to improve electron identification [**?**]. For the same momentum, electrons will have a higher Lorentz factor than the heavier charged pions, and consequently give off more transition radiation.

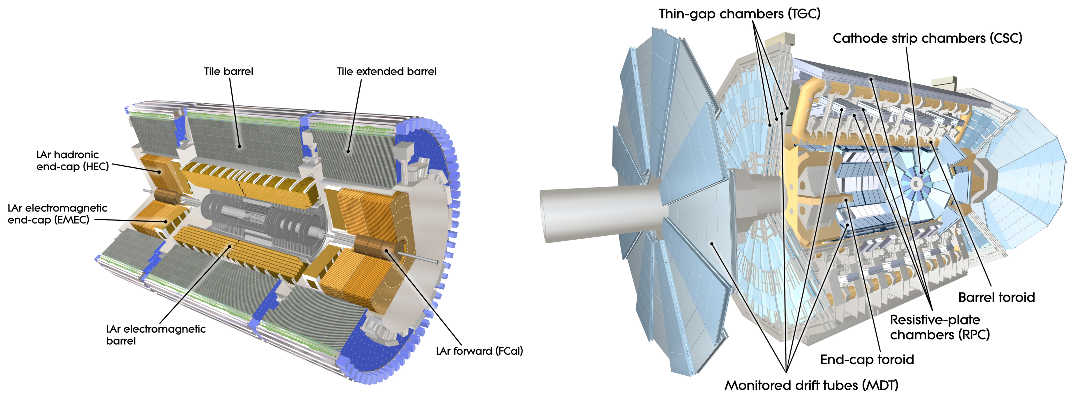

(a) Calorimeter systems **(b)** Muon spectrometer

Figure 2.6: Schematic drawing of the calorimeter systems and the muon spectrometer in ATLAS. Images adapted from [110, 111].

2.2.4 Calorimeters

The primary goal of calorimeters is to measure the energies of incoming particles by completely absorbing them. As the energies of neutral particles can not be measured by other means, calorimeters are especially important for jet energy measurements (which contain neutral hadrons) [1]. Since particles like photons and electrons interact mostly electromagnetically, while hadrons predominantly interact through the strong interaction, two different calorimeter types are needed in ATLAS. For values in η matching the ID, the electromagnetic calorimeter uses a finer granularity designed for precision measurements of electrons and photons. The subsequent hadronic calorimeter uses a coarser granularity sufficient for the requirements of jet reconstruction and missing transverse moment measurements. With a coverage up to $|\eta| < 4.9$, the calorimeter system in ATLAS provides the near hermetic energy measurements needed for the inference of missing transverse momentum created by neutrinos and other weakly interacting neutral particles [82].

Both calorimeters are sampling calorimeters, consisting of alternating layers of active and absorbing material. The absorbing material interacts with the incoming particles, causing them to deposit their energy by creating cascades or *showers* of secondary particles. The active layers are then used to record the shape and intensity of the produced showers. This alternating structure results in reduced material costs but also reduced energy resolution as only part of the particle's energy is sampled. Due to the typically longer cascades in hadronic interactions compared to electromagnetic interactions, and in order to minimise punch-through into the muon system, the hadronic calorimeter requires a greater material depth than the electromagnetic one. The calorimeter systems in ATLAS are schematically illustrated in fig. 2.6(a).

Electromagnetic calorimeter

The Electromagnetic (EM) calorimeter has an accordion-shaped structure and uses liquid argon (LAr) as active material and lead as absorber, providing full ϕ symmetry without azimuthal cracks. It is divided into a barrel part and two end-caps, covering $|\eta| < 1.475$ and

$1.375 < |\eta| < 3.2$, respectively, and arranged in a way to provide uniform performance and resolution as a function of ϕ. The barrel EM calorimeter consists of two identical half-barrels with a small gap of 4 cm at $z = 0$. In the end-caps, the EM calorimeter consists of two coaxial wheels, covering the region $1.375 < |\eta| < 2.5$ and $2.5 < |\eta| < 3.2$, respectively. Calorimeter cells in the EM calorimeter are segmented into multiple layers with fine granularity in first layers in the η region matching the ID, and coarser granularity in the outer layers and for $2.5 < |\eta| < 3.2$. In order to offer good containment of electromagnetic showers, the EM calorimeter has a depth of at least 22 (24) radiation lengths in the barrel (end-caps). A single instrumented LAr layer serves as presampler in the region with $|\eta| < 1.8$, allowing measurements of the energy losses upstream of the EM calorimeter, e.g. in the cryostats [82]. The design energy resolution of the EM calorimeter is $\sigma_E/E = 10\%/\sqrt{E} \oplus 0.7\%$ [82].

Hadronic calorimeter

Placed directly outside the envelope of the EM calorimeter is the hadronic tile calorimeter. It uses steel plates as absorber and polystyrene-based scintillating tiles as active material, and is subdivided into one central barrel and two extended barrels. Each barrel is segmented in three layers in depth with a total thickness of 7.4 interaction lengths. The tiles are oriented radially and perpendicular to the beam pipe and grouped in 64 tile modules per barrel, resulting in a near hermetic azimuthal coverage. Wavelength shifting fibres are used to shift the ultraviolet light produced in the scintillator to visible light and guide it into photomultipliers located at the radially far end of each module. The tile calorimeter covers a region with $|\eta| < 1.7$ and has a granularity of $\Delta\eta \times \Delta\phi = 0.1 \times 0.1$ except for the outermost layer which has a slightly coarser granularity in η. The design energy resolution of the tile calorimeter is $\sigma_E/E = 56.4\%/\sqrt{E} \oplus 5.5\%$ [82].

Hadronic calorimetry in the end-caps is provided by two independent calorimeter wheels per end-cap, situated directly behind the Electromagnetic end-cap calorimeter (EMEC). Similar to the EMEC, the Hadronic end-cap calorimeter (HEC) also uses LAr calorimeter as active material, allowing both calorimeter systems to share a single cryostat per end-cap. Instead of lead, the HEC however uses copper as absorber, which not only drastically reduces the mass of a calorimeter with a given interaction length, but also improves the linearity of low-energy hadronic signals [112]. Each of the four wheels of the HEC is comprised of 32 wedge-shaped modules, divided into two layers in depth. The HEC provides coverage in the region with $1.5 < |\eta| < 3.2$, slightly overlapping with the tile calorimeter and thus reducing the drop in material density in the transition region. While the granularity in the precision region with $1.5 < |\eta| < 2.5$ is the same as for the tile calorimeter, more forward regions with large $|\eta|$ have a granularity of $\Delta\eta \times \Delta\phi = 0.2 \times 0.2$ [82]. The design resolution of the HEC is $\sigma_E/E = 70.6\%/\sqrt{E} \oplus 5.8\%$ [82].

The forward region with $3.1 < |\eta| < 4.9$ is covered by the LAr Forward Calorimeter (FCal), which is integrated into the end-cap cryostats. This hermetic design not only minimises energy losses in cracks between the calorimeter systems, but also reduces the amount of background reaching the muon system in the outer shell of the ATLAS experiment. In order to limit the amount of neutrons reflected into the ID, the FCal is recessed by about 1.2 m with respect to the EM calorimeter, motivating a high-density design due to space constraints. The FCal in each end-cap consists of three layers with a total depth of 10 interaction lengths. While the first layer uses copper as absorber and is optimised for electromagnetic measurements, the remaining two layers are made of tungsten and cover hadronic interactions. The metals comprising each layer are arranged in a matrix structure with electrodes consisting of rods and tubes parallel to the beam pipe filling out regular channels. The small gaps (0.25 mm in the first layer) between the rods and tubes of the electrodes are filled with LAr as active material.

2.2.5 Muon spectrometer

Muons, being minimum ionising particles, are the only charged particles that consistently pass through the entire detector including the calorimeter system. Providing one of the cleanest signatures for BSM physics [1], muonic final states are measured with a dedicated detector system on the outermost layer of the ATLAS experiment. Embedded in the magnetic field of the toroid magnets, the Muon Spectrometer (MS) consists of three concentric cylindrical layers in the barrel region, and three wheels in each end-cap, and provides momentum measurements up to $|\eta| < 2.7$ [82]. It is designed to deliver a transverse momentum resolution of 10% for 1 TeV tracks and be able to measure muon momenta down to roughly 3 GeV.

The MS uses two high-precision gaseous detector chamber types, Monitoring Drift Tubes (MDTs) chambers and Cathode Strip Chambers (CSCs). As both the MDTs and CSCs are drift chambers relying on charges drifting to an anode or cathode, the maximum response times of 700 ns and 50 ns, respectively, are slow compared to the bunch-spacing of 25 ns. ATLAS therefore uses Resistive Plate Chambers (RPCs) in the barrel and Thin Gap Chambers (TGCs) in the end-caps as triggers in order to associate measurements to the right bunch-crossing.

Monitored drift tubes

The MDTs chambers are the main subcomponent providing precision measurements of the muon tracks up to $|\eta| < 2.7$, except in the innermost end-cap layer where their coverage only extends to $|\eta| < 2.0$. The MDTs are made of 3–4 layers of ~ 30 mm diameter drift tubes operated with Ar/CO_2 gas† pressurised to 3 bar. Charged particles traversing the drift tubes ionise the gas, creating electrons that drift towards a central tungsten-rhenium anode wire with a diameter of 50 µm. Following the symmetry of the barrel toroid magnet, the MDTs chambers are arranged as octets around the calorimeters with the drift tubes in ϕ direction, i.e. tangential to circles around the beam pipe. In order to be able to correct for potential chamber deformations due to varying thermal gradients, each MDTs chamber is equipped with an internal optical alignment system. Apart from the regular chambers in the barrel and the end-cap wheels, special modules are installed in order to minimise the acceptance losses due to the ATLAS support structure (the *feets* of the experiment).

Cathode strip chambers

In the region with $|\eta| > 2.0$ in the first layer of the end-caps, the particle flux is too high to allow for safe operation of MDTs chambers. Instead, CSCs, multiwire proportional chambers, are used for precision measurements in this region. The gold-plated tungsten-rhenium anode

† With a small admixture of 300 ppm of water to improve high voltage stability.

wires in the CSCs have a diameter of 30 µm and are oriented in radial direction. The wires are enclosed on both sides by cathode planes, one segmented perpendicular to the wires (thus providing the precision coordinate), the other parallel to the wires. Each chambers is filled with an Ar/CO_2 gas mixture and consists of four wire planes, resulting in four measurements of η and ϕ for each track. In addition to the chamber-internal alignment sensors, ATLAS also employs an optical alignment system in order to align the precision chambers to each other [82].

Resistive plate chambers

RPCs are gaseous parallel electrode-plate chambers that use two resistive plastic laminate plates kept 2 mm apart by insulating spacers. Due to an electric field of roughly 4.9 kV mm^{-1} between the plates, charged particles traversing the chamber cause avalanches of charges that can be read out through capacitive coupling to metallic strips mounted on the outside of the resistive plates. In order to provide tracking information in both coordinates, each RPCs consists of two rectangular units each containing two gas volumes with a total of four pairwise orthogonal sets of readout strips. The tree concentric cylindrical layers of RPCs in the barrel region thus provide six measurements of η and ϕ and cover $|\eta| < 1.05$

Thin gap chambers

The TGCs are not only necessary for triggering in the end-cap MS but also provide measurements of a second coordinate, orthogonal to the measurements of the MDTs. TGCs are multi-wire proportional chambers enclosed by two cathode planes and a wire-to-wire gap of 1.8 mm. The gas mixture of CO_2 and n-pentane allows for a quasi-saturated operation mode resulting in a relatively low gas gain. Each TGCs unit is built from a doublet or triplet of such chambers, separated by a supporting honeycomb structure, In each unit, the azimuthal coordinate is measured by radial copper readout strips, while the bending coordinate is provided by the wire groups.The TGCs are mounted in two concentric disks in each end-cap, one covering the rapidity range $1.05 < |\eta| < 1.92$ and one covering the more forward region $1.92 < |\eta| < 2.4$.

2.2.6 Forward detectors

Apart from the relative luminosity monitor LUCID-2 [95] (introduced in section 2.1.2) located at ±17 m from the IP, ATLAS uses three additional small detectors in the forward region. At ±140 m from the IP, immediately behind the location where the straight beam pipe splits back into two separate beam pipes, lies the Zero-Degree Calorimeter (ZDC) [113]. The ZDC is embedded in an absorber for neutrals mainly measures forward neutrons with $|\eta| > 8.3$ in heavy-ion collisions. Even further out from the IP at ±240 m, lies the Absolute Luminosity for ATLAS (ALFA) detector [114], consisting of scintillating fibre trackers placed in Roman pots [115] measuring the absolute luminosity through small scattering angles of 3 µrad (necessitating the special beam conditions also used for the LUCID-2 calibrations). The last of the forward detectors is the ATLAS Forward Proton (AFP) [116] detector, installed at the end of 2016 and operational since early 2017, is situated ±205 m and ±217 m from the IP and consists of Roman pots containing silicon trackers and time-of-flight detectors. The AFP detectors aims to study very forward protons from elastic and diffractive scattering.

2.2.7 Trigger and data acquisition system

With a nominal bunch spacing of 25 ns, the bunch crossing rate within ATLAS is 40 MHz. Even with only a single *pp* collision event per bunch crossing, a mean event size of $\sim 1.6\,\mathrm{MB}$ results in a data volume of more than $60\,\mathrm{TB\,s^{-1}}$, which is impossible to process and write to disk with current technology. In addition, interesting physics events will often only occur at relatively low rates, and generally be hidden in vast amounts of QCD processes that have much higher cross-sections. In order to reduce the event rate written to disk and focus on interesting signatures worth studying, ATLAS used a two-level trigger system during the Run 2 data-taking period [117].

The Level 1 (L1) trigger [118] is hardware-based and uses only coarse granularity calorimeter and muon detector information as inputs in order to define Regions of Interest (ROIs), i.e. regions in η and ϕ with interesting features. With a decision time of only 2.5 µs per event, the L1 trigger reduces the event rate from the bunch-crossing rate of 40 MHz to 100 kHz. The ROIs generated by the L1 trigger are subsequently processed by the High Level Trigger (HLT) [119], a software-based trigger running on a computing farm. The HLT has access to the full detector granularity in the ROIs as well as the entire event and runs reconstruction algorithms similar to those used in offline analysis, allowing to significantly refine the decisions from the L1 trigger. The HLT reduces the event rate from 100 kHz to 1 kHz, matching the data storage constraints. Data flow from the detectors to the storage elements and between the L1 and HLT trigger elements is handled by the Data Acquisition System (DAQ) [119].

The SUSY search presented in this work uses data recorded with missing transverse momentum ($E_{\mathrm{T}}^{\mathrm{miss}}$) triggers [120]. Selecting events with invisible particles is inherently difficult precisely because these particles do not leave a trace in the detector. As described previously, the L1 trigger uses ROIs to define intresting objects and regions in each event that will be further analyses by the HLT. This technique of reconstructing only partial regions of the instrumented region is not well suited for momentum imbalance triggers that rely on a sum of momenta over the full solid angle. In addition, the significant increase in luminosity in Run 2 of the LHC degrades the $E_{\mathrm{T}}^{\mathrm{miss}}$ resolution in the calorimeters, the only detector component used for the $E_{\mathrm{T}}^{\mathrm{miss}}$ triggers [120]. Two different types of $E_{\mathrm{T}}^{\mathrm{miss}}$ triggers are used in the following, one based on jets (`mht` algorithm), and one implementing local pile-up suppression (`pufit` algorithm). As hadronic jets dominate the visible momentum in most interesting events, using them for $E_{\mathrm{T}}^{\mathrm{miss}}$ computation and triggering is well-motivated. The `mht` algorithm computes the $E_{\mathrm{T}}^{\mathrm{miss}}$ from the negative vectorial sum of the transverse momenta of all jets with a transverse momentum $p_{\mathrm{T}} > 7\,\mathrm{GeV}$ before calibration [120]. The HLT jets are reconstructed and calibrated using a similar procedure as for offline analysis, and are thus corrected for pile-up effects [121]. The `pufit` algorithm takes as input topological clusters formed from electromagnetic and hadronic calorimeter cells in a multistage process common to many ATLAS reconstruction algorithms [122]. It subsequently combines the clusters into η–ϕ patches of approximately jet size and corrects for pile-up effects based on the distribution of the energy deposits in the calorimeter. The `pufit` algorithm assumes that high transverse energy deposits stem from the hard-scatter events, while low transverse energy deposits originate mainly from pile-up effects [120].

2.2.8 Object reconstruction

2.2.9 Monte Carlo simulation

Monte Carlo (MC) methods play a crucial role for simulating physics events in ATLAS. MC simulations are computational algorithms using repeated random sampling to solve complex problems, often the estimation of multi-dimensional integrals for which analytical solutions are not known. According to the law of large numbers the numerical approximations obtained by such a stochastic method become more accurate, the larger the sample size is. In addition, the central limit theorem also allows to state an uncertainty on the estimation of an expected value. This method can in principle be used for any problem with a probabilistic interpretation and is therefore well suited for particle physics where many aspects are inherently connected to Probability Density Functions (pdfs).

is this true?

In the ATLAS experiment, MC methods are not only used in physics analysis to estimate contributions from various physics processes in different phase space regions, but also to simulate particle interactions with the detector material and even finds ample applications in detector design and optimisation as well as physics objects reconstruction techniques. All of these applications rely on the MC simulations being as precise as possible, i.e. correctly describing the physics processes and detector responses underlying the data recorded by the ATLAS experiment. For reasons of more efficient computing resource utilisation and easier software validation, the ATLAS simulation infrastructure [123] can be divided into three main steps:

(i) Event generation,

(ii) Detector simulation,

(iii) Digitisation,

producing an output format identical to that of the DAQ for recorded *pp* collision events, such that the same trigger and reconstruction algorithms can be run over simulated data.

Event generation

simulation tools allow to plugin any Lagrangian and get events at detector level

The majority of *pp* collisions are not interesting for particle physicists in the sense that they only involve soft hadrons travelling along the beam axis. Only a few events actually involve an *hard-scattering* event with high-momentum transfer, rendering them interesting for particle physicists to study. Generating and understanding the final states of these *pp* collision events is an enormously challenging problem as it typically involves hundreds of particles with energies spanning many orders of magnitude [125]. This makes the matrix elements connected to these processes too complicated to be computed beyond the first few orders of perturbation theory. The treatment of divergences and the integration over large phase-spaces further complicates the calculation of experimental observables.

It is not surprising that the simulation of the hard-scatter interaction is at the heart of any MC event generator. Due to the high-momentum transfer scale, the cross section of this process can

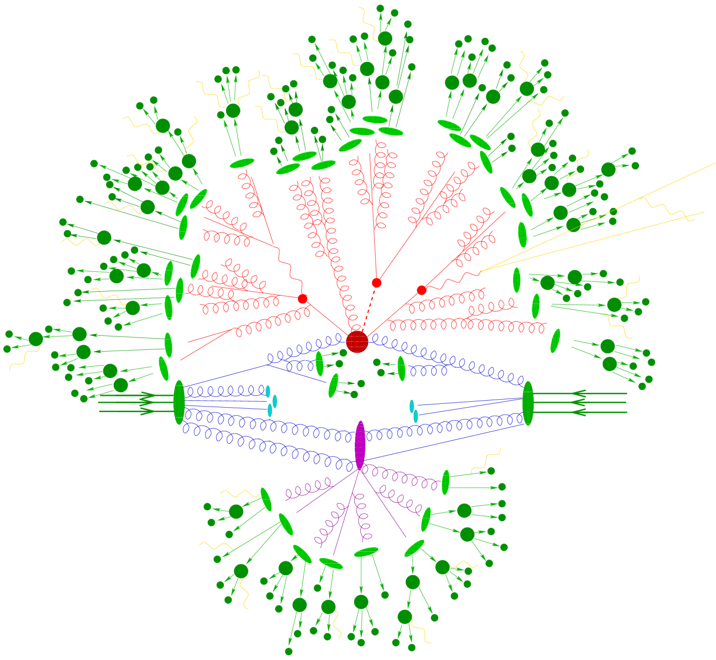

Figure 2.7: Pictorial representation of a $t\bar{t}+H$ event simulated by a MC event generator. The hard interaction (big red blob) is followed by the decay of the two top quarks and the Higgs boson (small red blobs). ISR and FSR are shown as curly blue and red lines, respectively. A second interaction is simulated (purple blob) and contributions from the underlying event are modelled (purple lines). The hadronisation of final-state partons (light green blobs) is followed by the decays of unstable hadrons (dark green blobs). QED radiation (yellow lines) is added at each stage of the event simulation. Figure adapted from [124].

be calculated perturbatively using collinear factorisation [125],

$$\sigma = \sum_{a,b} \int_0^1 \mathrm{d}x_a \, \mathrm{d}x_b \int \mathrm{d}\Phi_n f_a^{h_1}(x_a, \mu_F) f_b^{h_2}(x_b, \mu_F) \times \frac{1}{2x_a x_b s} |\mathcal{M}_{ab\to n}|^2(\Phi_n; \mu_F, \mu_R), \qquad (2.7)$$

with x_a and x_b the momentum fractions of the partons a and b with respect to their parent hadrons h_1 and h_2, μ_F and μ_R are the unphysical factorisation and the renormalisation scales, respectively and $\mathrm{d}\Phi_n$ is the differential final state phase-space element. The phase space integration is typically done using MC sampling methods. The choices for μ_R and μ_F are to some degree arbitrary, but are typically chosen to be in accordance with the logarithmic structure of Quantum Chromodynamics (QCD), such that the matrix elements can be combined with the subsequent parton showers [125]. The Matrix Element (ME) $|\mathcal{M}_{ab\to n}|^2$ can be calculated using different methods [125], with most MC generators employing Leading Order (LO) computations. As LO matrix elements are only reliable for the shapes of the distributions, an additional *K-factor* correcting the normalisation of the cross section to Next-to-leading Order (NLO) is typically used. The probability of finding a parton with momentum fractions x in a hadron h, is given by the PDF $f_a^h(x, \mu_F)$ and depends on the probed factorisation scale μ_F. The PDFs depend on non-perturbative aspects of the proton wave function and can thus not be calculated from first principles. Instead, they are extracted from measurements in deep inelastic scattering experiments (see e.g. [126, 127]). The variety of PDFs provided by different groups, is accessible in a common format through a unified interface implemented by the LHAPDF library [128]. In MC generators, the choice of PDFs not only play a crucial role for the simulation of the hard process, but also in the subsequent parton showers and multiple parton interactions, thus influencing both cross sections and event shapes.

Fixed-order matrix elements work well for describing separated, hard partons but is not sufficient to describe soft and collinear partons. Higher order effects from gluon radiation can be simulated using a *parton shower* algorithm. The emitted gluons will radiate additional gluons or split into quark–antiquark pairs which can in turn undergo gluon radiation. The parton shower thus describes an evolutionary process in momentum transfer scales from the scale of the hard scatter interaction down to the infrared scale $\mathcal{O}(1\,\mathrm{GeV})$ where QCD becomes non-perturbative and partons are confined into hadrons. Both ISR and FSR are simulated through the parton shower. As opposed to ME calculations, parton showers offer poor modelling of few hard partons, but excel in the simulation of collinear and soft multi-parton states.

In order to avoid double counting, the hard partons described by the calculation of the ME and the soft collinear emissions of the parton shower have to be connected to each other. This is done either through *matching* or *merging*. ME matching approaches [129] integrate higher-order corrections to an inclusive process with the parton shower [125]. Merging techniques like the CKKW [130] or CKKW-L [131] methods define an unphysical merging scale which can be understood as a jet resolution scale such that higher order ME corrections are only calculated for jets above that scale (while jets below that scale are modelled with the parton shower).

Next, additional activity in the event not directly associated to the hard process is simulated. The underlying event is typically defined to be all additional activity after ISR and FSR off the hard process has been taken into account [125]. Furthermore, *multiple interactions* can occur in a single pp collision. The modelling of multiple interactions involves multiple hard scatter processes per pp collision as well as multiple soft interactions in addition to the hard scatter process.

Once the parton showering reaches energies of $\mathcal{O}(1\,\mathrm{GeV})$, entering the non-perturbative regime of QCD, the coloured objects need to be transformed into colourless states. This so-called *hadronisation* step cannot be calculated from first principles but has to be modelled, typically with either a *string* or a *cluster* model. The most advanced of the string models is the *Lund* model [132, 133]. It starts from linear confinement and considers a linear potential between a $q\bar{q}$ pair, that can be thought of as a uniform colour flux tube stretching between the q and $\bar{q}$, with a transverse dimension of the order of typical hadronic size (i.e. around 1 fm). As the $q\bar{q}$ pair moves apart, the flux tube stretches in length, leading to an increase in potential energy, finally breaking apart once enough energy is available to create a new $q'\bar{q}'$ pair, resulting in two colourless quark pairs $q\bar{q}'$ and $q'\bar{q}$. The new quark pairs can again move apart and break up further, leading to quark anti-quark pairs with low relative momentum, forming the final hadrons. The cluster model is based on the preconfinement property of parton showers [134], stating that the colourless clusters of partons can be formed at any evolution scale Q_0 of the parton shower, and result in universal invariant mass distributions that depend only on Q_0 and the QCD scale Λ, but not on the energy scale Q or nature of the hard process at the origin of the parton shower [125]. The universal invariant mass distribution holds in the asymptotic limit where $Q_0 \ll Q$. If further $Q_0 \gg \Lambda$, then the mass, momentum and multiplicity distributions of the colourless clusters can even be calculated perturbatively [125]. Cluster models start with non-perturbative splitting of gluons and $q\bar{q}$ pairs, followed by the formation of clusters from colour-connected pairs. Clusters further split up until the Q_0 scale is reached, where they form the final mesons.

As not all hadrons formed in the hadronisation process are stable, the affected hadrons need to be decayed until they form resonances stable enough to reach the detector material. In addition QED radiation, that can happen at any time during the event, needs to be simulated. This is typically done with algorithms similar to the ones used for the parton shower.

The simulation steps that cannot be performed from first principles but rely on phenomenological models (underlying event, parton shower, hadronisation) introduce free parameters that need to be derived or *tuned* from parameter optimisations against experimental data. In ATLAS, the output of MC event generators is stored in so-called EVNT data format containing HepMC [135] event records. Although only the stable final-state particles are propagated to the detector simulation, the HepMC event record contains the entire connected tree as so-called *Monte Carlo truth*.

Detector simulation

Only the final-state particles generated by the MC event generator are read into the detector simulation. In ATLAS, the full detector simulation is handled GEANT4 [136], a toolkit providing detailed models for physics processes and an infrastructure for particle transportation through a geometry. GEANT4 has knowledge about the full detector geometry as well as the materials used in the subdetectors and is able to compute the energy deposits (so-called *hits*) from single particles in the different sensitive portions of the detector components. The GEANT4 simulation adds information to the Monte Carlo truth content created during the event generation, including however only the most relevant tracks (mostly from the ID) due to size constraints [123].

The complicated detector geometry and the detailed description of physics processes requires large computing resources for the full detector simulation using GEANT4, rendering it inaccessible for many physics studies requiring large statistics. Several varieties of fast simulations are available to this end. One of the most-used ones is ATLFAST-II [123] , a fast simulation that uses the GEANT4 full simulation only for the ID and MS. The slow simulation in the calorimeters—that takes about 80% of the full simulation time—is replaced with FASTCALOSIM [137], using parameterised electromagnetic and hadronic showers. Compared to the $\mathcal{O}(10^3\,\mathrm{s})$ simulation time per event in the full simulation, the ATLFAST-II detector simulation only takes $\mathcal{O}(10^2\,\mathrm{s})$ [123].

Digitisation

During the digitisation step, the hits from the detector simulation are converted into detector responses, so-called *digits* that are typically produced when currents or voltages in the respective readout channels rise above a certain threshold in a given time window. The digitisation considers a modelling of the peculiarities of each detector component, including electronic noise and cross-talk [123]. The effects from out-of-time and in-time pile-up are also considered by reading in multiple events and overlaying their hits. In order to match the true pile-up distribution in data, the number of events to overlay per bunch crossing can be set at run time. As described in section 2.1.1, effects from cavern background, beam halo and beam gas can either be mitigated or removed at analysis level and are therefore typically not simulated.

Chapter 3

Statistical data analysis

Statistical models are used in order to order to quantify the correspondence between theoretical predictions and the experimental observations in searches for SUSY. This chapter introduces the statistical concepts, methods and formulae used in this work for statistical inference. A frequentist approach to statistics is employed, interpreting probabilities as the frequencies of the outcomes of repeatable experiments that may either be real, based on computer simulations, or mathematical abstraction [5, 138]. The ensuing description largely follows [138, 139]

3.1 The likelihood function

In measurements in high energy physics, a *statistical model* $f(\boldsymbol{x}|\boldsymbol{\phi})$ is a parametric family of Probability Density Functions (pdfs) describing the probability of observing data $\boldsymbol{x}$ given a set of model parameters ϕ that typically describe parameters of the physical theory or unknown detector effects. The *likelihood function* $L(\boldsymbol{\phi})$ is then numerically equivalent to $f(\boldsymbol{x}|\boldsymbol{\phi})$ with $\boldsymbol{x}$ fixed. As opposed to the pdf $f(\boldsymbol{x})$ which describes the value of f as a function of $\boldsymbol{x}$ given a fixed set of parameters $\boldsymbol{\phi}$, the likelihood refers to the value of f as a function of $\boldsymbol{\phi}$ given a fixed value of $\boldsymbol{x}$.

Searches for BSM physics are typically centred around the measurement of several disjoint binned distributions (called *channels* c) that are each associated with different event selection criteria (as opposed to different scattering processes) yielding observed event counts $\boldsymbol{n}$. In such counting experiments where each event is independently drawn from the same underlying distribution, each bin is fundamentally described by a Poisson term. The Poisson probability to observe n events with a expectation of ν events, is given by

$$\mathrm{Pois}(n|\nu) = \frac{\nu^n}{n!}e^{-\nu}. \tag{3.1}$$

The expectation ν_{cb} in each channel c and bin b is a sum over the set of physics processes considered (called *samples*). The sample-wise rates are in general a function of the the model parameters $\boldsymbol{\phi}$, that can either be *free parameters* $\boldsymbol{\eta}$ or *constrained parameters* $\boldsymbol{\chi}$. Free parameters directly determined by the Poisson terms for the data observations are called *normalisation factors*. The constrained parameters represent the systematic uncertainties considered in the model. The degree to which they cause a deviation of the expected event rates from the nominal event rates is limited through *constraint terms* $c_{\boldsymbol{\chi}}(a_{\boldsymbol{\chi}}|\boldsymbol{\chi})$ that can be viewed as *auxiliary measurements* with global observed data $\boldsymbol{a}$.

For a given observation $\boldsymbol{x} = (\boldsymbol{n}, \boldsymbol{a})$ of observed events $\boldsymbol{n}$ and auxiliary data $\boldsymbol{a}$, the likelihood then reads

$$L(\boldsymbol{\eta}, \boldsymbol{\chi}) = \prod_{c \in \text{channels}} \prod_{b \in \text{bins}_c} \text{Pois}(n_{cb}|\nu_{cb}(\boldsymbol{\eta}, \boldsymbol{\chi})) \prod_{\chi \in \boldsymbol{\chi}} c_\chi(a_\chi|\chi), \tag{3.2}$$

where, given a certain integrated luminosity, n_{cb} and ν_{cb} refer to the corresponding observed and expected rate of events, respectively [140]. Most of the systematic uncertainties are so-called *interpolation parameters* $\boldsymbol{\alpha}$ representing either normalisation uncertainties or correlated shape uncertainties. Their constraint terms $c_{\boldsymbol{\alpha}}(a_{\boldsymbol{\alpha}}|\boldsymbol{\alpha})$ are parametrised by a Gaussian with mean $a = 0|\alpha$ and variance $\sigma = 1$, with $\alpha = 0$ representing the nominal value. The *up* and *down* variations are then given by $\alpha = \pm 1$, thus representing $\pm 1\sigma$ variations. The impact of any given value of the parameter on the event rates is then evaluated through polynomial interpolation and exponential extrapolation, a method that avoids discontinuous first and second derivatives at $\alpha = 0$ and ensures positive values for the predicted event rates [141].

Explain this further

Sample rates derived from theory calculations (i.e. MC simulation), are scaled to the integrated luminosity corresponding to the observed data. The integrated luminosity is itself a measurement that is subject to uncertainties. Therefore, an additional constraint term in the likelihood is needed. It is parametrised by a Gaussian with mean corresponding to the nominal integrated luminosity measurement and variance equal to the integrated luminosity measurement uncertainty.

Uncertainties arising from the finite size of the MC datasets often used to derive estimated event rates are modelled by bin-wise scale factors γ_b. The constraint terms are Gaussian distributions with central value equal to unity and variances calculated from the individual uncertainties of the samples defined in the respective channel.

As the event rate in a given bin can depend on multiple parameters, and, likewise, a single parameter can affect the expected event rate in multiple bins, correlations between the model parameters $\boldsymbol{\phi}$ can occur.

The above prescription for building binned likelihoods is called the HistFactory template [141]. In this work, two independent implementations of the HistFactory template are used. The first implementation uses RooFit and RooStats for fitting (using `Minuit`), and HistFitter as interface for steering fits and hypothesis tests and bookkeeping of results. The second implementation uses `pyhf`, a pure-`python` implementation of HistFactory that is independent from ROOT and uses computational graph libraries like `PyTorch`, TensorFlow and JAX to speed up the minimisation process.

Apart from separating the model parameter set into free and constrained parameters $\boldsymbol{\phi} = (\boldsymbol{\eta}, \boldsymbol{\chi})$, a separate partition $\boldsymbol{\phi} = (\boldsymbol{\psi}, \boldsymbol{\theta})$ is frequently used in the context of hypothesis testing. Here, $\boldsymbol{\eta}$ are so-called *parameters of interests* of the model for which hypothesis tests are performed, and $\boldsymbol{\theta}$ are *nuisance parameters* that are not of immediate interest but need to be accounted for to correctly model the data. In the search presented in this work, the only Parameter of Interest (POI) is the *signal strength* parameter μ, representing the ratio of the signal process cross section to its reference cross section as expected from theory. The expectation ν_i in each bin i can be parametrised through

$$\nu_b = \mu S_b + B_b, \tag{3.3}$$

where S_b and B_b are the bin-wise expected signal and background rates, respectively. Fixing $\mu = 0$ thus yields an expected event rate containing only Standard Model (SM) processes (thus called *background-only*), while $\mu = 1$ represents a *signal-plus-background* description at nominal signal cross section. Scanning multiple values of μ allows to set limits on the visible cross sections of the signal models considered in the search.

3.2 Parameter estimation

Given a likelihood $L(\mu, \boldsymbol{\phi})$ for a fixed set of observations $\boldsymbol{x}$, a measurement can be understood as a parameter estimation. In general, an estimator $\hat{\phi}$ is a function of the observed data used to estimate the true value of the model parameter ϕ.

In particle physics, the most commonly used estimator is the Maximum Likelihood Estimator (MLE). The MLEs for the model parameters $\hat{\boldsymbol{\phi}}$ are defined to be the parameter values that maximise $L(\boldsymbol{\phi})$, or, equivalently maximise $\ln L(\boldsymbol{\phi})$ and minimises $-\ln L(\boldsymbol{\phi})$. The logarithm of the likelihood is used for computational reasons, as it not only reduces the computational complexity by avoiding exponentials and products, but also avoids avoids problems of running out of floating point precision. As the logarithm is a monotonically increasing function, $\ln L(\boldsymbol{\phi})$ has maxima at the same parameter values as $L(\boldsymbol{\phi})$.

The MLE $\hat{\boldsymbol{\phi}}$ can thus be found by solving

$$\frac{\partial \ln L}{\partial \phi_i} = 0, \tag{3.4}$$

where the index i runs over all parameters. The solution typically needs to be found numerically using minimisation algorithms. In the following, the parameter estimation is referred to as a *fit* of the model to data, and the maximum likelihood estimates of the parameters are consequently called *best-fit values.*

3.3 Statistical tests

In addition to estimating the values of model parameters, searches for SUSY are naturally interested in claiming discovery (or alternatively exclusion) of hypothesised signal models. In the frequentist approach, this can be formulated in terms of hypothesis tests, evaluating a *null hypothesis* H_0 against an *alternative hypothesis* H_1, with the goal of rejecting the null hypothesis. For discovering a new signal process, H_0 is defined to describe only known SM processes (called *background-only* hypothesis), while H_1 describes both SM background processes as well as the signal process (called *signal plus background hypothesis*). When excluding a signal model the signal plus background hypothesis takes over the role of H_0 and is tested against the background-only hypothesis.

The degree of agreement of observed data with a certain hypothesis H is quantified by computing a p-value, representing the probability of finding data of greater or more extreme incompatibility under assumption of H. The hypothesis can then be considered as excluded if its observed p-value is below a specified threshold. It is common to convert the p-value into a *significance* Z, defined in such a way that a Gaussian distributed observable with measured value Z standard deviations above its mean gives a one-sided upper tail probability equal to p. This yields the expression

$$Z = \Phi^{-1}(1-p), \tag{3.5}$$

where Φ^{-1} is the quantile of the standard Gaussian. Discovery of a signal then conventionally requires a significance of at least $Z = 5$, while exclusion of a signal hypothesis at 95% confidence level requires a p-value of 0.05, i.e. $Z = 1.64$ [139].

The p-values are calculated using a *test statistic* that parameterises the compatibility between the hypothesis and data in a single value. At the LHC experiments, the test statistics used for hypothesis testing are based on the *profile likelihood ratio*

$$\lambda(\mu) = \frac{L(\mu, \hat{\hat{\boldsymbol{\theta}}}(\mu))}{L(\hat{\mu}, \hat{\boldsymbol{\theta}})}, \tag{3.6}$$

where the *conditional maximum likelihood estimates* $\hat{\hat{\boldsymbol{\theta}}}$ are the values of $\boldsymbol{\theta}$ that maximise the likelihood with μ fixed. The profile likelihood ratio depends explicitly on μ, and implicitly on $\boldsymbol{x} = (\boldsymbol{n}, \boldsymbol{a})$, but is asymptotically (i.e. in the limit of a large number of events)independent of the nuisance parameters $\boldsymbol{\theta}^{\dagger}$. The asymptotic independence from $\boldsymbol{\theta}$ follows from Wald's and Wilks' theorems [142, 143] and is one of the main motivations for using the profile likelihood ratio, as it avoids the problem of having to compute p-values for all possible values of ***theta***. The profile likelihood ratio takes values between 0 and 1, with $\lambda(\mu) = 1$ corresponding to cases where the tested value of μ is in good agreement with the observed data.

As the rate of signal processes considered in this work is non-negative, an estimator for μ must satisfy $\hat{\mu} \geq 0$. In order to avoid the formal complications of having a boundary at $\mu = 0$, it is convenient to consider an effective estimator $\hat{\mu}$ that is allowed to become negative, provided that the respective Poisson terms for $\mu S_b + B_b$ remain positive. By imposing the constraint $\mu \geq 0$ on the test statistic itself, it is possible to avoid the formal problems of having a boundary at $\mu = 0$. This leads to the definition of

$$\tilde{\lambda}(\mu) = \begin{cases} \frac{L(\mu, \hat{\hat{\boldsymbol{\theta}}}(\mu))}{L(\hat{\mu}, \hat{\boldsymbol{\theta}})}, & \hat{\mu} \geq 0, \\ \frac{L(\mu, \hat{\hat{\boldsymbol{\theta}}}(\mu))}{L(0, \hat{\hat{\boldsymbol{\theta}}}(0))}, & \hat{\mu} < 0, \end{cases} \tag{3.7}$$

where $\hat{\hat{\boldsymbol{\theta}}}(0)$ and $\hat{\hat{\boldsymbol{\theta}}}(\mu)$ are the conditional MLEs of $\boldsymbol{\theta}$ given a signal strength parameter of 0 and μ, respectively.

† Eliminated by choosing specific values of the nuisance parameters for a given $\boldsymbol{x}$ and μ, often referred to as *profiling*.

Discovery

For the important special case where $\mu = 0$ is tested in a model with $\mu \geq 0$, i.e. discovery of a non-negative signal (rejection of the $\mu = 0$ hypothesis), the test statistic in eq. (3.7) becomes

$$q_0 = \tilde{t}_0 = \begin{cases} -\ln \lambda(0), & \hat{\mu} \geq 0, \\ 0, & \hat{\mu} < 0. \end{cases} \tag{3.8}$$

This definition ensures that the $\mu = 0$ hypothesis is not rejected due to a downward fluctuation in data, causing $\hat{\mu} < 0$. In case more events are seen in data than expected based on the background-only hypothesis, eq. (3.8) produces increasingly large values of q_0, corresponding to an increasing incompatibility between data and the background-only hypothesis. The p-value quantifying the disagreement between the $\mu = 0$ hypothesis and data can then be computed using

$$p_0 = \int_{q_{0,\mathrm{obs}}}^{\infty} f(q_0|0)\,\mathrm{d}q, \tag{3.9}$$

with $q_{0,\mathrm{obs}}$ the observed value of the test statistic q_0 in data and $f(q_0|0)$ the pdf of q_0 under assumption of the $\mu = 0$ hypothesis. In the asymptotic limit with a single POI, the test statistic q_0 can be written as

$$q_0 = \begin{cases} \hat{\mu}^2/\sigma^2, & \hat{\mu} \geq 0, \\ 0, & \hat{\mu} < 0, \end{cases} \tag{3.10}$$

where $\hat{\mu}$ has a Gaussian distribution with mean μ' and variance σ^2. In the case where $\mu' = 0$, the pdf of q_0 has the form of a half chi-square distribution with one degree of freedom, and its cumulative distribution is $F(q_0|0) = \Phi(\sqrt{q_0})$. Using eq. (3.5), the p-value obtained with eq. (3.9) can be expressed with the significance Z_0 as

$$Z_0 = \sqrt{q_0}. \tag{3.11}$$

Exclusion and upper limits

If the background-only ($\mu = 0$) hypothesis cannot be rejected, the hypotheses can be switched around and instead the signal plus background hypothesis can be tested. For excluding the signal plus background ($\mu = 1$) hypothesis and setting upper limits on the signal strength μ, the test statistic is defined as

$$\tilde{q}_\mu = \begin{cases} -2\ln \tilde{\lambda}(\mu), & \hat{\mu} \geq 0, \\ 0, & \hat{\mu} < 0. \end{cases} = \begin{cases} -2\ln \frac{L(\mu,\hat{\hat{\boldsymbol{\theta}}}(\mu))}{L(\hat{\mu},\hat{\boldsymbol{\theta}})}, & \hat{\mu} \geq 0, \\ -2\ln \frac{L(\mu,\hat{\hat{\boldsymbol{\theta}}}(\mu))}{L(0,\hat{\hat{\boldsymbol{\theta}}}(0))}, & 0 \leq \hat{\mu} \leq \mu, \\ 0 & \hat{\mu} > \mu. \end{cases} \tag{3.12}$$

Setting $\tilde{q}_\mu = 0$ in the case where $\hat{\mu} > \mu$ ensures that an overfluctuation of data is not considered as evidence against the signal hypothesis. This is opposed to the definition of q_0, where an underfluctuation of data ($\hat{\mu} < \mu$) is not regarded to be evidence against the background-only hypothesis. The p-value, quantifying the level of agreement between data and the tested value

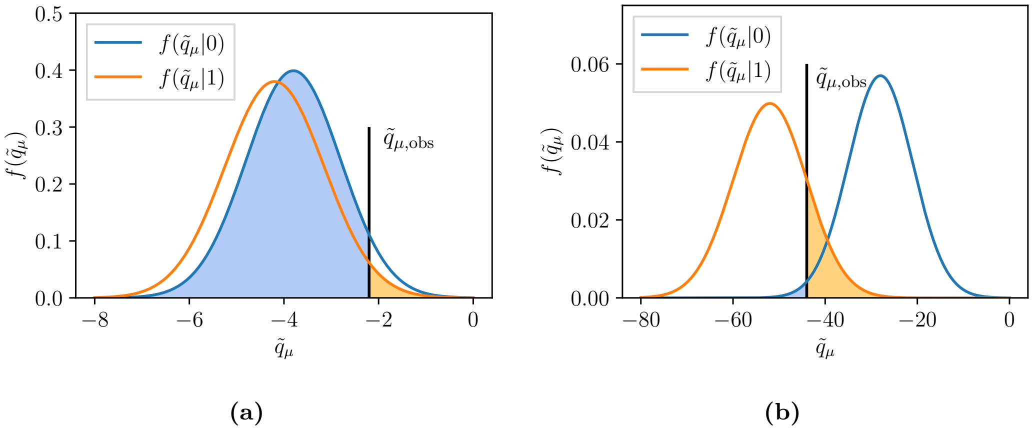

Figure 3.1: Distribution of the pdfs of the signal plus background (in orange) and background-only (in blue) models. The coloured areas represent the p_{s+b} and p_b values, respectively. Figure (a) shows a case where both pdfs are close together, while figure (a) shows a case where both a well separated. Adapted from [144].

of μ is then given by

$$p_\mu = \int_{\tilde{q}_{\mu,\text{obs}}}^{\infty} f(\tilde{q}_\mu|\mu)\,\mathrm{d}\tilde{q}_\mu, \tag{3.13}$$

where, as before, $\tilde{q}_{\mu,\text{obs}}$ is the observed value of the test statistic in data and $f(\tilde{q}_\mu|\mu)$ is the pdf of $\tilde{q}_\mu$ given the hypothesis μ. In the asymptotic limit, the test statistic $\tilde{q}_\mu$ can be written as

$$\tilde{q}_\mu = \begin{cases} \mu^2\sigma^2 - 2\mu\hat{\mu}/\sigma^2, & \hat{\mu} \geq 0, \\ (\mu - \hat{\mu})^2\sigma^2, & 0 \leq \hat{\mu} \leq \mu, \\ 0 & \hat{\mu} > \mu, \end{cases} \tag{3.14}$$

which yields for the significance Z_μ the expression

$$Z_\mu = \begin{cases} \sqrt{\tilde{q}_\mu}, & 0 < \tilde{q}_\mu \leq \mu^2/\sigma^2 \\ \frac{\tilde{q}_\mu + \mu^2/\sigma^2}{2\mu/\sigma}, & \tilde{q}_\mu > \mu^2/\sigma^2. \end{cases} \tag{3.15}$$

3.4 Asimov dataset

3.5 Intervals and limits

3.6 CL_s approach

In the CL_{s+b} method, a signal plus background model is excluded if $p_{s+b} < \alpha$, where α is defined by the desired confidence level, typically $CL = 1 - \alpha = 95\%$, and p_{s+b} can be calculated using the test statistic $\tilde{q}_\mu$ (with $\mu = 1$) introduced before. If the experiment has very low sensitivity to a specific signal plus background model, e.g. because the production cross section is too low, the test statistic of the signal plus background model will be very close to that of the background-only model. In case of an underfluctuation in data, the $\mu = 1$ model can then falsely be excluded, even though no sensitivity is expected. Figure 3.1 illustrates this with a simple example. In fact, the exclusion of models to which the experiment has no sensitivity has a probability of at least α [144].

This problem can be remedied by adopting the CL_s method [145], altering the threshold for excluding a model in a way to avoid exclusion of models to which the experiment has very low sensitivity. The CL_s value is defined as

$$CL_s = \frac{p_{s+b}}{1 - p_b}, \tag{3.16}$$

where p_b is the p-value of the background-only hypothesis. If the distributions of the test statistics for the signal plus background and the background-only models are close a small value of p_{s+b} due to an underfluctuation in data will entail a large value of p_b. Consequently, in the calculation of the CL_s value, p_{s+b} will be penalised by $1 - p_b$ (that will be close to 0), resulting in $CL_s > p_{s+b}$, preventing the exclusion of the signal plus background model. Conversely, in the case where the two test statistics are well-separated and $p_{s+b} < \alpha$, then p_b will also be small and thus CL_s will be close to p_{s+b} obtained by the frequentist approach.

Part II

The 1-lepton analysis

Chapter 4

Analysis overview

4.1 The 1-lepton final state

4.2 Standard Model backgrounds

4.3 Object reconstruction

4.4 Triggers

Chapter 5

Signal region optimisation

Chapter 6

Background estimation

Chapter 7

Systematic uncertainties

Chapter 8

Results

Part III

Reinterpretation

Chapter 9

Simplified likelihoods

Chapter 10

Reinterpretation in the pMSSM

Part IV

Summary and Outlook

Chapter 11

Summary

Here be dragons/

Part V

Appendix

Appendix A

A.1 N-1 plots for cut-scan results

Appendix B

B.1 Scatter plots comparing truth and reco yields in the SRs

Abbreviations

AFP ATLAS Forward Proton. 50

ALFA Absolute Luminosity for ATLAS. 50

BSM Beyond the Standard Model. 41, 42, 49, 57

CSCs Cathode Strip Chambers. 49, 50

DAQ Data Acquisition System. 51, 52

EM Electromagnetic. 47, 48

EMEC Electromagnetic end-cap calorimeter. 48

FCal Forward Calorimeter. 48

FSR Final State Radiation. 53, 54

HEC Hadronic end-cap calorimeter. 48

HLT High Level Trigger. 51

IBL Insertable B-Layer. 46

ID Inner Detector. 45–48, 55

IP Interaction Point. 43–45, 50

ISR Initial State Radiation. 53, 54

L1 Level 1. 51

LAr liquid argon. 47–49

LEP Large Electron Positron. 37

LHC Large Hadron Collider. 37–39, 41–43

LO Leading Order. 53

MC Monte Carlo. 52, 53, 55, 58

MDTs Monitoring Drift Tubes. 49, 50

ME Matrix Element. 53, 54

MLE Maximum Likelihood Estimator. 59, 60

MS Muon Spectrometer. 49, 50, 55

NLO Next-to-leading Order. 53

PDF Parton Distribution Function. 44, 53

pdf Probability Density Function. 52, 57, 61, 62

POI Parameter of Interest. 58, 61

PS Proton Synchrotron. 38

QCD Quantum Chromodynamics. 53, 54

QED Quantum Electrodynamics. 53, 54

RF Radio frequency. 38, 39

ROIs Regions of Interest. 51

RPCs Resistive Plate Chambers. 49, 50

SCT Silicon Microstip Tracker. 45, 46

SM Standard Model. 59

SPS Super Proton Synchrotron. 38

SUSY Supersymmetry. 37, 41, 51, 57, 59

TGCs Thin Gap Chambers. 49, 50

TRT Transition Radiation Tracker. 45, 46

vdM van der Meer. 42

ZDC Zero-Degree Calorimeter. 50

Bibliography

[1] I. C. Brock and T. Schorner-Sadenius, *Physics at the terascale*. Wiley, Weinheim, 2011. https://cds.cern.ch/record/1354959.

[2] M. E. Peskin and D. V. Schroeder, *An Introduction to quantum field theory*. Addison-Wesley, Reading, USA, 1995. http://www.slac.stanford.edu/~mpeskin/QFT.html.

[3] S. P. Martin, "A Supersymmetry primer," `arXiv:hep-ph/9709356 [hep-ph]`. [Adv. Ser. Direct. High Energy Phys.18,1(1998)].

[4] P. J. Mohr, D. B. Newell, and B. N. Taylor, "CODATA Recommended Values of the Fundamental Physical Constants: 2014," *Rev. Mod. Phys.* **88** no. 3, (2016) 035009, `arXiv:1507.07956 [physics.atom-ph]`.

[5] P. D. Group, "Review of Particle Physics," *Progress of Theoretical and Experimental Physics* **2020** no. 8, (08, 2020) , `https://academic.oup.com/ptep/article-pdf/2020/8/083C01/34673722/ptaa104.pdf`. https://doi.org/10.1093/ptep/ptaa104. 083C01.

[6] **Super-Kamiokande** Collaboration, Y. Fukuda *et al.*, "Evidence for oscillation of atmospheric neutrinos," *Phys. Rev. Lett.* **81** (1998) 1562–1567, `arXiv:hep-ex/9807003 [hep-ex]`.

[7] Z. Maki, M. Nakagawa, and S. Sakata, "Remarks on the unified model of elementary particles," *Prog. Theor. Phys.* **28** (1962) 870–880. [,34(1962)].

[8] N. Cabibbo, "Unitary symmetry and leptonic decays," *Phys. Rev. Lett.* **10** (Jun, 1963) 531–533. https://link.aps.org/doi/10.1103/PhysRevLett.10.531.

[9] M. Kobayashi and T. Maskawa, "CP Violation in the Renormalizable Theory of Weak Interaction," *Prog. Theor. Phys.* **49** (1973) 652–657.

[10] E. Noether and M. A. Tavel, "Invariant variation problems," `arXiv:physics/0503066`.

[11] J. C. Ward, "An identity in quantum electrodynamics," *Phys. Rev.* **78** (Apr, 1950) 182–182. https://link.aps.org/doi/10.1103/PhysRev.78.182.

[12] Y. Takahashi, "On the generalized ward identity," *Il Nuovo Cimento (1955-1965)* **6** no. 2, (Aug, 1957) 371–375. https://doi.org/10.1007/BF02832514.

[13] G. 'tHooft, "Renormalization of massless yang-mills fields," *Nuclear Physics B* **33** no. 1, (1971) 173 – 199. http://www.sciencedirect.com/science/article/pii/0550321371903956.

[14] J. Taylor, "Ward identities and charge renormalization of the yang-mills field," *Nuclear Physics B* **33** no. 2, (1971) 436 – 444. http://www.sciencedirect.com/science/article/pii/0550321371902975.

[15] A. A. Slavnov, "Ward identities in gauge theories," *Theoretical and Mathematical Physics* **10** no. 2, (Feb, 1972) 99–104. https://doi.org/10.1007/BF01090719.

[16] C. N. Yang and R. L. Mills, "Conservation of isotopic spin and isotopic gauge invariance," *Phys. Rev.* **96** (Oct, 1954) 191–195. https://link.aps.org/doi/10.1103/PhysRev.96.191.

[17] K. G. Wilson, "Confinement of quarks," *Phys. Rev. D* **10** (Oct, 1974) 2445–2459. https://link.aps.org/doi/10.1103/PhysRevD.10.2445.

[18] T. DeGrand and C. DeTar, *Lattice Methods for Quantum Chromodynamics*. World Scientific, Singapore, 2006. https://cds.cern.ch/record/1055545.

[19] S. L. Glashow, "Partial-symmetries of weak interactions," *Nuclear Physics* **22** no. 4, (1961) 579 – 588. http://www.sciencedirect.com/science/article/pii/0029558261904692.

[20] S. Weinberg, "A model of leptons," *Phys. Rev. Lett.* **19** (Nov, 1967) 1264–1266. https://link.aps.org/doi/10.1103/PhysRevLett.19.1264.

[21] A. Salam and J. C. Ward, "Weak and electromagnetic interactions," *Il Nuovo Cimento (1955-1965)* **11** no. 4, (Feb, 1959) 568–577. https://doi.org/10.1007/BF02726525.

[22] C. S. Wu, E. Ambler, R. W. Hayward, D. D. Hoppes, and R. P. Hudson, "Experimental test of parity conservation in beta decay," *Phys. Rev.* **105** (Feb, 1957) 1413–1415. https://link.aps.org/doi/10.1103/PhysRev.105.1413.

[23] M. Gell-Mann, "The interpretation of the new particles as displaced charge multiplets," *Il Nuovo Cimento (1955-1965)* **4** no. 2, (Apr, 1956) 848–866. https://doi.org/10.1007/BF02748000.

[24] K. Nishijima, "Charge Independence Theory of V Particles*," *Progress of Theoretical Physics* **13** no. 3, (03, 1955) 285–304, `https://academic.oup.com/ptp/article-pdf/13/3/285/5425869/13-3-285.pdf`. https://doi.org/10.1143/PTP.13.285.

[25] T. Nakano and K. Nishijima, "Charge Independence for V-particles*," *Progress of Theoretical Physics* **10** no. 5, (11, 1953) 581–582, `https://academic.oup.com/ptp/article-pdf/10/5/581/5364926/10-5-581.pdf`. https://doi.org/10.1143/PTP.10.581.

[26] F. Englert and R. Brout, "Broken symmetry and the mass of gauge vector mesons," *Phys. Rev. Lett.* **13** (Aug, 1964) 321–323. https://link.aps.org/doi/10.1103/PhysRevLett.13.321.

[27] P. W. Higgs, "Broken symmetries and the masses of gauge bosons," *Phys. Rev. Lett.* **13** (Oct, 1964) 508–509. https://link.aps.org/doi/10.1103/PhysRevLett.13.508.

[28] P. W. Higgs, "Spontaneous symmetry breakdown without massless bosons," *Phys. Rev.* **145** (May, 1966) 1156–1163. https://link.aps.org/doi/10.1103/PhysRev.145.1156.

[29] Y. Nambu, "Quasiparticles and Gauge Invariance in the Theory of Superconductivity," *Phys. Rev.* **117** (1960) 648–663. [,132(1960)].

[30] J. Goldstone, "Field Theories with Superconductor Solutions," *Nuovo Cim.* **19** (1961) 154–164.

[31] V. Brdar, A. J. Helmboldt, S. Iwamoto, and K. Schmitz, "Type-I Seesaw as the Common Origin of Neutrino Mass, Baryon Asymmetry, and the Electroweak Scale," *Phys. Rev. D* **100** (2019) 075029, `arXiv:1905.12634 [hep-ph]`.

[32] G. 't Hooft and M. Veltman, "Regularization and renormalization of gauge fields," *Nuclear Physics B* **44** no. 1, (1972) 189 – 213. http://www.sciencedirect.com/science/article/pii/0550321372902799.

[33] F. Zwicky, "Die Rotverschiebung von extragalaktischen Nebeln," *Helv. Phys. Acta* **6** (1933) 110–127. https://cds.cern.ch/record/437297.

[34] V. C. Rubin and W. K. Ford, Jr., "Rotation of the Andromeda Nebula from a Spectroscopic Survey of Emission Regions," *Astrophys. J.* **159** (1970) 379–403.

[35] G. Bertone, D. Hooper, and J. Silk, "Particle dark matter: Evidence, candidates and constraints," *Phys. Rept.* **405** (2005) 279–390, `arXiv:hep-ph/0404175`.

[36] D. Clowe, M. Bradac, A. H. Gonzalez, M. Markevitch, S. W. Randall, C. Jones, and D. Zaritsky, "A direct empirical proof of the existence of dark matter," *Astrophys. J.* **648** (2006) L109–L113, `arXiv:astro-ph/0608407 [astro-ph]`.

[37] A. Taylor, S. Dye, T. J. Broadhurst, N. Benitez, and E. van Kampen, "Gravitational lens magnification and the mass of abell 1689," *Astrophys. J.* **501** (1998) 539, `arXiv:astro-ph/9801158`.

[38] C. Bennett *et al.*, "Four year COBE DMR cosmic microwave background observations: Maps and basic results," *Astrophys. J. Lett.* **464** (1996) L1–L4, `arXiv:astro-ph/9601067`.

[39] G. F. Smoot *et al.*, "Structure in the COBE Differential Microwave Radiometer First-Year Maps," *ApJS* **396** (September, 1992) L1.

[40] **WMAP** Collaboration, "Nine-year Wilkinson Microwave Anisotropy Probe (WMAP) Observations: Final Maps and Results," *ApJS* **208** no. 2, (October, 2013) 20, `arXiv:1212.5225 [astro-ph.CO]`.

[41] **WMAP** Collaboration, "Nine-year Wilkinson Microwave Anisotropy Probe (WMAP) Observations: Cosmological Parameter Results," *ApJS* **208** no. 2, (October, 2013) 19, `arXiv:1212.5226 [astro-ph.CO]`.

[42] **Planck** Collaboration, "Planck 2018 results. I. Overview and the cosmological legacy of Planck," *Astron. Astrophys.* **641** (2020) A1, `arXiv:1807.06205 [astro-ph.CO]`.

[43] A. Liddle, *An introduction to modern cosmology; 3rd ed.* Wiley, Chichester, Mar, 2015. https://cds.cern.ch/record/1976476.

[44] **Planck** Collaboration, "Planck 2018 results. VI. Cosmological parameters," *Astron. Astrophys.* **641** (2020) A6, `arXiv:1807.06209 [astro-ph.CO]`.

[45] H. Georgi and S. L. Glashow, "Unity of all elementary-particle forces," *Phys. Rev. Lett.* **32** (Feb, 1974) 438–441. https://link.aps.org/doi/10.1103/PhysRevLett.32.438.

[46] I. Aitchison, *Supersymmetry in Particle Physics. An Elementary Introduction*. Cambridge University Press, Cambridge, 2007.

[47] **Muon g-2** Collaboration, G. Bennett *et al.*, "Final Report of the Muon E821 Anomalous Magnetic Moment Measurement at BNL," *Phys. Rev. D* **73** (2006) 072003, `arXiv:hep-ex/0602035`.

[48] H. Baer and X. Tata, *Weak Scale Supersymmetry: From Superfields to Scattering Events*. Cambridge University Press, 2006.

[49] A. Czarnecki and W. J. Marciano, "The Muon anomalous magnetic moment: A Harbinger for 'new physics'," *Phys. Rev. D* **64** (2001) 013014, `arXiv:hep-ph/0102122`.

[50] J. L. Feng and K. T. Matchev, "Supersymmetry and the anomalous magnetic moment of the muon," *Phys. Rev. Lett.* **86** (2001) 3480–3483, `arXiv:hep-ph/0102146`.

[51] S. Coleman and J. Mandula, "All possible symmetries of the s matrix," *Phys. Rev.* **159** (Jul, 1967) 1251–1256. https://link.aps.org/doi/10.1103/PhysRev.159.1251.

[52] R. Haag, J. T. Lopuszanski, and M. Sohnius, "All Possible Generators of Supersymmetries of the s Matrix," *Nucl. Phys.* **B88** (1975) 257. [,257(1974)].

[53] M. Bustamante, L. Cieri, and J. Ellis, "Beyond the Standard Model for Montaneros," in *5th CERN - Latin American School of High-Energy Physics*. 11, 2009. `arXiv:0911.4409 [hep-ph]`.

[54] J. Wess and B. Zumino, "Supergauge transformations in four dimensions," *Nuclear Physics B* **70** no. 1, (1974) 39 – 50. http://www.sciencedirect.com/science/article/pii/0550321374903551.

[55] H. Georgi and S. L. Glashow, "Gauge theories without anomalies," *Phys. Rev. D* **6** (Jul, 1972) 429–431. https://link.aps.org/doi/10.1103/PhysRevD.6.429.

[56] S. Dimopoulos and D. W. Sutter, "The Supersymmetric flavor problem," *Nucl. Phys. B* **452** (1995) 496–512, `arXiv:hep-ph/9504415`.

[57] **MEG** Collaboration, T. Mori, "Final Results of the MEG Experiment," *Nuovo Cim. C* **39** no. 4, (2017) 325, `arXiv:1606.08168 [hep-ex]`.

[58] H. P. Nilles, "Supersymmetry, Supergravity and Particle Physics," *Phys. Rept.* **110** (1984) 1–162.

[59] A. Lahanas and D. Nanopoulos, "The road to no-scale supergravity," *Physics Reports* **145** no. 1, (1987) 1 – 139. http://www.sciencedirect.com/science/article/pii/0370157387900342.

[60] J. L. Feng, A. Rajaraman, and F. Takayama, "Superweakly interacting massive particles," *Phys. Rev. Lett.* **91** (2003) 011302, `arXiv:hep-ph/0302215`.

[61] **Super-Kamiokande** Collaboration, K. Abe *et al.*, "Search for proton decay via $p \to e^+\pi^0$ and $p \to \mu^+\pi^0$ in 0.31 megaton-years exposure of the Super-Kamiokande water Cherenkov detector," *Phys. Rev.* **D95** no. 1, (2017) 012004, `arXiv:1610.03597 [hep-ex]`.

[62] J. R. Ellis, "Beyond the standard model for hill walkers," in *1998 European School of High-Energy Physics*, pp. 133–196. 8, 1998. `arXiv:hep-ph/9812235`.

[63] J. R. Ellis, J. Hagelin, D. V. Nanopoulos, K. A. Olive, and M. Srednicki, "Supersymmetric Relics from the Big Bang," *Nucl. Phys. B* **238** (1984) 453–476.

[64] A. Djouadi, J.-L. Kneur, and G. Moultaka, "SuSpect: A Fortran code for the supersymmetric and Higgs particle spectrum in the MSSM," *Comput. Phys. Commun.* **176** (2007) 426–455, arXiv:hep-ph/0211331.

[65] C. F. Berger, J. S. Gainer, J. L. Hewett, and T. G. Rizzo, "Supersymmetry without prejudice," *Journal of High Energy Physics* **2009** no. 02, (Feb, 2009) 023–023. http://dx.doi.org/10.1088/1126-6708/2009/02/023.

[66] J. Alwall, P. Schuster, and N. Toro, "Simplified Models for a First Characterization of New Physics at the LHC," *Phys. Rev.* **D79** (2009) 075020, arXiv:0810.3921 [hep-ph].

[67] **LHC New Physics Working Group** Collaboration, D. Alves, "Simplified Models for LHC New Physics Searches," *J. Phys.* **G39** (2012) 105005, arXiv:1105.2838 [hep-ph].

[68] D. S. Alves, E. Izaguirre, and J. G. Wacker, "Where the Sidewalk Ends: Jets and Missing Energy Search Strategies for the 7 TeV LHC," *JHEP* **10** (2011) 012, arXiv:1102.5338 [hep-ph].

[69] F. Ambrogi, S. Kraml, S. Kulkarni, U. Laa, A. Lessa, and W. Waltenberger, "On the coverage of the pMSSM by simplified model results," *Eur. Phys. J. C* **78** no. 3, (2018) 215, arXiv:1707.09036 [hep-ph].

[70] O. Buchmueller and J. Marrouche, "Universal mass limits on gluino and third-generation squarks in the context of Natural-like SUSY spectra," *Int. J. Mod. Phys. A* **29** no. 06, (2014) 1450032, arXiv:1304.2185 [hep-ph].

[71] **ATLAS** Collaboration, M. Aaboud *et al.*, "Dark matter interpretations of ATLAS searches for the electroweak production of supersymmetric particles in $\sqrt{s} = 8$ TeV proton-proton collisions," *JHEP* **09** (2016) 175, arXiv:1608.00872 [hep-ex].

[72] **ATLAS** Collaboration, "Summary of the ATLAS experiment's sensitivity to supersymmetry after LHC Run 1 — interpreted in the phenomenological MSSM," *JHEP* **10** (2015) 134, arXiv:1508.06608 [hep-ex].

[73] **ATLAS** Collaboration, "Mass reach of the atlas searches for supersymmetry." https://atlas.web.cern.ch/Atlas/GROUPS/PHYSICS/PUBNOTES/ATL-PHYS-PUB-2020-020/fig_23.png, 2020.

[74] **CMS** Collaboration, "Summary plot moriond 2017." https://twiki.cern.ch/twiki/pub/CMSPublic/SUSYSummary2017/Moriond2017_BarPlot.pdf, 2017.

[75] L. S. W. Group, "Notes lepsusywg/02-04.1 and lepsusywg/01-03.1." http://lepsusy.web.cern.ch/lepsusy/, 2004. Accessed: 2021-02-11.

[76] **ATLAS** Collaboration, G. Aad *et al.*, "Observation of a new particle in the search for the Standard Model Higgs boson with the ATLAS detector at the LHC," *Phys. Lett. B* **716** (2012) 1–29, arXiv:1207.7214 [hep-ex].

[77] **CMS** Collaboration, S. Chatrchyan *et al.*, "Observation of a New Boson at a Mass of 125 GeV with the CMS Experiment at the LHC," *Phys. Lett. B* **716** (2012) 30–61, arXiv:1207.7235 [hep-ex].

[78] CERN, "About cern." https://home.cern/about. Accessed: 2021-01-21.

[79] L. R. Evans and P. Bryant, "LHC Machine," *JINST* **3** (2008) S08001. 164 p. http://cds.cern.ch/record/1129806. This report is an abridged version of the LHC Design Report (CERN-2004-003).

[80] R. Scrivens, M. Kronberger, D. Küchler, J. Lettry, C. Mastrostefano, O. Midttun, M. O'Neil, H. Pereira, and C. Schmitzer, "Overview of the status and developments on primary ion sources at CERN*,". https://cds.cern.ch/record/1382102.

[81] E. Mobs, "The CERN accelerator complex - 2019. Complexe des accélérateurs du CERN - 2019,". https://cds.cern.ch/record/2684277. General Photo.

[82] **ATLAS** Collaboration, "The ATLAS Experiment at the CERN Large Hadron Collider," *JINST* **3** (2008) S08003.

[83] **CMS** Collaboration, S. Chatrchyan *et al.*, "The CMS Experiment at the CERN LHC," *JINST* **3** (2008) S08004.

[84] **ALICE** Collaboration, K. Aamodt *et al.*, "The ALICE experiment at the CERN LHC," *JINST* **3** (2008) S08002.

[85] **LHCb** Collaboration, J. Alves, A.Augusto *et al.*, "The LHCb Detector at the LHC," *JINST* **3** (2008) S08005.

[86] **TOTEM** Collaboration, G. Anelli *et al.*, "The TOTEM experiment at the CERN Large Hadron Collider," *JINST* **3** (2008) S08007.

[87] **LHCf** Collaboration, O. Adriani *et al.*, "Technical design report of the LHCf experiment: Measurement of photons and neutral pions in the very forward region of LHC,".

[88] **MoEDAL** Collaboration, J. Pinfold *et al.*, "Technical Design Report of the MoEDAL Experiment,".

[89] O. S. Bruning, P. Collier, P. Lebrun, S. Myers, R. Ostojic, J. Poole, and P. Proudlock, *LHC Design Report*. CERN Yellow Reports: Monographs. CERN, Geneva, 2004. https://cds.cern.ch/record/782076.

[90] **ATLAS** Collaboration, "ATLAS Public Results - Luminosity Public Results Run 2,". https://twiki.cern.ch/twiki/bin/view/AtlasPublic/LuminosityPublicResultsRun2. Accessed: 2021-01-17.

[91] **ATLAS** Collaboration, Z. Marshall, "Simulation of Pile-up in the ATLAS Experiment," *J. Phys. Conf. Ser.* **513** (2014) 022024.

[92] "First beam in the LHC - accelerating science,". https://home.cern/news/news/accelerators/record-luminosity-well-done-lhc. Accessed: 2021-01-10.

[93] **ATLAS Collaboration** Collaboration, "Luminosity determination in pp collisions at $\sqrt{s} = 13$ TeV using the ATLAS detector at the LHC," Tech. Rep. ATLAS-CONF-2019-021, CERN, Geneva, Jun, 2019. https://cds.cern.ch/record/2677054.

[94] **ATLAS** Collaboration, M. Aaboud *et al.*, "Luminosity determination in pp collisions at $\sqrt{s} = 8$ TeV using the ATLAS detector at the LHC," *Eur. Phys. J. C* **76** no. 12, (2016) 653, `arXiv:1608.03953 [hep-ex]`.

[95] G. Avoni, M. Bruschi, G. Cabras, D. Caforio, N. Dehghanian, A. Floderus, B. Giacobbe, F. Giannuzzi, F. Giorgi, P. Grafström, V. Hedberg, F. L. Manghi, S. Meneghini, J. Pinfold, E. Richards, C. Sbarra, N. S. Cesari, A. Sbrizzi, R. Soluk, G. Ucchielli, S. Valentinetti, O. Viazlo, M. Villa, C. Vittori, R. Vuillermet, and A. Zoccoli, "The new

LUCID-2 detector for luminosity measurement and monitoring in ATLAS," *Journal of Instrumentation* **13** no. 07, (Jul, 2018) P07017–P07017. https://doi.org/10.1088/1748-0221/13/07/p07017.

[96] S. van der Meer, "Calibration of the effective beam height in the ISR," Tech. Rep. CERN-ISR-PO-68-31. ISR-PO-68-31, CERN, Geneva, 1968. https://cds.cern.ch/record/296752.

[97] P. Grafström and W. Kozanecki, "Luminosity determination at proton colliders," *Progress in Particle and Nuclear Physics* **81** (2015) 97 – 148. http://www.sciencedirect.com/science/article/pii/S0146641014000878.

[98] "New schedule for CERN's accelerators and experiments,". https://home.cern/news/press-release/cern/first-beam-lhc-accelerating-science. Accessed: 2021-01-10.

[99] **ATLAS** Collaboration, G. Aad *et al.*, "Luminosity Determination in *pp* Collisions at $\sqrt{s} = 7$ TeV Using the ATLAS Detector at the LHC," *Eur. Phys. J. C* **71** (2011) 1630, `arXiv:1101.2185 [hep-ex]`.

[100] **ATLAS Collaboration** Collaboration, G. Aad *et al.*, "Improved luminosity determination in pp collisions at $\sqrt{s} = 7$ TeV using the ATLAS detector at the LHC. Improved luminosity determination in pp collisions at sqrt(s) = 7 TeV using the ATLAS detector at the LHC," *Eur. Phys. J. C* **73** no. CERN-PH-EP-2013-026. CERN-PH-EP-2013-026, (Feb, 2013) 2518. 27 p. https://cds.cern.ch/record/1517411. Comments: 26 pages plus author list (39 pages total), 17 figures, 9 tables, submitted to EPJC, All figures are available at <a href=.

[101] "Record luminosity: well done LHC,". https://home.cern/news/news/accelerators/new-schedule-cerns-accelerators-and-experiments. Accessed: 2021-01-10.

[102] A. G., B. A. I., B. O., F. P., L. M., R. L., and T. L., *High-Luminosity Large Hadron Collider (HL-LHC): Technical Design Report V. 0.1*. CERN Yellow Reports: Monographs. CERN, Geneva, 2017. https://cds.cern.ch/record/2284929.

[103] J. Pequenao, "Computer generated image of the whole ATLAS detector." Mar, 2008.

[104] **ATLAS** Collaboration, "ATLAS: Detector and physics performance technical design report. Volume 1,".

[105] J. Pequenao, "Computer generated image of the ATLAS inner detector." Mar, 2008.

[106] **ATLAS Collaboration** Collaboration, K. Potamianos, "The upgraded Pixel detector and the commissioning of the Inner Detector tracking of the ATLAS experiment for Run-2 at the Large Hadron Collider," Tech. Rep. ATL-PHYS-PROC-2016-104, CERN, Geneva, Aug, 2016. https://cds.cern.ch/record/2209070. 15 pages, EPS-HEP 2015 Proceedings.

[107] **ATLAS IBL** Collaboration, B. Abbott *et al.*, "Production and Integration of the ATLAS Insertable B-Layer," *JINST* **13** no. 05, (2018) T05008, `arXiv:1803.00844 [physics.ins-det]`.

[108] **ATLAS** Collaboration, "ATLAS Insertable B-Layer Technical Design Report," Tech. Rep. CERN-LHCC-2010-013. ATLAS-TDR-19, Sep, 2010. http://cds.cern.ch/record/1291633.

[109] **ATLAS** Collaboration, G. Aad *et al.*, "ATLAS b-jet identification performance and efficiency measurement with $t\bar{t}$ events in pp collisions at $\sqrt{s} = 13$ TeV," *Eur. Phys. J. C* **79** no. 11, (2019) 970, `arXiv:1907.05120 [hep-ex]`.

[110] J. Pequenao, "Computer Generated image of the ATLAS calorimeter." Mar, 2008.

[111] J. Pequenao, "Computer generated image of the ATLAS Muons subsystem." Mar, 2008.

[112] S. Lee, M. Livan, and R. Wigmans, "Dual-Readout Calorimetry," *Rev. Mod. Phys.* **90** no. arXiv:1712.05494. 2, (Dec, 2017) 025002. 40 p. https://cds.cern.ch/record/2637852. 44 pages, 53 figures, accepted for publication in Review of Modern Physics.

[113] M. Leite, "Performance of the ATLAS Zero Degree Calorimeter," Tech. Rep. ATL-FWD-PROC-2013-001, CERN, Geneva, Nov, 2013. https://cds.cern.ch/record/1628749.

[114] S. Abdel Khalek *et al.*, "The ALFA Roman Pot Detectors of ATLAS," *JINST* **11** no. 11, (2016) P11013, `arXiv:1609.00249 [physics.ins-det]`.

[115] U. Amaldi, G. Cocconi, A. Diddens, R. Dobinson, J. Dorenbosch, W. Duinker, D. Gustavson, J. Meyer, K. Potter, A. Wetherell, A. Baroncelli, and C. Bosio, "The real part of the forward proton proton scattering amplitude measured at the cern intersecting storage rings," *Physics Letters B* **66** no. 4, (1977) 390 – 394. http://www.sciencedirect.com/science/article/pii/0370269377900223.

[116] L. Adamczyk, E. Banaś, A. Brandt, M. Bruschi, S. Grinstein, J. Lange, M. Rijssenbeek, P. Sicho, R. Staszewski, T. Sykora, M. Trzebiński, J. Chwastowski, and K. Korcyl, "Technical Design Report for the ATLAS Forward Proton Detector," Tech. Rep. CERN-LHCC-2015-009. ATLAS-TDR-024, May, 2015. https://cds.cern.ch/record/2017378.

[117] **ATLAS** Collaboration, A. R. Martínez, "The Run-2 ATLAS Trigger System," *J. Phys. Conf. Ser.* **762** no. 1, (2016) 012003.

[118] **ATLAS Collaboration** Collaboration, *ATLAS level-1 trigger: Technical Design Report*. Technical Design Report ATLAS. CERN, Geneva, 1998. https://cds.cern.ch/record/381429.

[119] **ATLAS Collaboration** Collaboration, P. Jenni, M. Nessi, M. Nordberg, and K. Smith, *ATLAS high-level trigger, data-acquisition and controls: Technical Design Report*. Technical Design Report ATLAS. CERN, Geneva, 2003. https://cds.cern.ch/record/616089.

[120] **ATLAS** Collaboration, G. Aad *et al.*, "Performance of the missing transverse momentum triggers for the ATLAS detector during Run-2 data taking," *JHEP* **08** (2020) 080, `arXiv:2005.09554 [hep-ex]`.

[121] **ATLAS** Collaboration, G. Aad *et al.*, "Performance of algorithms that reconstruct missing transverse momentum in $\sqrt{s} = 8$ TeV proton-proton collisions in the ATLAS detector," *Eur. Phys. J. C* **77** no. 4, (2017) 241, `arXiv:1609.09324 [hep-ex]`.

[122] **ATLAS** Collaboration, G. Aad *et al.*, "Topological cell clustering in the ATLAS calorimeters and its performance in LHC Run 1," *Eur. Phys. J. C* **77** (2017) 490, `arXiv:1603.02934 [hep-ex]`.

[123] **ATLAS** Collaboration, G. Aad *et al.*, "The ATLAS Simulation Infrastructure," *Eur. Phys. J. C* **70** (2010) 823–874, arXiv:1005.4568 [physics.ins-det].

[124] T. Gleisberg, S. Hoeche, F. Krauss, M. Schonherr, S. Schumann, F. Siegert, and J. Winter, "Event generation with SHERPA 1.1," *JHEP* **02** (2009) 007, arXiv:0811.4622 [hep-ph].

[125] A. Buckley *et al.*, "General-purpose event generators for LHC physics," *Phys. Rept.* **504** (2011) 145–233, arXiv:1101.2599 [hep-ph].

[126] V. N. Gribov and L. N. Lipatov, "Deep inelastic e p scattering in perturbation theory," *Sov. J. Nucl. Phys.* **15** (1972) 438–450.

[127] J. Blumlein, T. Doyle, F. Hautmann, M. Klein, and A. Vogt, "Structure functions in deep inelastic scattering at HERA," in *Workshop on Future Physics at HERA (To be followed by meetings 7-9 Feb and 30-31 May 1996 at DESY)*. 9, 1996. arXiv:hep-ph/9609425.

[128] A. Buckley, J. Ferrando, S. Lloyd, K. Nordström, B. Page, M. Rüfenacht, M. Schönherr, and G. Watt, "LHAPDF6: parton density access in the LHC precision era," *Eur. Phys. J. C* **75** (2015) 132, arXiv:1412.7420 [hep-ph].

[129] M. Bengtsson and T. Sjostrand, "Coherent Parton Showers Versus Matrix Elements: Implications of PETRA - PEP Data," *Phys. Lett. B* **185** (1987) 435.

[130] S. Catani, F. Krauss, R. Kuhn, and B. R. Webber, "QCD matrix elements + parton showers," *JHEP* **11** (2001) 063, arXiv:hep-ph/0109231.

[131] L. Lonnblad, "Correcting the color dipole cascade model with fixed order matrix elements," *JHEP* **05** (2002) 046, arXiv:hep-ph/0112284.

[132] B. Andersson, G. Gustafson, G. Ingelman, and T. Sjostrand, "Parton Fragmentation and String Dynamics," *Phys. Rept.* **97** (1983) 31–145.

[133] B. Andersson, *The Lund Model*. Cambridge Monographs on Particle Physics, Nuclear Physics and Cosmology. Cambridge University Press, 1998.

[134] D. Amati and G. Veneziano, "Preconfinement as a Property of Perturbative QCD," *Phys. Lett. B* **83** (1979) 87–92.

[135] M. Dobbs and J. B. Hansen, "The HepMC C++ Monte Carlo event record for High Energy Physics," *Comput. Phys. Commun.* **134** (2001) 41–46.

[136] **GEANT4** Collaboration, S. Agostinelli *et al.*, "GEANT4: A Simulation toolkit," *Nucl. Instrum. Meth.* **A506** (2003) 250–303.

[137] **ATLAS Collaboration** Collaboration, "The new Fast Calorimeter Simulation in ATLAS," Tech. Rep. ATL-SOFT-PUB-2018-002, CERN, Geneva, Jul, 2018. https://cds.cern.ch/record/2630434.

[138] K. Cranmer, "Practical Statistics for the LHC," in *2011 European School of High-Energy Physics*, pp. 267–308. 2014. arXiv:1503.07622 [physics.data-an].

[139] G. Cowan, K. Cranmer, E. Gross, and O. Vitells, "Asymptotic formulae for likelihood-based tests of new physics," *Eur. Phys. J.* **C71** (2011) 1554, arXiv:1007.1727 [physics.data-an]. [Erratum: Eur. Phys. J.C73,2501(2013)].

[140] ATLAS Collaboration, "Reproduction searches for new physics with the ATLAS experiment through publication of full statistical likelihoods." ATL-PHYS-PUB-2019-029, 2019. https://cds.cern.ch/record/2684863.

[141] **ROOT Collaboration** Collaboration, K. Cranmer, G. Lewis, L. Moneta, A. Shibata, and W. Verkerke, "HistFactory: A tool for creating statistical models for use with RooFit and RooStats," Tech. Rep. CERN-OPEN-2012-016, New York U., New York, Jan, 2012. https://cds.cern.ch/record/1456844.

[142] A. Wald, "Tests of statistical hypotheses concerning several parameters when the number of observations is large," *Transactions of the American Mathematical Society* **54** no. 3, (1943) 426–482. https://doi.org/10.1090/S0002-9947-1943-0012401-3.

[143] S. S. Wilks, "The large-sample distribution of the likelihood ratio for testing composite hypotheses," *Ann. Math. Statist.* **9** no. 1, (03, 1938) 60–62. https://doi.org/10.1214/aoms/1177732360.

[144] G. Cowan, "Statistics for Searches at the LHC," in *69th Scottish Universities Summer School in Physics: LHC Physics*, pp. 321–355. 7, 2013. `arXiv:1307.2487 [hep-ex]`.

[145] A. L. Read, "Presentation of search results: the CL_S technique," *J. Phys. G* **28** (2002) 2693.

Acknowledgements

An dieser Stelle möchte ich mich herzlich bei allen bedanken, die mich bei der Anfertigung dieser Arbeit unterstützt haben. Insbesondere danke ich herzlich

- Prof. Dr. Dorothee Schaile für die Möglichkeit, diese Arbeit an ihrem Lehrstuhl durchzuführen sowie das Korrekturlesen der Arbeit.
- Dr. Jeanette Lorenz für die ausgezeichnete Betreuung, die vielen Anregungen, sowie die ehrliche und konstruktive Kritik beim Korrekturlesen dieser Arbeit. Sie hat es mir ermöglicht aktiv im 1-Lepton Analyseteam an der Suche nach Supersymmetrie mitwirken zu können.
- Dr. Nikolai Hartmann für die unzähligen Diskussionen über den Sinn und Unsinn der Datenanalyse mit und ohne ATLAS Software. Vielen Dank für die stets geduldige und ausführliche Beantwortung meiner Fragen, sowie das Bereitstellen unzähliger Zeilen Code, ohne die vieles schwieriger gewesen wäre.
- Allen Mitgliedern des Lehrstuhls Schaile für die angenehme und freundliche Arbeitsatmosphäre.
- Allen Freunden, die stets da waren, wenn ich sie gebraucht habe.

I also want to thank the entire 1-lepton analysis team, especially the coordinators Jeanette Lorenz, Da Xu and Alberto Cervelli. Thank you for the always supportive and enjoyable work environment. Many thanks also to Valentina Tudorache for patiently answering all my questions as well as all the entertaining conversations.

I would further like to thank Dr. Brian Petersen without whom the presented pMSSM studies would not have been possible.

En léiwen Merci och dem Yannick Erpelding fir d'Korrekturliesen—och wann en net alles verstanen huet—an dem Nick Beffort, fir all déi domm Reddit Posts, d'Korrekturliesen, an dei onzähleg Stonnen zesummen mat enger Spezi an der Hand.

Zu gudder Läscht, wëll ech op dëser Platz menger ganzer Famill merci soen, virun allem mengen léiwen Elteren an menger wonnerbarer Schwëster. Merci dass dir mëch bei allem waat ech maachen ënnerstëtzt an dass ech ëmmer op iech zielen kann, och wann ech weit fort sin. Ouni iech wier daat heiten net méiglech gewiescht. Besonneschen Merci och dem Nathalie Münster, dofir dass et mech seit Joren ëmmer ënnerstëtzt an ëmmer fir mech do as, och wann ech heiansdo depriméiert oder duercherneen sin.

Selbstständigkeitserklärung

Hiermit erkläre ich, die vorliegende Arbeit mit dem Titel

WIP: Work in Progress Title

WIP: Work in Progress Title

selbständig verfasst zu haben und keine anderen als die in der Arbeit angegebenen Quellen und Hilfsmittel benutzt zu haben.

Eric Schanet

München, den 01. Mai 2021